Faculdade de Engenharia da Universidade do Porto

Numerical study on Structural response of dental restorations using finite element method and meshless methods

Farid Mehri Sofiani

Dissertation submitted to the Faculty of Engineering of the University of Porto as a requirement to obtain the MSc degree in Computational Mechanics

Supervisor: Professor Jorge Americo Oliveira Pinto Belinha

Co-supervisor: Professor Renato Natal Manuel Natal Jorge

December 2018

Abstract

Dental carries and dental restorations have a long history and over the years, many materials and methods were invented. In recent decades, modern techniques and materials have brought complexity to this issue, which have created the necessity to investigate more and more to achieve high quality, consistency, good mechanical properties, efficiency, beauty, good color, and reduce the costs and time. Combined with the recent advances in the medical field, mechanical engineering plays one of the most important roles in this topic.

Therefore, the main goal of this master thesis is to analyze some commercial materials in trend. Additionally, it aims to compare the results of distinct discrete numerical methods – the finite element method (FEM) and meshless methods. The pros and cons of the analyzed materials are identified, which could be used by the producers of the studied materials to improve their quality. On the other hand, a computational framework, as the one here presented, would assist the clinical practice and treatment decision (in accordance with each patient's characteristics).

Based on the 2D model domain that is drawn for this work, and the zone that is considered to be replaced by commercial dental restorative materials, structural responses are observed. The 2D model was meshed for the FEM study and from it, the nodal mesh was retrieved to be analyzed using meshless methods, including the Radial Point Interpolation Method (RPIM) and Natural Neighbor Radial Point Interpolation Method (NNRPIM). Meshless methods are advanced discretization method capable to give accurate and smooth variable fields. A total of four load cases are imposed as natural boundary conditions to this model. In contrary to many previous works (which address fatigue mechanics), this work's analysis is elasto-static and also elasto-plastic and the materials' behavior in each zone are discussed and compared. Therefore, this works uses linear solution algorithm and also Newton-Raphson non-linear algorithm to achieve the solution. The results show that both formulations (FEM and meshless methods) are capable to produce similar results. Showing that meshless methods are an efficient and robust numerical technique for biomechanics.

Keywords: Radial Point Interpolation Method, Natural Neighbor Interpolation Method, Finite Element Method, Dental Restorations, Dental Restorative Composites, Linear elastic analysis, non-linear elasto-plastic analysis

Acknowledgments

I would like to say many thanks to Professor Jorge Belinha, who encouraged, supported and taught me many lessons in this path. His continuous guidance and help enabled me to finish this work successfully. I am grateful for his patience, motivation and immense knowledge.

Also, I would like to express my sincere gratitude to Professor Renato Natal Jorge, the director of the master's degree program in computational mechanics at the University of Porto, Engineering faculty. I appreciate his support from first day until now and his consideration of my hard situation. This precious help made it possible to conduct this master studies for me.

I have to express my appreciation to my parents and my dear brother for their sacrifices both moral and economical throughout my M.Sc. Course in the most terrible days of my country that we don't have neither the support of our government nor the foreign countries and our people have to resist. However, I was beloved and been supported by my dear family that I will never forget it. I hope I deserve this kindness and love.

Institutional Acknowledgments and Funding

The author truly acknowledges the work conditions provided by the Applied Mechanics Division (SMAp) of the Department of Mechanical Engineering (DEMec) of the Faculty of Engineering of the University of Porto (FEUP), and by the MIT-Portugal project "MIT-EXPL/ISF/0084/2017", funded by Massachusetts Institute of Technology (USA) and "Ministério da Ciência, Tecnologia e Ensino Superior - Fundação para a Ciência e a Tecnologia" (Portugal).

Additionally, the authors gratefully acknowledge the funding of Project NORTE-01-0145-FEDER-000022 - SciTech - Science and Technology for Competitive and Sustainable Industries, cofinanced by Programa Operacional Regional do Norte (NORTE2020), through Fundo Europeu de Desenvolvimento Regional (FEDER).

Finally, the author acknowledges the synergetic collaboration with the Researchers of "Computational Mechanics Research Laboratory CMech-Lab" (ISEP/FEUP/INEGI), and its director, Prof. Dr. Jorge Belinha, and its senior advisors, Prof. Dr. Renato Natal Jorge and Prof. Dra. Lúcia Dinis.

To my lovely parents and my dear brother, Vahid

Contents

List of Figures

List of tables

Chapter 1

Introduction

Dental restoration is a concept that can be found since 1400 years ago in China, mainly motivated by the dental carries [1]. For the modern human, due to changes in lifestyle and diet, dental carries became more prevalent than old days, which motivated scientists to find and develop new materials and techniques to solve this problem properly. One of the threats to a normal tooth is fracture due to several situations, such was self-contact between teeth or by abrupt impact with an external object. One of the most important cases that cause damage and fracture in a human tooth is Bruxism. By the time passes, many restorative materials are being produced to restore the fractured teeth, revealing the importance to study on these materials to avoid the usage of low-quality materials and improve them in both medical and mechanical perspective.

1.1. Motivation and pathology

The main goal in the current work is to investigate some commercial materials behaviour under certain load cases (Bruxism) in a condition that one side of the molar tooth is free and, in the opposite side, there is a tooth, just next to the molar tooth being analyzed. Being bruxism is a common phenomenon. it was chosen for this study.

The elasto-static and elasto-plastic analysis are performed for selected loading cases, and all the results are compared between each other (materials versus materials, FEM versus meshless). Nevertheless, as a computational mechanics motivation, a strong emphasis is given to the comparison between the FEM and both meshless methods - the Radial Point Interpolation Method (RPIM)and Natural Neighbor Radial Interpolation Method (NNRPIM).

Since this work is a biomedical research, it starts with an explanation on how it behaves the biological system under study. The cortical and trabecular bone surrounds a normal molar tooth in the root, and the tooth itself is constituted with different parts, such as enamel, dentine, pulp, and periodontal

ligament. In the mechanical model in this work, a part of a tooth is replaced by commercial dental restorative composites. It is consequential to observe what happens to the material under the certain loading situation and measure how the material tolerates the stress.

1.2. Document Structure

The thesis is organized in several chapters, starting with chapter 1 as an introduction to the subject and the theme of the work. In chapter 2, all the necessary and related description about dental restorations, main threats to teeth such as bruxism, and then materials, and techniques to restore a tooth, has been given. Chapter 3 concentrates on the biological system of bone and tooth and the mechanical properties of the mentioned systems. Chapter 4, focuses on Solid Mechanics and the related formulations for elasto-static and elasto-plastic analysis. In chapter 5, the finite element method and meshless methods used in this work are explained and the general procedure, nodal connectivity, integration method, and the shape functions are discussed. In chapter 6, the mechanical model is described and analysed and the results are revealed and discussed. Finally, chapter 7 concludes the work and presents the ideas and suggestion for the future works.

Chapter 2

Dental Restorations

Dental caries has been always considered one of the most important issues in the global oral disease burden. Dental caries, not only in 3rd world countries but even in most high-income countries, are still a major public health problem [2].

2.1. Main threats to Oral Health

Oral health is one the most important and essential part of human life. Healthy teeth would increase the quality of life and helps to improve the senses and to chew. Nevertheless, a human with healthy teeth can express his feelings and emotions better with facial expressions. However, oral diseases, which range widely, cause pain and disorders for many people each year [3]. In the next section, the main threats to oral health are discussed, and also a brief explanation is done about the people that are exposed to these threats.

2.1.1 Dental erosion, tooth decay (cavities), and periodontal (gum) disease

Dental erosion is used as a physical term to describe the mentioned results [4]: When the dental hard tissue is chemically etched away from the tooth surface without bacterial involvement as a result of being acid or chelation on the tooth. The second main threat is *tooth decay* (cavities), which is a common and preventable problem of all people in the world [3]. It is known formally as dental caries, and it has always been a serious health problem for all nations, in which a certain oral bacteria discharge mineraleroding acid onto the enamel, starting the gradual process of decay. The bacteria related to the tooth decay lives in communities so-called biofilms [5]. The third main threat is *periodontal (gum) disease*, that is a complicated infection of bacterial origin in which multiple factors are implicated [6]. This chronic bacterial infection is characterized by persistent inflammation, connective tissue breakdown, and alveolar bone destruction [7]. Severe periodontitis, which may lead to tooth loss, is observed around 5-20% of most populations all around the world [8]. Adults and children would have

different forms of periodontitis, such as aggressive periodontitis, chronic periodontitis, and periodontitis as a manifestation of systematic disease [7],[9].

2.1.2 Risk factors for oral disease

Generally, almost all forms of periodontal disease, tooth decay, and dental erosion occur as a result of poor oral hygiene practices, improper nutrition and diet, dry mouth issues, genetics, and age. Periodontal disease's extent and severity depend on the interaction between the bacteria and the host response. So, the presence of the bacteria is a necessary but insufficient condition for the onset of the disease and in fact, **genetic** factors which affect the immune system and also the environmental factors come with a microbiological agent to trigger the disease (Fig. 2-1) [6]. It is necessary to take the inherent tendency of the tooth into account (which is so-called **dental degenerative changes)** during aging, such as attrition, periodontosis, secondary dentin, cementum apposition, root resorption, and transparency of the root [10]. Researchers over the years have used different methods and techniques to estimate age based on this property of teeth [11],[12],[13]. Thus, this is a phenomenon which is not independent of genetics, guiding the researchers to consider the risk factors' effects on younger people to be different from those effects on older people.

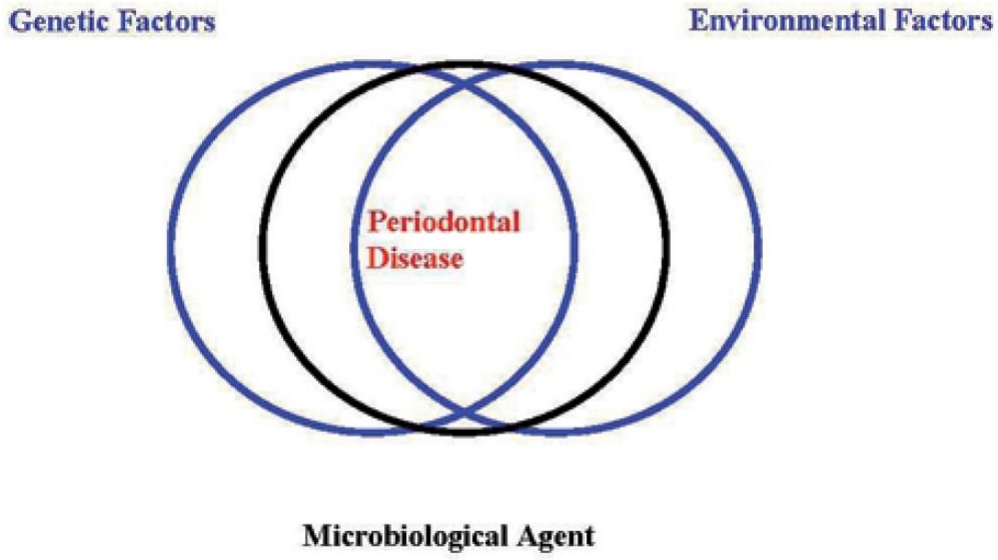

Figure 2. 1- Factors implicated in periodontal disease [6].

To get deeper sight about the risk factors, the most dangerous ones are addressed in this section.

First of all, **poor diet** as an important environmental factor is always focused on several types of research. Poor diet, consisting of sugary foods, acidic drinks (like soft drinks), alcohol, etc. Poor diet is a preventable risk factor that can be controlled. Soft drinks containing inherent acids and sugars have both erosion problems and cariogenic potential [14],[15]. Bowen and Lawrence obtained some data in

2005 which demonstrated that the cariogenicity and erosion of soft drinks and honey are higher than that of milk and sucrose and to reduce dental caries risk, the low-calorie and sugar-free food were recommended [16]. However, sugar-free soft drinks often have as high erosive potential as sugar-containing soft drinks [17]. Almost in all over the world, soft drinks have turned out to be highly dangerous drinks for oral health. Al-Majed et al. in 2002 identified some risk factors for dental erosion among 5-6 years old and 12-14 years old boys in Saudi Arabia, which were all about soft drinks consumption, especially at night [18].

Furthermore, researches indicate that pH of carbonated drinks is lower than fruit juices and the pH for different kind of drinks is in the following order: fruit juices > fruit-based carbonated drinks > non-fruit-based carbonated drinks [19]. The carbonated drink could reduce surface hardness of enamel, dentine, micro filled composite, and resin-modified glass ionomer and even sports drink and juices have influence on enamel [20]. Sports drinks have a more softening effect than fruit juices [21],[22]. Also, some studies revealed that dental erosion is associated with **drinking methods**. Holding the drink longer in the mouth can lead to a more pronounced pH drop [23].

Excessive alcohol consumption is attributed to be also one of the main threats to oral health, a habit that should be modified [24]. Based on the annual report of world health statistics in 2017, Portugal is the 24th country in Europe in alcohol consumption per capita with an average of 10.6 litters, which means that Portuguese people drink alcohol more than 27 other European countries' people [25]. This amount of alcohol consumption is considerable when the comparison is made between Portugal and the rest of the world. Thus, one of the essential key factors for Portugal could be decreasing the harmful use of alcohol. Besides, it's very important to know that the poor diet is not restricted to those mentioned above. There are several kinds of foods and drinks which have consequential effects on teeth and also an important role in making diseases like gastroesophageal reflux. Research in China revealed a prevalence of dental erosion among people with gastroesophageal reflux [26].

Since tobacco smoking is one of the main reasons for death and mortality [27], it's important to be concerned about it. Nevertheless, tobacco smokers, which are estimated to be around one billion people all over the world, are exposed by dental issues. Still, researchers are investigating the harmful effects of tobacco on human's body, and a wide range of studies are about oral health. Not only the natural teeth but also the restored teeth are under investigation. For instance, tobacco smoking would have a considerable effect on color stability and roughness of restored teeth with composite [28]. Tobacco smoking per capita in Portugal shows this country to be ranked 28th among 45 European countries which submitted data [25] and still Portugal is consuming tobacco more than 17 other European countries. Furthermore, in a case-control study in India [29], existing a relationship between oral hygiene, tobacco, and risk of oral cancer was approved. Thus, tobacco smoking should be considered as a consequential habit leading to oral disease.

One of the mechanical risk factors that are not normal and does not occur usually is **dental damage in anaesthesia** [30]. Although it does not happen regularly, it is mandatory to take it into account due to the consequential effects of this phenomenon, which are represented in table 2.1 [31]. The arch of incisors can generate a force range of 150-200 N [32] along the axis, and both healthy maxillary and mandibular teeth can tolerate this amount of force. However, a vulnerable tooth, such as a restored tooth, or the teeth replaced with artificial materials, and the ones with periodontal disease, etc. wouldn't withstand the force and damage may occur. According to the literature, the restored teeth are five times more likely to experience dental trauma [33].

Classification	Number (%)
Subluxation	33 (35%)
Crown fracture	18 (19%)
Missing teeth	11 (12%)
Avulsion	7 (7%)
Crown and root fracture	5 (5%)
Enamel fracture	5 (5%)
Other trauma	15 (16%)

Table 2. 1- Classification of 94 cases of dental trauma [31]

Bruxism is also considered as a mechanical risk factor for dental damage that has its root cause in Central Nervous System [34], which forces the jaw-muscle to move in a repetitively order leading to the grind and clenching of the teeth. Bruxism would become an important issue due to its capability to cause fracture or tooth wear. Bruxism can happen either during the awake period or during the sleep period. This common phenomenon is still under investigation, and there are many unknown reasons for Bruxism. As an instance, recently in 2017, Serra-Negra et al. formulated that chronotype and Bruxism could be related to each other and there may be an association between them [35].

2.2. Protecting oral health and costs

As it is mentioned previously, oral diseases are all preventable, and prevention is now the mantra in dentistry. During the years, several products and techniques were introduced to fight oral disease, and more people benefit from preventive dentistry. Compared to old days, these techniques have made it possible for millions of more people to keep their natural teeth and save money. It is estimated that American people from 1979 to 1989 (10 years) have saved more than 39 billion dollars in dental costs due to the big help of prevention [5].

There are too many reasons for convincing the protection of oral health. However, here in this section, mostly it will be focused on the consequences of tooth loss which makes dental restorations necessary.

Notice that tooth loss has been indicated as an important epidemiological indicator of oral health [36]. Figure 2.2 shows a decision-make tree with a brief expression of the result of tooth extracting and treatment. Oral diseases such as periodontal disease and untreated caries are the two main reasons for tooth loss globally [37],[38]. Generally, tooth extraction directly influences oral function and aesthetics; therefore oral health is related to the quality of life [39].

One of the reasons that make protecting oral health necessary is the generation of some diseases as a consequence of dental health problems, such as tooth loss (which can be one of the factors to increase the risk of future coronary heart disease (CHD) [40]). Nevertheless, the recent research revealed that greater loss of teeth and having less natural teeth, considerably and independently linked with increased risk of CHD [40].

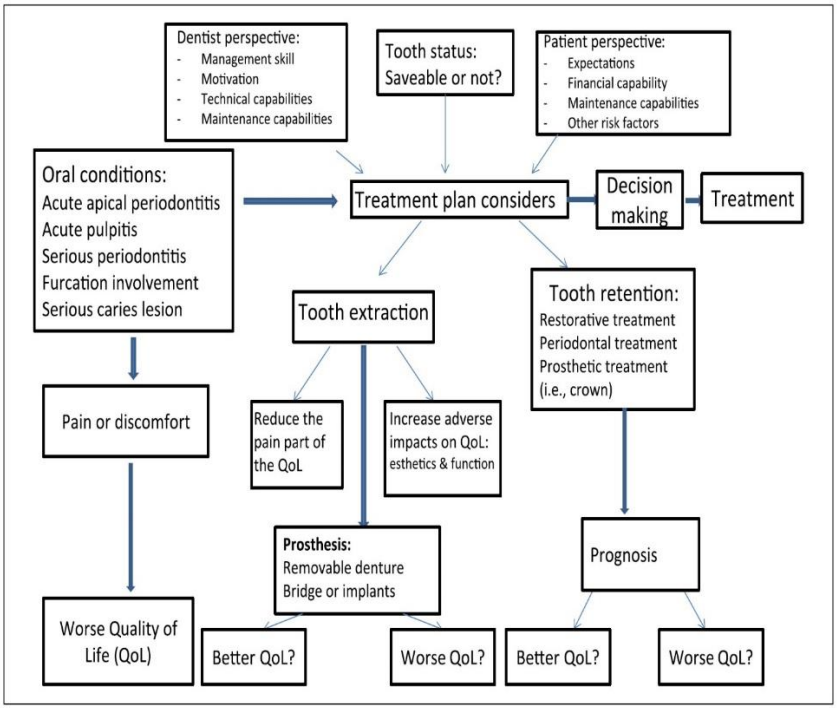

Figure 2. 2- Decision-making tree for tooth extraction and pathways to quality-of-life (QoL) impacts [39]

According to an International Agency for Research on Cancer (IARC) 2012 Report, lip, oral cavity related cancer is the 7th concerning incidence and mortality in Portugal [41], see Figure 2.3.

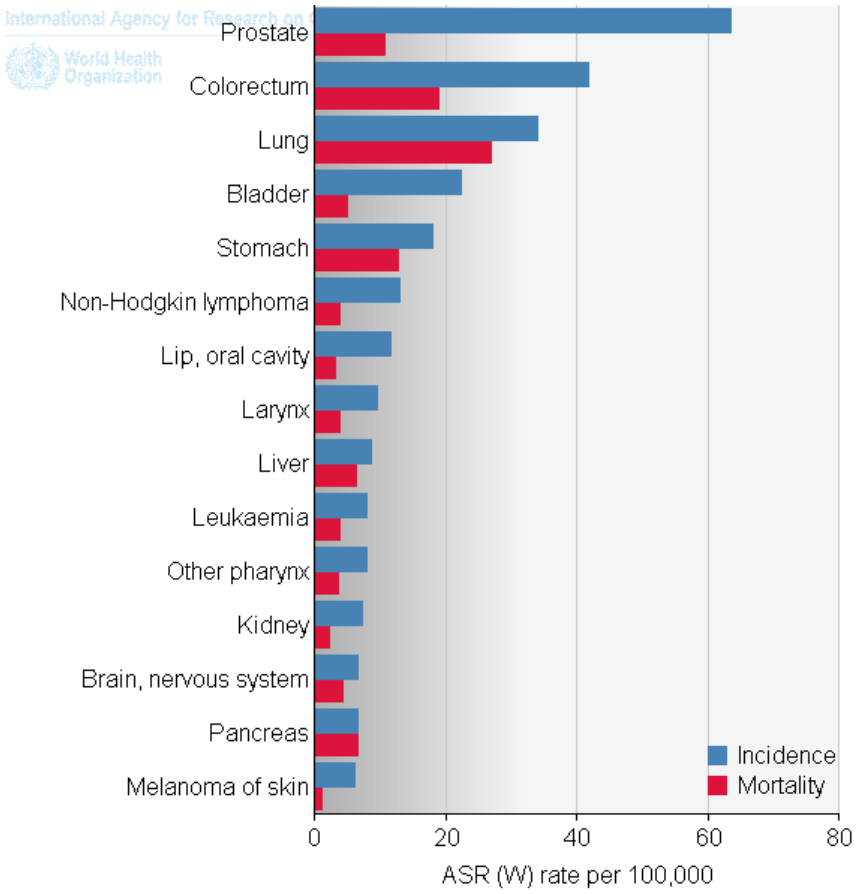

Figure 2. 3- Top cancers in case of incidence and mortality in Portugal, based on ASR scale in 2012 [41]

Oral diseases, especially tooth loss in most of the developed countries, is decreasing due to preventive measures such as periodic visits, including professional tooth cleaning and raising awareness of controlling healthy diet to keep oral health among young people [42],[43]. The fact that 122 billion dollars were spent for dental caries in 2014 only in the U.S.A [42] alerts for the necessity of practicing preventive ways.

2.3. Materials and methods of dental restorations

During the last 40 years, the porcelain-fused-to-metal technique has been used to fix the teeth [44], and this technique has been improved by the usage of biocompatible materials [45]. Dental caries is a common disease and since prehistoric times humans are exposed to it. The burst of this disease has raised because of dietary changes that occurred in human lifestyles. Nevertheless, there is now evidence that this trend has got to its climax and has begun now to decline in certain segments of the population of New Zealand, United States, Western Europe, and Australia. The main cause of the decrease is the addition of fluoride ions to public drinking water. This decline in developed countries has been prominent

in the upper classes and middle classes, while the lower socioeconomic and rural classes have retained a high prevalence of tooth decay.

2.3.1 Classic materials and methods

The first developed efficient material solution-therapy is the amalgam. Amalgam is a metallic restorative material used for direct filling of carious lesions. There are some reports revealing that, as early as 659 AD, a silver paste was used to restore teeth in China [1]. Dental amalgam is an alloy of silver, copper, tin, and zinc combined with metallic mercury [46]. These particles combine with mercury to form 2-phase matrix:

- Gamma 1- binding of silver and mercury (Ag_2Hg_3)
- Gamma 2- binding of tin and mercury (Sn_7Hg)

Unreacted alloy particles create the gamma 2 phase, which is responsible for early fracture and failure of restorations; thus, copper percentage was increased to replace the tin-mercury phase with a copper-tin phase (Cu_5Sn_5). This matrix decreases the corrosion of tin, thereby strengthening the restoration [47].

There are two main types of amalgam:

- a conventional silver-tin amalgam made from a silver-tin alloy with small amounts of copper and zinc
- high copper amalgam made from an admixed alloy (a mixture of tin and silver-copper) of from a single alloy (ternary silver-copper-tin) [48]

Corrosion may occur when a non-metallic element reacts with a metal by an oxidation-reduction reaction [48], and in recent research, the measurements proved that the reaction between mercury and gold could make a roughness on gold [49]. So, the reactions generate some wanted and unwanted properties. One of the main pros of the reactions is the production of a self-sealing property in amalgam which decreases the chance of microleakage and protects the pulp and dentin. Dental amalgam restorations provide advantages over other dental restorative materials becuse they can be placed quickly, in a relatively wet field, while still maintaining high strength, durability, longevity and marginal integrity [50]. Amalgam placement (metallic alloys) is not a technique as sensitive as composite resins application, which require strict saliva and moisture control. Moisture contamination can cause delayed expansion especially in zinc-containing alloys [47], and this is an issue in countries like Portugal. To achieve maximum success, amalgam restorations require adequate retention as outlined by the principles by G. V. Black. Some common errors in cavity design (which weaken the restorations) include over-flaring of proximal outlines, leaving the flash on the margins, narrow isthmus width, preparation, etc. Moreover, some authors recommend a conservative resin restoration with a sealant for a small class I restorations [51]. Besides, the mercury and silver components in the amalgam also provides bacteriostatic properties

which aids in patients who have poor oral hygiene [52]. Overall, amalgam is a good restorative material solution for small to moderate sized interproximal lesions. When it comes to study the longevity of amalgam, with the increase in copper, amalgam has a higher survival rate than the conventional amalgam [53], and several studies show 12 years of durability in average [54]. Since it is not technique sensitive, the failures from the operator error and insufficient marginal adaptation are minimal. Between the two primary molars, first molars, amalgams have a higher failure rate and most amalgams failure occur between the first and second year after placement [55].

The existence of mercury in amalgam and its threats on human health has always been a topic of debate among scientists and researchers since last decades, being repetitively investigated the quantitative amount of mercury in blood [56]. Mercury (Hg) is a rare chemical element from the earth's crust. Its boiling point is 357 degrees Celsius, a melting point of -39 degrees Celsius and is insoluble in water, a good conductor of electricity and a poor conductor of heat [46]. One of the main reasons for moving over amalgam is due to mercury and its perceived toxicity. Thus, the effect of mercury on the kidney, brain, and immune function has been widely studied. Mercury is released from dental amalgam in several ways including chewing, tooth brushing, and ingestion of hot foods or liquids [57]. Despite encapsulating the silver-tin alloy, there are still concerns about the effects of inhalation of mercury vapor, ingestion of amalgam, allergy to mercury, and environmental burden [58]. A research in Germany, it was shown that the average amount of mercury in adults' blood without amalgam, is almost 1μg due to other environmental factors [59]. On the other hand, an investigation on 170 Spanish adults, shows a high increase of mercury amount in urine [60].

Although there are multiple claims that amalgam is deleterious due to its mercury content, there is no prosperous study that shows adverse health effects. This may be because of the low amount of mercury released from amalgam or the steps taken to minimize mercury toxicity. Not only the patients but also the dentist would be exposed by amalgam toxicity during the process, which makes a recommendation to use a high volume suction and the use of a rubber dam to decrease mercury exposure to the patient and the dental team [61]. Generally, to reduce the release of amalgam to the environment, chair-side traps, amalgam separator, vacuum pump filter, and line cleaners should be employed in every office [62].

2.3.2 Novel materials and methods

Dental composites were developed in the 1960s [63] and represented at the time a big revolution in clinical dentistry materials. One of the examples of the new generation of dental restorations is fused-porcelain-to-metal-teeth in 1962 [64]. Dental composites contain filler particles which are usually a type of glass or silicon dioxide. The greater filler, provides better physical properties, although it has to be optimized by a reduction in clinical handling. The improved performances of resin composites have encouraged more clinicians to select resin-based composites for posterior restorations as an alternative

to amalgam [65] because the adhesive technology allows restricted extraction of tooth substance beyond that required to eliminate caries and undermined enamel. The composites, being a not electrical conductor and not needing galvanism are taking good advantage over amalgams. Composites also combine an initiator to incept polymerization, and this can be mediated by chemical or by light activation. All the properties of the composites are dependent of their mechanical structure, containing three major substances, which are: the organic matrix, inorganic fillers accelerator, and initiator. The latter two together allow curing to take place in the presence of suppressors. The inhibitors increase the product storage life to its climax and make the color to be stable and eliminate the effect of UV light on the amine compounds in the initiator system, that might cause discoloration in the medium-long term [66]. The predominant base monomer used in commercial dental composites has been bis-GMA, which due to its high viscosity is mixed with methacrylates, such as TEGDMA, UDMA or other monomers. To determine the clinical indication for the commercial composites in the market, classification criteria were developed, mostly based on filler system. Their criteria are primarily based on the amount of inorganic filler fraction in volume percent or the particular filler size. Composites can be divided into classical, hybrids (including a composition of ground glass and microfill particles), and microfill composites. The microfills are further divided into subclasses including a characterization of the type of pre-polymerized resin fillers incorporated. Since the spherical fillers can be combined in a higher amount in a composite (in comparison to the irregular fillers of the same size and higher wear rate), the shape of the fillers is important [67]. It has been proved that microfill composites have the more ideal aesthetic qualities because of their high polishability and capability to retain and maintain surface smoothness over time [67]. However, these materials are not good for stress-bearing restorations, such as sharp edges and moderate to large stress bearing restorations in occlusal contact with opposing. This limitation is a consequence of their poor mechanical properties [68]. Recently, another classification system was introduced based on the filler volume fracture and filler size, distinguishes between densified composites, microfine composites, miscellaneous composite, and fibre-reinforced composite. The densified composites were subdivided into classes, a midway filled (<60 vol %) and compact-filled (>60 vol %) with a classification of ultrafine (<3μm) and fine (>3μm) within each category as a function of the mean particle size of the filler [69].

The main composition of composite resin includes:

- Fillers made of quartz, silica, or glass;
- Polymeric resin matrix;
- Silane coupling agents; and
- Other components such as pigments, stabilizers, a polymerization inhibitor, a photoinitiator, and radiopaque agents [70]

Fillers, defined by weight and volume, are a major constituent of composite resin materials [71]. The filler particles influence the properties of the composite, such as polymerization shrinkage, the

coefficient of thermal expansion, compressive strength, wear, water absorption, and translucency [70]. Historically, quartz has been used most often; however, it has been more recently replaced with colloidal silica, silica with barium, or lithium aluminum silicate. By increasing filler content, the compressive and tensile strengths, modulus of elasticity, and wear resistance are generally increased [72]. With round fillers, there is a higher filler content, allowing increased hardness and flexural strength, while mixed fillers have no linear relationship [72]. Also, the filler induced translucency can be varied with the heterogeneity in the polymer matrix [73]. The mechanical properties of the composite have drastically improved with the creation of hybrid and nano-filled composites, thus starting to overcome some of its inadequacies.

A quick milling process would help to make the waiting time shorter when the tooth should be prepared and to be placed. Thus, it's necessary to assess the machinability of the CAD/CAM materials. In a recent experimental work [74], it was revealed that the machinability of Lava Ultimate and Enamic is more than for e.max CAD and Celtra Duo and furthermore, they showed that the feed rate could be pushed up for the polymer-containing materials and as a result, milling time will be less.

Generally, brittleness of the ceramic-based CAD/CAM materials is more than polymer-containing CAD/CAM materials, and it causes edge chipping more likely to happen in ceramic-based materials [74].

Since there are a variety of commercial CAD/CAM materials in the market, in this work Filtek ™ Z250, Filtek ™ Z100 from 3M ™, and Herculite XRV Ultra ™ produced by Kerr are studied in the elasto-static regime. On the other hand, an elasto-plastic study is performed on Filtek ™ Z250 and Tetric N-Ceram Bulk ™ produced by Ivoclar Vivadent ™ (because these two materials show experimentally an evident elasto-plastic behaviour).

By 1992, 3M™ introduced Filtek ™ Z100 ™ for the first time which provided very good aesthetics, strength and wear resistance for the dentists. The studies by Creighton University and also University of Manitoba revealed some certain attributes for this product as follow and made it be an acceptable material for the posterior restorations:

- Retention
- Colour match
- Anatomic form
- Marginal adaptation
- Marginal discoloration
- Axial contour
- Proximal contact
- Secondary caries and
- Post-operative sensitivity

Ideally, the wear of material from composite restorative must match that of enamel in the occlusal contact situation for the enamel on enamel. So, the third study made by Catholic University at Leuven examined the wear of this material using a computerized measuring technique accurate to within 1 micron. The 4-year study indicated similar wear to Amalgam, and the wear rate of Z100 ™ on enamel in occlusal contact areas became comparable to the occlusal contact wear for enamel [75].

In 1999, 3M ™ introduced Z250 ™ with better quality in comparison to Z100 ™ regarding: aesthetics, resistance to fracture, resistance to marginal discoloration, and wear resistance. Furthermore, Z250 ™ has excellent handling for the dentists. This product receives the top ratings from dentists since it was introduced [76].

According to the material properties shown in table 2.2, Z100™ shows a higher Young's modulus in comparison to others and also a higher tensile and compressive strength.

Material	Young's modulus (MPa)	Poisson's ratio	Flexural strength (MPa)	Compressive strength (MPa)	Tensile strength (MPa)
Filtek Z250™	11,000 [77]	0.31 [78]	155 [75]	405 [75]	85 [75]
Filtek Z100™	14,500 [77]	0.3 [78]	135 [75]	470 [75]	105 [75]
Herculite XRV Ultra™	8,200 [77]	0.3	135 [79]	462 [79]	80 [77]

Table 2. 2. Material properties for the commercial dental restorative materials for elasto-static study

In a blind survey, in which 117 dentists participated, Filtek ™ Z250 ™ stands in the first ranks in universal preference (both anterior and posterior) by the specialists, Herculite XRV ™ stands in 2nd and Z100 ™ in the 3rd place.

In this work, Tetric N-Ceram Bulk ™ and Filtek Z250™ are chosen for the elasto-plastic analysis and the related mechanical properties are shown in table 2.3.

Material	Young's Modulus (MPa)	Plastic Modulus (MPa)	Yield Stress (MPa)
Filtek Z250™	11,000 [77]	5263[80]	100[80]
Tetric N-Ceram Bulk ™	10,000 [81]	2250[80]	85[80]

Table 2. 3. Material Properties for the commercial dental restorative composites for elasto-plastic study

2.3.3 Trends in restorative material choice in Europe

In parts of Europe, there has been a move to a "post amalgam era" in the pediatric population [82]. An increase in the use of composite resin has been noted in Norway, Finland, Germany, Italy, and Denmark for Class III, IV, and V restorations [83]. In Belgium, a national survey was administered in 1983 and again in 1988 to assess the types of restorative materials used for proximal lesions. In 1983, amalgam was preferred most frequently at 59% but dropped significantly to 20% in 1988 [84]. Also, the technique for placing composite resin changed significantly as well. In 1983, 18% of dentists seldom used acid etching for placing composite resins but in 1988, 69% reported using acid etching. There was a correlation with older dentists more frequently placing composite resins without acid etching, but it was not statistically significant. Another significant finding was that in 1983, 66% of practitioners never used composite resin for Class II restorations, while five years later, this percentage dropped to 15%.

In Finland, the use of amalgam for children dramatically decreased in the 1990s [82]. In 1994, GIC was being used for 47% of permanent tooth restorations in children [85]. This trend decreased to 40% among children and 19% among adults in 1997, and in 2003, the most common restorative material to restore primary molars was resin-modified glass ionomer (8-57%) [82], [86]. For the primary dentition, amalgam was never used [82]. In patients older than 17 years old, composite was used often (74.9%), and resin-modified glass ionomer and amalgam were rare used [86].

Additionally, in 1987-88, 6% of all tooth-colored restorations, mainly Class II restorations in primary teeth, were GIC [87]. GIC increased in popularity until it attained its highest rates in Finland and Norway at approximately 25% [88]. In 1996, a survey of general dentists in Norway found that 85% of all restorations placed in children were tooth-colored restorations with the majority being glass ionomer or resin-modified glass ionomers [88]. In the second survey, in 2001, at ten randomly selected public dental clinics; 46% of all restorations were glass ionomer or resin-6 modified glass ionomer, 38% were compomers, 5% was an amalgam, 2% was composite, and 9% were other. To assess material longevity, the new restorations placed in 1996 were reassessed; the median longevity for amalgam restorations in primary teeth was three years, while tooth-colored restorations were two years [88]. The paper alludes that the restorations were assessed in December 2000- January 2001 but the follow-up time is unclear. Besides, it is not stated how many restorations were lost to follow-up. In a study assessing 4030 Class II restorations by 27 general dentists in the Public Dental Health Service from 2001-2004; composite was used 81.5% of the time, compomer at 12.7%, amalgam at 4.6%, and glass ionomer at 1.2% [89]. Amalgam was more often used; in the treatment of patients with a higher reported decayed-missing-filled tooth (DMFT), in deep caries (9.1%) versus shallow caries (2.9%), and in molars (8.1%) rather than premolars (1.5%) [89]. In 2002, the Norwegian Directorate of Health reported that composite is the preferred restoration for general dentists and the proportion of amalgam restorations for children was reduced by

about 90% since 1995. The perceived toxicity of amalgam was secondary to the concern regarding the environmental impact of mercury.

In Sweden, researchers found that the majority (93%) of all new restorations were restored with composite resin [90],[83]. Whereas in 2001, only 2.9% of Swedish dentists used amalgam to restore primary occlusal caries, while there was a more positive response for the use of amalgam in Norway (19.9%) and Denmark (52.4%) [90]. When restoring with amalgam, a traditional Class II preparation was most commonly used in contrast to a tunnel preparation for glass ionomer restorations and saucer-shaped cavity design for composite resins [90].

In a survey of general dentists in Croatia, 66% chose composite resin as the preferred material for proximal caries [91]. Of these dentists, 46% preferred tunnel preparations versus traditional Class II or saucer type preparations. There was a significant relationship with dentists younger than 45 years old preferring tunnel preparations, while older respondents preferred traditional Class II preparations ($p= 0.017$).

2.4 Background on numerical studies of dental restorations

Investigation of dental restorations began decades ago (about 40 years) [92] and thanks to technological progress, computer-aided studies have been recently improved the methods and techniques of this field. Since during mastication a force of 100-1000 N is apply on teeth [93],[94], stress can generate on the teeth contact forces capable of creating a corresponding strain deformation on teeth [44]. Thus, studying the mechanical behaviour of natural teeth and also restored teeth is a relevant research topic. In this section, the numerical investigations on the mechanical behavior of the materials will be discussed.

It is not so common to find a significant amount of works on numerical studies dealing with fatigue on dental restorations, which is a production of a combination of FEM and S-N fatigue behavior [95]. In reality, the failure of a restored tooth can be consequences of cyclic chewing forces. As it is mentioned in 2.3.2, from 1962 fused-porcelain-to-metal-teeth has been introduced and used by dentists, and obviously, from that time, the demand of analysis to predict and determine the strength and other mechanical properties has become a priority to scientists. Since almost 1990, the dental restorations' analysis has entered a new era. Thus, the techniques and theory has been improved, and the new generation of analyses has been developed. Reid et al. [96], investigated fatigue and wear of dental materials and presented a study on crack growth. In 1967 an experimental investigation, based on static stress analysis, was performed and published in two parts. The research work focused mostly on finding the regions with stress concentration and some solutions to improve the quality of the restorative materials [97],[98].

Two of the most-common failures occurring in restored teeth with resin-composites are microleakage and failure of tooth tissue. The applied stress would be more effective in weak regions, and in this case, if the operator makes a good-quality and well-bonded restoration, the weak region may be the interface of composite and tooth [99]. In 2012, an investigation was done on this field, using a 3D finite element method analysis [100]. Nevertheless, another study was on the process of polymerization of the dental composite resin restoration using spring elements with different stiffness parameters, and finally, a correlation between the stiffness and higher shrinkage stresses was found [101]. The schematic model which is used in this work is represented in Figure 2.4. The interface of the composite resin and enamel has been constituted of spring elements. In this analysis, not only Young's modulus and Poisson's ratio, but also the thermal coefficient of expansion was used as the material properties for dentin, enamel and composite resin due to inherence of the work.

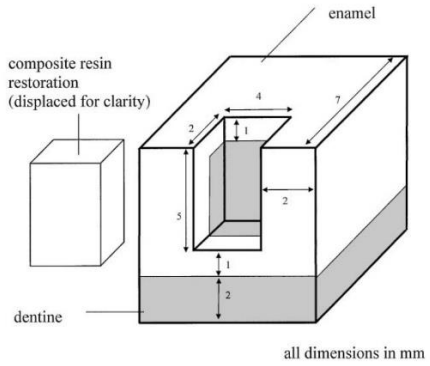

Figure 2. 4- Schematic diagram of the model [101]

Chapter 3

Biosystem of bone and tooth

3.1. Bone Morphology

Bones can be categorized into five types, i.e., long, short, flat, sesamoid and irregular. Long bones include the femora, tibiae, fibulae, humeri, radii, ulnae, metacarpals, metatarsals, phalanges, clavicles, which provide support and are requested to withstand most of the load during everyday activities. The shafts of the long bones are referred to as the diaphysis and the expanded ends as the epiphyses.

3.1.1 The macroscopic composition of bone

In a macroscopic scale, a normal bone is composed of the: **periosteum**, which covers bone, protecting from the tissues surrounded and provides cells for bone growth and repair; **articular cartilage** which covers the ends of the epiphyses; the **ossified tissue** and **bone marrow** which fills the medullary cavity and the spaces between the trabeculae, see Figure 3.1. It works like a storage for precursor cells, which participate in the repairing and fixing. The **endosteum** is also included in bone's composition, and consists of the inner surfaces of the bone.

The **periosteum** is a 1-2 mm wide membrane consisting of connective tissue that encloses the whole bone apart from the articular surface. It is comprised of two-layer, i.e., the **osteogenic** including progenitor cells, and the fibrous, including nerves and blood vessels. The ossified tissue is non-homogeneous, porous and anisotropic. It is divided into cortical, compact, cancellous and trabecular bone. Most of a long bone (around 80%) is constituted of cortical bone. The epiphyses are comprised of

cancellous bone whereas the diaphysis is mostly composed of compact bone, which is covered with a thin layer if cancellous in the inner surface around the bone marrow.

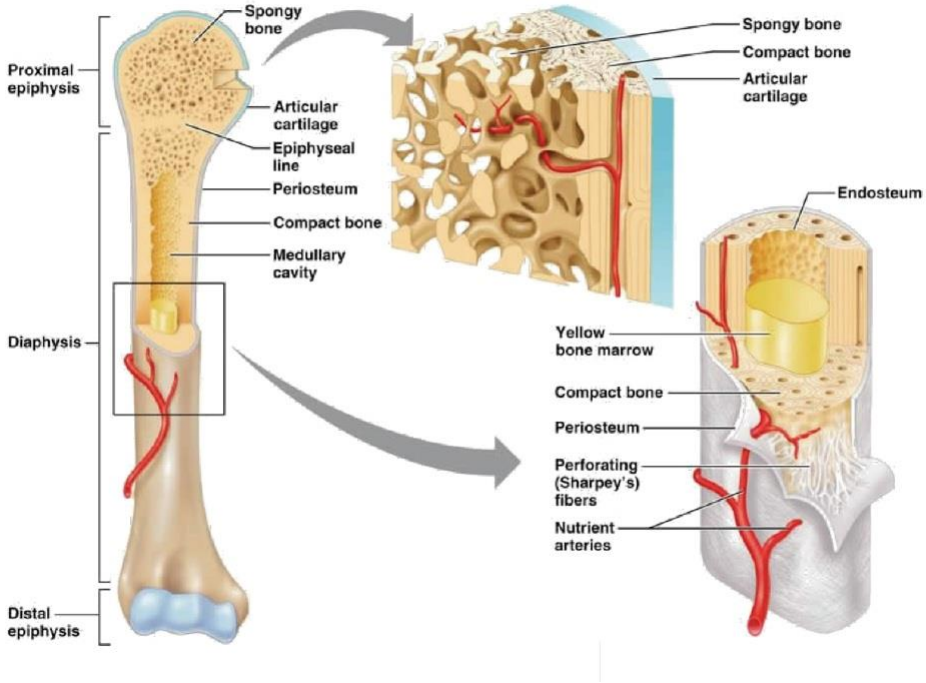

Figure 3. 1- Bone Structure [102]

Cortical bone includes systems of concentric lamellae as well as the Harvesian systems or osteons, which are the basic structural unit of cortical bone. Osteons are cylindrical or elliptical of 100-300 μm diameter and 10 mm long [103], [104]. 3-8 lamellae are wrapped around each osteon. The Harvesian canal of 50-100 μm long constitutes the central canal of the osteons. Harvesian canals include vessels, nerves and, connective tissue. Canaliculi pass through each osteon and, Volkman canals are also composed of vessels and nerves, placed in a transverse plane of that of the Harvesian canals. Volkman canals help in the communication between Harvesian canals and bone marrow, see Figure 3.1. According to an ultrasound testing technique, the elasticity modulus obtained 10.4 GPa for trabeculae, and 18.6 GPa for cortical [105]. This is probably due to microstructure, mineralization, and collagen fiber orientation differences of two tissue types[106].

3.1.2 The microscopic composition of bone

Bone is composed of the organic phase, inorganic phase, and water. The most important constituent of the organic phase is collagen, i.e., a protein organized into strong fibers, which provide bone with flexibility and tensile strength. Each collagen fibre has a diameter of 0.5 μm [103]. Proteoglycans and non-collagenous proteins also constitute the organic phase. The inorganic phase mostly includes hydroxyl apatite crystals and provides compressive strength and rigidity to bone [107]. In macroscopically level, although cortical and trabecular bone are different by their degree of porosity or density [108],[109], true differentiation comes from his histological evaluation of the tissue's microstructure [110].

A very small fraction of the bone's volume consists of cells that are responsible for the production, resorption, and maintenance of the above-described bone matrix:

Osteoblasts which are mononuclear cells differentiated from mesenchymal stem cells. Once they are stimulated, they change their shape and form new ossified organic matrix, i.e., osteoid. This osteoid is produced at a rate of 1 $\mu m/day$ and is then calcified to create mineralized bone. When they are deactivated, they become flattened and form cells to the free bone surfaces or are self-vested with mineral matrix and become **osteocytes**.

Osteocytes which are former osteoblasts sitting in cavities inside the organic matrix, i.e. the lacunae. They have an oval shape and stick out in small canals, the canaliculi, where they are connected with other osteocytes and osteoblasts. Their role is to sustain organic bone matrix and release calcium ions from the organic matrix when it is necessary. A small amount of osteocytes absorbs organic mineral matrix, which shows that these cells play a significant role in the conservation of the bone organic matrix [111].

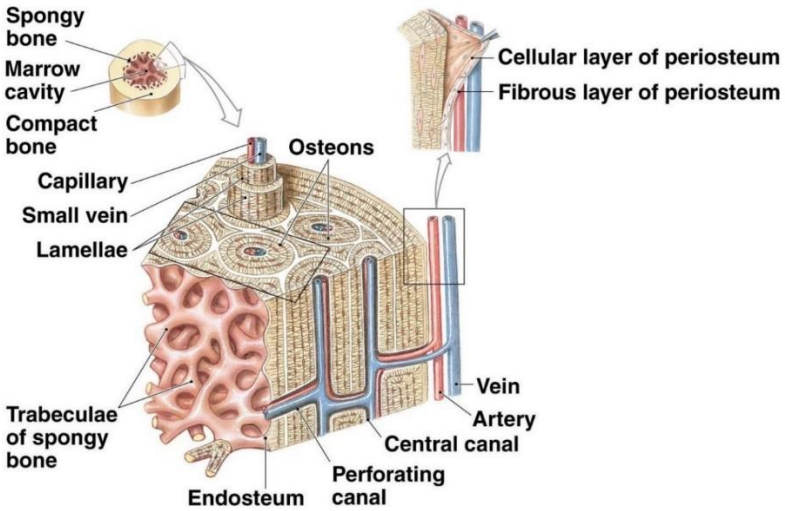

Figure 3. 2- Microstructure of bone [102]

Osteoclasts that are multinuclear cells and come from precursors of bone marrow. They are responsible for bone absorption. This process is ensured by a large number of mitochondria existing in their cytoplasm. The cytoplasm membrane creates an acid environment in which the organic matrix loses its metallic ions and is dissolved. Bone resorption takes place at a rate of tens of micrometers per day. The cooperation of osteoblasts and osteoclasts is responsible for the form, remodeling, and healing of bone tissue. The concept of remodeling which mentioned is referred to a complex regenerative process that gradually restores the functional and mechanical bone properties and leads to fracture healing.

3.2. Tooth

There are usually 32 teeth in the adult human which are separated equally into two arches: the upper arch (maxilla) and the lower arch (mandible), see Figure 3.3. Depending on their position in the arch, teeth are divided into either anterior or posterior teeth. Normally in each arch, the anterior teeth consist of incisors and canines which aid in cutting and shearing the food, while the posterior consists of premolars and molars which help in the mastication of food [112],[113]. Each human tooth is anatomically separated into a crown and one or more roots. The anatomical crown is composed of an inner soft tissue (pulp chamber) enveloped with a relatively harder tissue called dentine that is further surrounded by one of the hardest tissues in the human body known as enamel [114],[115]. The junction between the pulp chamber and dentine is called dentin-pulpal junction (DPJ), whereas the junction between the dentine and enamel is known as the dentin-enamel junction (DEJ) [112], [114]. Mechanical properties (Young's modulus and Poisson's ratio) for different parts of a human tooth are shown in table 3.1.

Materials	Young's modulus (MPa)	Poisson's ratio
Dentine	1.86×10^4	0.31
Enamel	4.1×10^4	0.3
Pulp	20	0.45
Periodontal Ligament	68.9	0.499
Cortical bone	1.37×10^4	0.30
Cancellous bone	1.37×10^3	0.28

Table 3. 1- The mechanical properties attributed to the materials of a human tooth [116]

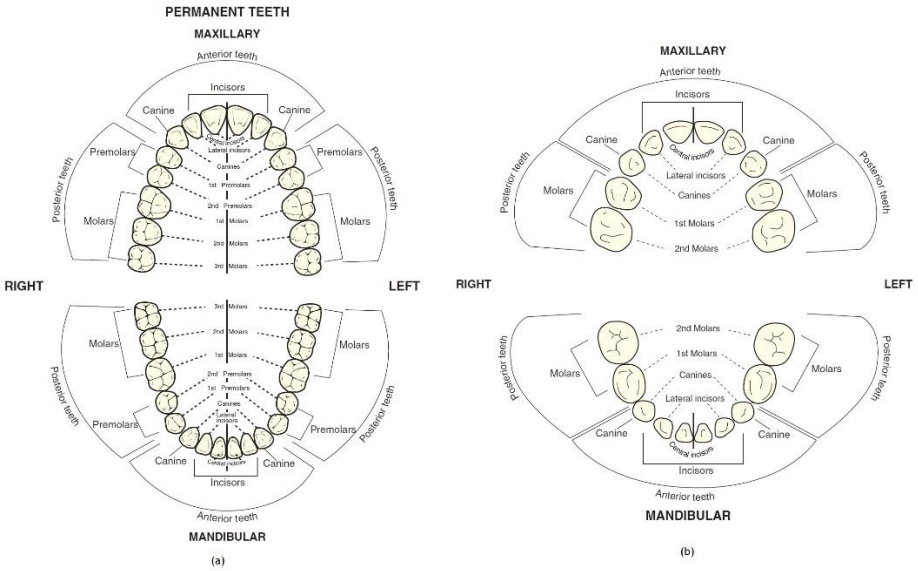

Figure 3. 3- (a) Maxillary and permanent mandibular dentition. (b) Maxillary and mandibular primary dentition [117]

The scientific interest about the anatomy of jaw and dentition is not a new concept. Traditionally it has been one of the main topics which have made the scientists to develop methods and software to investigate scrupulously this field [118],[119],[120]. In this chapter, each major parts of a human tooth will be described and also within the different tooth types, premolars and molars will be focused on this work.

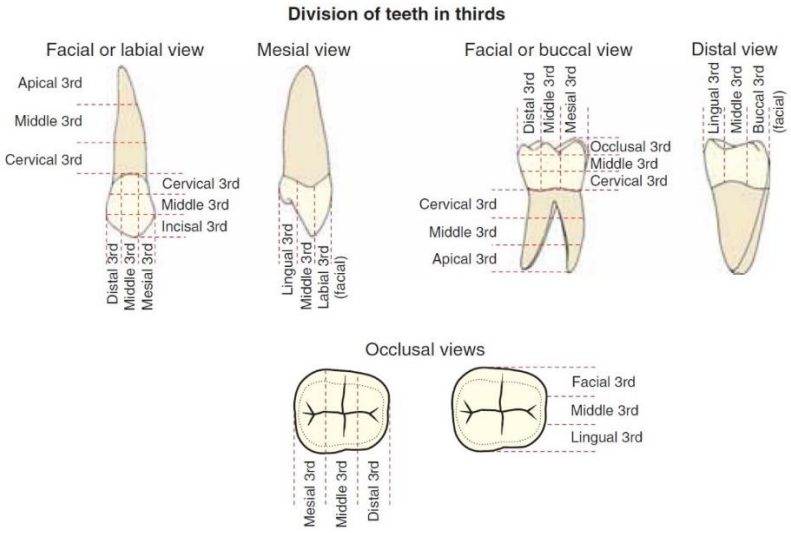

Figure 3. 4- Diagrams of a maxillary canine and mandibular molars to show how a crown or root may be divided into thirds from each view for the purpose of describing the location of anatomic landmarks, contact areas [117]

3.2.1 Morphology of premolars and molars

There are four premolars in the maxillary arch, and four in the mandibular arch, see Figure 3.3. Both upper and lower premolars' function with molars is to masticate food and to maintain the vertical dimension of the face (between nose and chin). First premolars assist the canines in shearing or cutting food morsels, and all premolars support the mouth and cheeks to avoid sagging. Furthermore, from the **aesthetic** aspect, while smiling or laughing, premolars play a significant role [117]. Some properties are referring to premolars which are similar to anterior teeth. **The number of developmental lobes** is similar to the anterior teeth. The facial surfaces of all premolars develop from three facial lobes. Premolars' crown from facial, is narrower in the cervical third than occlusal, see Figure 3.5.

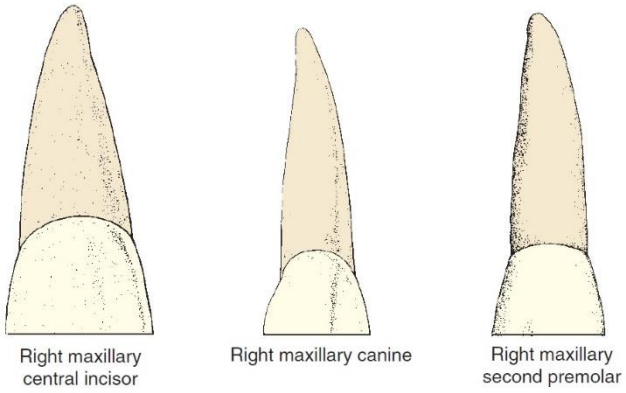

Figure 3. 5- Facial views of an incisor, canine, and premolar with the incisal/occlusal thirds of the crowns removed[117]

To give an idea about the facial definitions of a tooth, in figure 3.6, some external tooth line angles and point angles for a molar tooth are described (Mesial, Lingual, Buccal, and Distal). Nevertheless, similar to anterior teeth, cervical lines, curve along with the biting surfaces (occlusal or incisal) and the amount of curvature is slightly higher on the distal surface. Furthermore, root shape of premolars is similar to anterior teeth. Contrary to the anterior teeth, instead of incisal ridges, premolars have occlusal surfaces which they have cusps, ridges, and grooves.

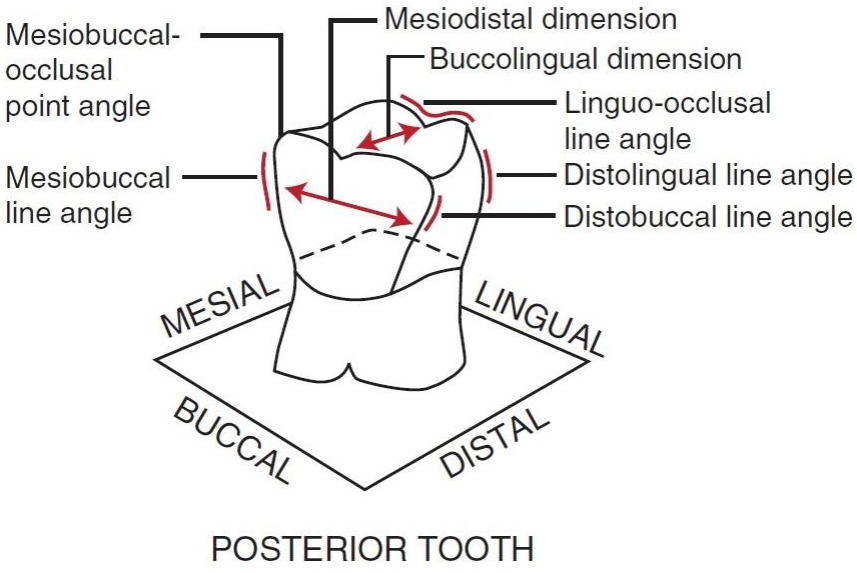

Figure 3. 6- Diagrammatic representation of molar crown shows some external tooth line angles and point angles [117].

Mandibular premolars due to their complicated root canals have always been considered the most difficult case in treatment. Because of this complexity, it is necessary to follow some principles to address the problem [121].

According to figure 3.7, being the mandibular premolar three-cusp is unique. Since it is the only premolar that has three triangular ridges (one per cusp).

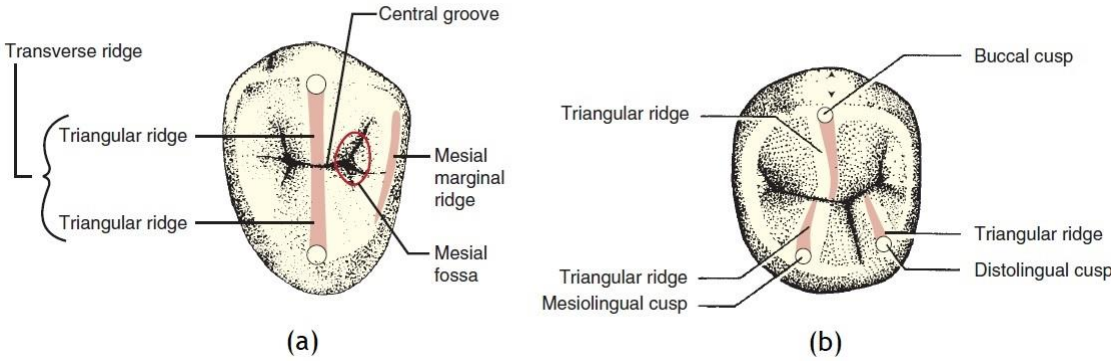

Figure 3. 7- (a) Typical two-cusp type premolar (maxillary second) (b) The mandibular second premolar, three cusp type[117]

In table 3.2 and table 3.3, the data according to the measurement of maxillary and mandibular premolars is shown. This measurement has been accomplished by Dr. Woelfel and his dental students

from 1974 to 1979 [117]. The premolar crowns are shorter than the canines and longer than those of molars. The root canal lengths are similar to molars but shorter than canines [122]. The difference in measurement for different cases is dependent on genetics and environmental influences [123].

	234 first premolars		224 second premolars	
Dimension measured	Average	Range	Average	Range
Crown length	8.6	7.1-11.1	7.7	5.2-10.5
Root length	13.4	8.3-19.0	14.0	8.0-20.6
Overall length	21.5	15.5-28.9	21.2	15.2-28.4
Crown width (mesiodistal)	7.1	5.5-9.4	6.6	5.5-8.9
Root width (cervix)	4.8	3.6-8.5	4.7	4.0-5.8
Faciolingual crown size	9.2	6.6-11.2	9.0	6.9-11.6
Faciolingual root (cervix)	8.2	5.0-9.4	8.1	5.8-10.5
Mesial cervical curve	1.1	0.0-1.7	0.9	0.4-1.9
Distal cervical curve	0.7	0.0-1.7	0.6	0.0-1.4

Table 3. 2- Size of maxillary premolars (millimeters) [117]

	234 first premolars		224 second premolars	
Dimension measured	Average	Range	Average	Range
Crown length	8.8	5.9-10.9	8.2	6.7-10.2
Root length	14.4	9.7-20.2	14.7	9.2-21.2
Overall length	22.4	17.0-28.5	22.1	16.8-28.1
Crown width (mesiodistal)	7.0	5.9-8.8	7.1	5.2-9.5
Root width (cervix)	4.8	3.9-7.3	5.0	4.0-6.8
Faciolingual crown size	7.7	6.2-10.5	7.3	6.1-8.4
Faciolingual root (cervix)	7.0	5.5-8.5	7.3	6.1-8.4
Mesial cervical curve	0.9	0.0-2.0	0.8	0.0-2.0
Distal cervical curve	0.6	0.0-1.6	0.5	0.0-1.3

Table 3. 3- Size of mandibular premolars (millimeters) [117]

There are six permanent molars in both maxillary and mandibular which means there are 12 permanent molars totally. The first molar is distal to the last premolar and a loss of molars would allow movement of teeth in both sides. Morphology of molars can change in a long time, and a study in India showed a considerable change due to developmental variation or an evolutionary change [124]. Permanent molars are considered as the largest and strongest teeth in each arch, and they play a significant role in the chewing like the premolars as mentioned previously.

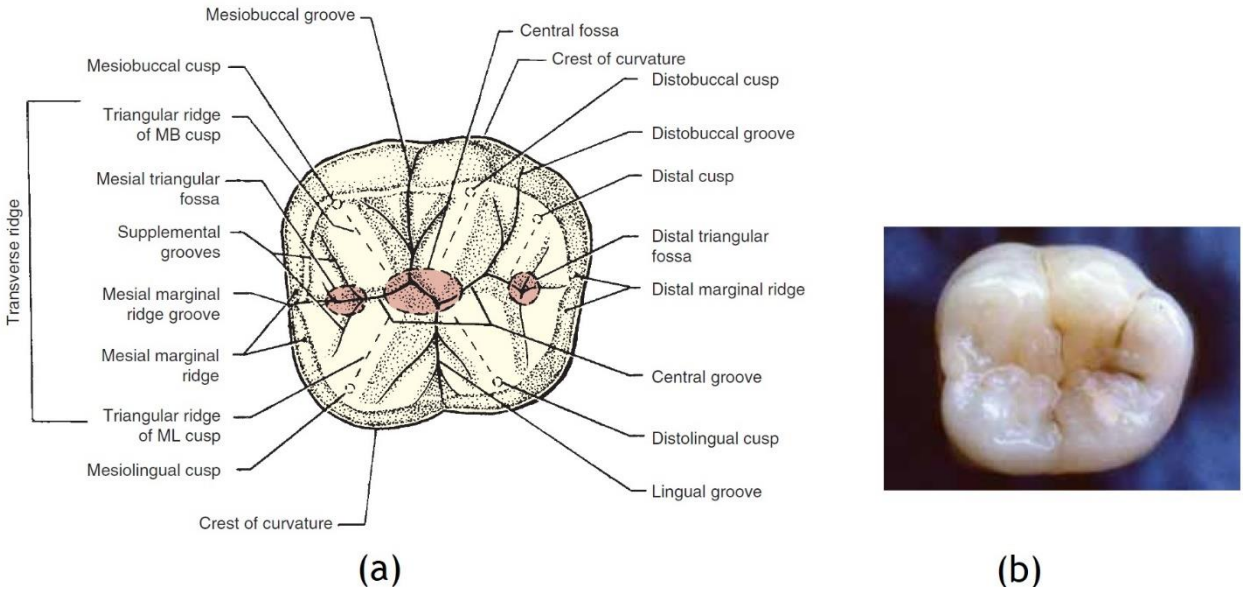

Figure 3. 8- (a) occlusal view of a mandibular molar (b) Occlusal anatomy of a mandibular molar [117]

Chapter 4

Solid Mechanics

4.1. Fundamentals

Solid mechanics deals with the relationship between stress, strain, and displacement. Rotation and/or a strain are the product of the deformation on a body. Thus, Cauchy stress tensor is a symmetric matrix represented in equation 4.1.

$$\boldsymbol{\sigma} = \begin{bmatrix} \sigma_{xx} & \sigma_{xy} & \sigma_{xz} \\ \sigma_{yx} & \sigma_{yy} & \sigma_{yz} \\ \sigma_{zx} & \sigma_{zy} & \sigma_{zz} \end{bmatrix} \tag{4.1}$$

The strain tensor is equivalent to the Cauchy stress tensor. Also, it is possible to reduce the stress tensor and strain tensor to a stress vector and strain vector, respectively, as it is shown in equation 4.2 and 4.3.

$$\boldsymbol{\sigma} = \begin{Bmatrix} \sigma_{xx} & \sigma_{yy} & \sigma_{zz} & \sigma_{xy} & \sigma_{yz} & \sigma_{xz} \end{Bmatrix}^{\boldsymbol{T}} \tag{4.2}$$

$$\boldsymbol{\varepsilon} = \begin{Bmatrix} \varepsilon_{xx} & \varepsilon_{yy} & \varepsilon_{zz} & \varepsilon_{xy} & \varepsilon_{yz} & \varepsilon_{xz} \end{Bmatrix}^{\boldsymbol{T}} \tag{4.3}$$

To make a relation between stress rate and strain rate, a material constitutive matrix is necessary to be established. The stresses and the strains of the material inside a continuous elastic material are connected by a linear relationship that is mathematically similar to Hooke's spring law [125]. This law is commonly applied to elastic materials. Nevertheless, recently this law was extended to other types of

materials such as viscoelastic materials [126], [127]. The following relation in equation 4.4, also can be written as equation 4.5, where the $\boldsymbol{s} = \boldsymbol{c}^{-1}$ and the matrix for a 3-dimensional case as in equation 4.6.

$$d\boldsymbol{\sigma} = \boldsymbol{c}\, d\boldsymbol{\varepsilon} \tag{4.4}$$

$$d\boldsymbol{\varepsilon} = \boldsymbol{c}^{-1} d\boldsymbol{\sigma} \tag{4.5}$$

$$\boldsymbol{s} = \boldsymbol{c}^{-1} = \begin{bmatrix} \frac{1}{E_{xx}} & -\frac{\nu_{yx}}{E_{yy}} & -\frac{\nu_{zx}}{E_{zz}} & 0 & 0 & 0 \\ -\frac{\nu_{xy}}{E_{xx}} & \frac{1}{E_{yy}} & -\frac{\nu_{zy}}{E_{zz}} & 0 & 0 & 0 \\ -\frac{\nu_{xz}}{E_{xx}} & -\frac{\nu_{yz}}{E_{yy}} & \frac{1}{E_{zz}} & 0 & 0 & 0 \\ 0 & 0 & 0 & \frac{1}{G_{xy}} & 0 & 0 \\ 0 & 0 & 0 & 0 & \frac{1}{G_{yz}} & 0 \\ 0 & 0 & 0 & 0 & 0 & \frac{1}{G_{zx}} \end{bmatrix} \tag{4.6}$$

The elements on matrix $\boldsymbol{s} = \boldsymbol{c}^{-1}$ are determined experimentally, allowing to define the material's anisotropic mechanical properties. E_{ii} is the young's modulus in direction i, ν_{ij} is Poisson's ratio which shows the deformation in j direction when the force is applied in i direction. Furthermore, G_{ij} is the shear modulus which characterizes the variation of angle between i and j.

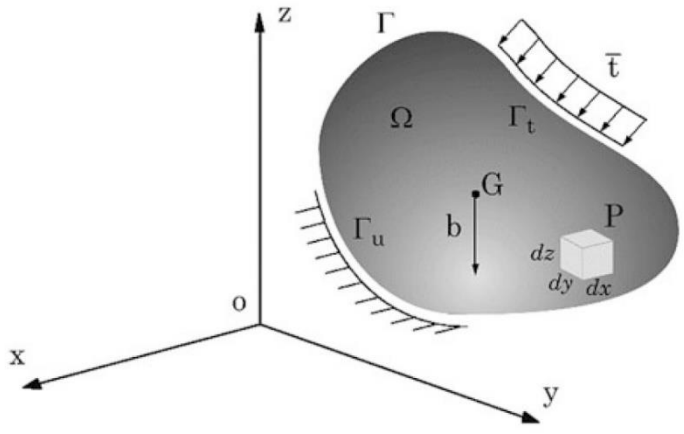

Figure 4. 1- Continuous solid domain under volume forces and external forces[128].

The continuous solid domain (Ω) , bounded by a natural boundary (Γ_t) (denoted to external forces) and also essential boundary (Γ_u) (denoted to the boundary, in which the displacement is constrained), see Figure 4.1. The displacement field in three directions can represented as in equation 4.7. By considering the 6 distinct stress and strain components on an infinitesimal cubic volume, the matrix of partial differential operators, $\boldsymbol{L}$ can be obtained (equation 4.8) and the relation between displacement field and the strain field can be written as equation 4.9.

$$\boldsymbol{u} = \begin{Bmatrix} u(x,y,z) \\ v(x,y,z) \\ w(x,y,z) \end{Bmatrix} \tag{4.7}$$

$$\boldsymbol{L} = \begin{bmatrix} \partial/\partial x & 0 & 0 & \partial/\partial y & \partial/\partial z & 0 \\ 0 & \partial/\partial y & 0 & \partial/\partial x & 0 & \partial/\partial z \\ 0 & 0 & \partial/\partial z & 0 & \partial/\partial x & \partial/\partial y \end{bmatrix} \tag{4.8}$$

$$\boldsymbol{\varepsilon} = \boldsymbol{L}\,\boldsymbol{u} \tag{4.9}$$

Thus, the strain components are obtained from the derivatives of the displacement field components as explicitly shown in equation 4.10.

$$\begin{aligned} \varepsilon_{xx} &= \partial u/\partial x \\ \varepsilon_{yy} &= \partial v/\partial y \\ \varepsilon_{zz} &= \partial w/\partial z \\ \gamma_{xy} &= \partial u/\partial y + \partial v/\partial x \\ \gamma_{yz} &= \partial v/\partial z + \partial w/\partial y \\ \gamma_{xz} &= \partial u/\partial z + \partial w/\partial x \end{aligned} \tag{4.10}$$

A force balance should be performed by obtaining static equilibrium equations of elasticity, considering all the directions, as it is indicated in equation 4.11.

$$\frac{\partial \sigma_{xx}}{\partial x} + \frac{\partial \tau_{xy}}{\partial y} + \frac{\partial \tau_{xz}}{\partial z} + F_x = 0$$

$$\frac{\partial \tau_{xy}}{\partial x} + \frac{\partial \sigma_{yy}}{\partial y} + \frac{\partial \tau_{yz}}{\partial z} + F_y = 0 \tag{4.11}$$
$$\frac{\partial \tau_{xz}}{\partial x} + \frac{\partial \tau_{yz}}{\partial y} + \frac{\partial \sigma_{zz}}{\partial z} + F_z = 0$$

4.2. The weak form of Galerkin

Although it is preferable to obtain an exact solution utilizing strong form of equations, such calculus is a very difficult task in complex practical engineering problems, which leads to the necessity of using a weak form. The weak form of Galerkin has attracted much attention in the field of numerical partial differential equations [129], [130], [131]. In a Galerkin formulation, numerical integration is usually achieved evaluating the integrals in the weak form. As it will be discussed in the next chapter, in the finite element method (FEM), Gaussian quadrature is used in each element, and the support of the shape functions are used for integration. In meshless methods, the integration cells are usually constructed independently of the shape functions [132]. Generally, the weak form of the system equations is normally obtained by two main methods: energy principals, and weighted residual methods, and weak form of Galerkin employs the energy principals named Hamilton's principal [133]. Considering the solid mechanics, in equation 4.12, T represents kinetic energy, U the strain energy, and W_f is the work produced by external forces. Hamilton's principal could be shown mathematically as equation 4.13 and, with combination of the both prior equations, the 4.14 would be obtained [134].

$$L = T - U + W_f \tag{4.12}$$
$$\delta \int_{t_1}^{t_2} L dt = 0 \tag{4.13}$$
$$\delta \int_{t_1}^{t_2} \left(T - U + W_f\right) dt = 0 \tag{4.14}$$

The kinetic energy is defined by equation 4.15, where the Ω defines solid volume and $\dot{\boldsymbol{u}}$ is the displacement first derivative with respect to time, representing the velocity. Furthermore, ρ is the density of the material.

$$T = \frac{1}{2}\int_{\Omega} \rho \dot{\boldsymbol{u}}^T \dot{\boldsymbol{u}}\, \mathrm{d}\Omega \tag{4.15}$$

The strain energy, for elastic materials, is defined as equation 4.16.

$$U = \frac{1}{2}\int_{\Omega} \boldsymbol{\varepsilon}^T \boldsymbol{\sigma}\, \mathrm{d}\Omega \tag{4.16}$$

Being the $\boldsymbol{\varepsilon}^T$ and $\boldsymbol{\sigma}$, the transposed strain vector and stress vector, respectively. The work produced by external forces can be expressed as equation 4.17.

$$W_f = \int_{\Omega} \boldsymbol{u}^T \boldsymbol{b}\, \mathrm{d}\Omega + \int_{\Gamma_t} \boldsymbol{u}^T \bar{\boldsymbol{t}}\, \mathrm{d}\Gamma \tag{4.17}$$

In equation 4.17, $\boldsymbol{b}$ shows the body force, $\boldsymbol{u}$ is the displacement and Γ_t the traction boundary where the external forces $\bar{\boldsymbol{t}}$ are applied. By substituting Lagrangian functional L can be written as equation 4.18.

$$L = \frac{1}{2}\int_{\Omega} \rho \dot{\boldsymbol{u}}^T \dot{\boldsymbol{u}}\, \mathrm{d}\Omega - \frac{1}{2}\int_{\Omega} \boldsymbol{\varepsilon}^T \boldsymbol{\sigma}\, \mathrm{d}\Omega + \int_{\Omega} \boldsymbol{u}^T \boldsymbol{b}\, \mathrm{d}\Omega + \int_{\Gamma_t} \boldsymbol{u}^T \bar{\boldsymbol{t}}\, \mathrm{d}\Gamma \tag{4.18}$$

After minimizing equation 4.18, by substituting in equation 4.14, and moving the δ inside the integrals, based on the linearity of operations, the order of operation can be changed without any effect on result, so equation 4.19 can be obtained by employing the chain rule of variation and then the scalar property for the first term of the integral above.

$$\int_{t_1}^{t_2} \delta\,(\rho \dot{\boldsymbol{u}}^T \dot{\boldsymbol{u}})\, \mathrm{dt} = \rho \int_{t_1}^{t_2} (\delta \dot{\boldsymbol{u}}^T \dot{\boldsymbol{u}} + \dot{\boldsymbol{u}}^T \delta \dot{\boldsymbol{u}})\, \mathrm{dt} = 2\rho \int_{t_1}^{t_2} (\delta \dot{\boldsymbol{u}}^T \dot{\boldsymbol{u}})\, \mathrm{dt} \tag{4.19}$$

Since $\dot{\boldsymbol{u}}^T \dot{\boldsymbol{u}}$ is a scalar and $\dot{\boldsymbol{u}} = \partial \boldsymbol{u}/\partial t$, then integration by parts, with respect to time, makes the first term of equation 4.18 to be as it is represented in 4.20.

$$\int_{t_1}^{t_2}\left[\frac{1}{2}\int_{\Omega}\rho\dot{\boldsymbol{u}}^T\dot{\boldsymbol{u}}\,\mathrm{d}\Omega\right]\mathrm{dt}=-\int_{t_1}^{t_2}\left[\rho\int_{\Omega}(\delta\boldsymbol{u}^T\ddot{\boldsymbol{u}})\mathrm{dt}\right] \tag{4.20}$$

Also, the second term of the 4.18, can be written as equation 4.21.

$$\delta(\boldsymbol{\varepsilon}^T\boldsymbol{\sigma})=\delta\boldsymbol{\varepsilon}^T\boldsymbol{\sigma}+\boldsymbol{\varepsilon}^T\delta\boldsymbol{\sigma}=\mathbf{2}\delta\boldsymbol{\varepsilon}^T\boldsymbol{\sigma} \tag{4.21}$$

Using the constitutive equation (4.4) and the symmetric property of the material matrix, $\boldsymbol{c^T}=\boldsymbol{c}$, it is possible to simplify the integrals, and the "Galerkin weak form" can be written as equation 4.22.

$$-\rho\int_{\Omega}(\delta\boldsymbol{u}^T\ddot{\boldsymbol{u}})\,\mathrm{d}\Omega-\int_{\Omega}(\delta\boldsymbol{\varepsilon}^T\boldsymbol{\sigma})\,\mathrm{d}\Omega+\int_{\Omega}(\delta\boldsymbol{u}^T\boldsymbol{b})\,\mathrm{d}\Omega+\int_{\Gamma_t}(\delta\boldsymbol{u}^T\bar{\boldsymbol{t}})\,\mathrm{d}\Gamma=0 \tag{4.22}$$

By considering the relation of stress and strain, and also strain and displacement, as it was previously mentioned in equation 4.4 and 4.9, the Galerkin weak form can be also written as 4.23.

$$\int_{\Omega}(\delta(\boldsymbol{Lu})^T\boldsymbol{c}(\boldsymbol{Lu}))\,\mathrm{d}\Omega-\int_{\Omega}(\delta\boldsymbol{u}^T\boldsymbol{b})\,\mathrm{d}\Omega+\int_{\Omega}\rho(\delta\boldsymbol{u}^T\ddot{\boldsymbol{u}})\,\mathrm{d}\Omega-\int_{\Gamma_t}(\delta\boldsymbol{u}^T\bar{\boldsymbol{t}})\,\mathrm{d}\Gamma=0 \tag{4.23}$$

The last equation is the generic Galerkin weak form written in terms of displacement and very useful in solid mechanics [128]. Take into account that in a static problem, the third term including acceleration will disappear.

4.3. Discrete system of equations

Through the principle of virtual work, the discrete system of equations is obtained for meshless methods. The trial meshless function $\boldsymbol{u}(\boldsymbol{x})_{\boldsymbol{I}}$ can be expressed as equation 4.24.

$$\boldsymbol{u}(\boldsymbol{x})_{\boldsymbol{I}}=\sum_{i=1}^{n}\varphi_i(\boldsymbol{x}_{\boldsymbol{I}})\boldsymbol{u}_{\boldsymbol{i}} \tag{4.24}$$

Where $\varphi_i(\boldsymbol{x_I})$ is the meshless method approximation (or interpolation) function and $\boldsymbol{u_i}$ are the nodal displacements for each *n* node which belongs to the influence-domain of the interest point $\boldsymbol{x_I}$.

The virtual displacements can be written as equation 4.25.

$$\delta \boldsymbol{u}(\boldsymbol{x_I}) = \sum_{i=1}^{n} \varphi_i(\boldsymbol{x_I}) \boldsymbol{\delta u_i} \tag{4.25}$$

By replacing the "Galerkin weak form" equation by equations 4.24 and 4.25, equation 4.26 can be drawn.

$$\begin{aligned} &-\int_{\Omega} \left(\sum_{i=1}^{n} \varphi_i(\boldsymbol{x_I}) \boldsymbol{\delta u_i} \right)^T \boldsymbol{L^T c L} \left(\sum_{i=1}^{n} \varphi_i(\boldsymbol{x_I}) \boldsymbol{\delta u_i} \right) d\Omega \\ &+ \int_{\Omega} \left(\sum_{i=1}^{n} \varphi_i(\boldsymbol{x_I}) \boldsymbol{\delta u_i} \right)^T \boldsymbol{b}\, d\Omega + \int_{\Omega} \left(\sum_{i=1}^{n} \varphi_i(\boldsymbol{x_I}) \boldsymbol{\delta u_i} \right)^T \bar{\boldsymbol{t}}\, d\Gamma = 0 \end{aligned} \tag{4.26}$$

In order to get rid of the sums, the equation can be replaced by matrix form. For the interest point $\boldsymbol{x_I}$ considering a 3D problem, the approximation or interpolation functions can be as follow in equation 4.27.

$$\varphi(\boldsymbol{x_I}) = \begin{bmatrix} \varphi_1(\boldsymbol{x_I}) & \mathbf{0} & \mathbf{0} & \varphi_2(\boldsymbol{x_I}) & \mathbf{0} & \mathbf{0} & \dots & \varphi_n(\boldsymbol{x_I}) & \mathbf{0} & \mathbf{0} \\ \mathbf{0} & \varphi_1(\boldsymbol{x_I}) & \mathbf{0} & \mathbf{0} & \varphi_2(\boldsymbol{x_I}) & \mathbf{0} & \dots & \mathbf{0} & \varphi_n(\boldsymbol{x_I}) & \mathbf{0} \\ \mathbf{0} & \mathbf{0} & \varphi_1(\boldsymbol{x_I}) & \mathbf{0} & \mathbf{0} & \varphi_2(\boldsymbol{x_I}) & \dots & \mathbf{0} & \mathbf{0} & \varphi_n(\boldsymbol{x_I}) \end{bmatrix} \tag{4.27}$$

The matrix of partial differential operators $\boldsymbol{L}$, as it is demonstrated in equation 4.8, can play the role to set the matrix of deformability $\boldsymbol{B}(\boldsymbol{x_I})$, for the interest point $\boldsymbol{x_I}$. This matrix would be obtained by multiplying $\varphi_i(\boldsymbol{x_I})$ and $\boldsymbol{L}$, as it is indicated in equation 4.28.

$$\boldsymbol{B_i}(\boldsymbol{x_I}) = \boldsymbol{L\varphi_i}(\boldsymbol{x_I}) = \begin{bmatrix} \frac{\partial \varphi_i(\boldsymbol{x_I})}{\partial x} & 0 & 0 & \frac{\partial \varphi_i(\boldsymbol{x_I})}{\partial y} & \frac{\partial \varphi_i(\boldsymbol{x_I})}{\partial z} & 0 \\ 0 & \frac{\partial \varphi_i(\boldsymbol{x_I})}{\partial y} & 0 & \frac{\partial \varphi_i(\boldsymbol{x_I})}{\partial x} & 0 & \frac{\partial \varphi_i(\boldsymbol{x_I})}{\partial z} \\ 0 & 0 & \frac{\partial \varphi_i(\boldsymbol{x_I})}{\partial z} & 0 & \frac{\partial \varphi_i(\boldsymbol{x_I})}{\partial x} & \frac{\partial \varphi_i(\boldsymbol{x_I})}{\partial y} \end{bmatrix}^{\boldsymbol{T}} \tag{4.28}$$

Finally, equation 4.26 by inserting equations 4.27 and 4.28 can be written as follow, in equation 4.29.

$$-\delta \boldsymbol{u}_I{}^T \int_\Omega \left[\left(\boldsymbol{\varphi}(\boldsymbol{x_I})\right)^T \boldsymbol{L}^T\right] \boldsymbol{c}[\boldsymbol{L}\boldsymbol{\varphi}(\boldsymbol{x_I})] d\Omega \boldsymbol{u}_I + \delta \boldsymbol{u}_I{}^T \int_\Omega \left(\boldsymbol{\varphi}(\boldsymbol{x_I})\right)^T \boldsymbol{b} d\Omega + \delta \boldsymbol{u}_I{}^T \int_{\Gamma^t} \left(\boldsymbol{\varphi}(\boldsymbol{x_I})\right)^T \bar{\boldsymbol{t}} d\Gamma = 0 \tag{4.29}$$

For each node in the influence-domain, the matrix $\boldsymbol{B}(\boldsymbol{x_I})$ is the result of combination of all *n* $\boldsymbol{B_i}(\boldsymbol{x_I})$ matrixes. Thus, the deformation matrix introduced in equation 4.26 becomes as follow in equation 4.30 that leads to the local static equilibrium equation for the influence-domain corresponding to the interest point $\boldsymbol{x_I}$ that can be written as it is demonstrated in equation 4.31.

$$\delta \boldsymbol{u}_I{}^T [- \int_\Omega (\boldsymbol{B}(\boldsymbol{x_I}))^T \boldsymbol{c} \boldsymbol{B}(\boldsymbol{x_I}) d\Omega \boldsymbol{u}_I + \int_\Omega \left(\boldsymbol{\varphi}(\boldsymbol{x_I})\right)^T \boldsymbol{b} d\Omega + \int_{\Gamma^t} \left(\boldsymbol{\varphi}(\boldsymbol{x_I})\right)^T \bar{\boldsymbol{t}} d\Gamma] = 0 \tag{4.30}$$

The first integral in the next equation (4.31), corresponds to the local stiffness matrix, $\boldsymbol{K_I}$, and the other two integrals can be grouped constituting the local force vector $\boldsymbol{F_I}$.

$$\int_\Omega (\boldsymbol{B}(\boldsymbol{x_I}))^T \boldsymbol{c} \boldsymbol{B}(\boldsymbol{x_I}) d\Omega \boldsymbol{u}_I - \int_\Omega \left(\boldsymbol{\varphi}(\boldsymbol{x_I})\right)^T \boldsymbol{b} d\Omega - \int_{\Gamma^t} \left(\boldsymbol{\varphi}(\boldsymbol{x_I})\right)^T \bar{\boldsymbol{t}} d\Gamma = 0 \tag{4.31}$$

Then, considering the nodal connectivity which will be discussed in the next chapter, the previous local stiffness matrixes should be assembled, leading to the global discrete system of equations like in equation 4.32, where ***K*** is the global stiffness matrix, ***u*** is the global nodal displacement vector and ***F*** the global force vector.

$$\boldsymbol{K}.\boldsymbol{u} = \boldsymbol{F} \tag{4.32}$$

4.4. Elasto-plastic analysis

The elasto-plastic analysis is required in a structural problem in which the stress in the structure exceeds the material yield stress. In an elasto-static analysis, after unloading, the material regains its initial (un-deformed) configuration. However, when the yield stress is exceeded, unloading may leave

permanent plastic deformations due to plastic effects. So, the problem will be non-linear. In order to exhibit an elasto-plastic model, the stress-strain relation is shown in figure 4.2. As it is shown in this figure, when the yield stress is reached (point A_0), the material shows a plastic behavior and prior to reach that point the relation between stress and strain gives elasticity modulus. However, after passing the yield stress, the relation between stress and strain gives a tangent modulus.

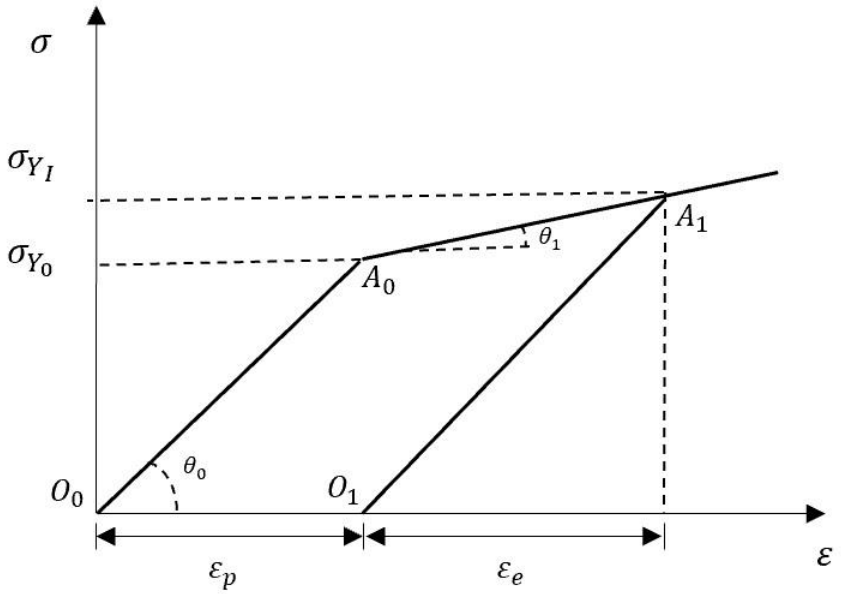

Figure 4. 2. Bilinear elasto-plastic model

To present a description of elasto-plastic behavior for a material, three requirements must be satisfied. First of all, **Yield Criterion,** which defines the limit elastic behavior. The second, **Flow Rule**, which defines the stress and deformation relation in the increments in a plastic regime. Finally, the **Hardening Rule**, which defines the changes in the yield function during the plastic deformation.

To define the total strain vector, elastic and plastic strain should be sum up, which is the so-called ***additive decomposition*** of the strain vectors, see the equation 4.33. In the following equation, ε^e represents the elastic strain. On the other hand, ε^p shows the plastic strain. As a matter of fact, according to the figure 4.2, the material after passing the yield stress, if the force is removed, for instance in point A_1, the material recovers the elastic part. However, keeps the plastic deformation which is dependent to the load history.

$$\varepsilon = \varepsilon^p + \varepsilon^e \tag{4.33}$$

Until the yield stress, Hooke's law (as a linear equation) is satisfied, but after the yield point, the relation between stress and strain becomes nonlinear. Thus, Hooke's law is not valid anymore. That's where the flow rule becomes necessary to determine the governing stress state in the problem. A hardening rule is also needed because of the yield surface evolve. Following sections will focus on each of the mentioned requirements.

4.4.1 Yield Criterion

The yield criterion detaches the plastic behavior from elastic behavior. As it is depicted in figure 4.3, yield surface with the function of $f(\boldsymbol{\sigma}, \boldsymbol{\varepsilon^p}, \kappa)$ determines two areas as elastic and plastic behavior which are shown in this figure as A and B, respectively. In this work, the materials are considered as homogenous and isotropic.

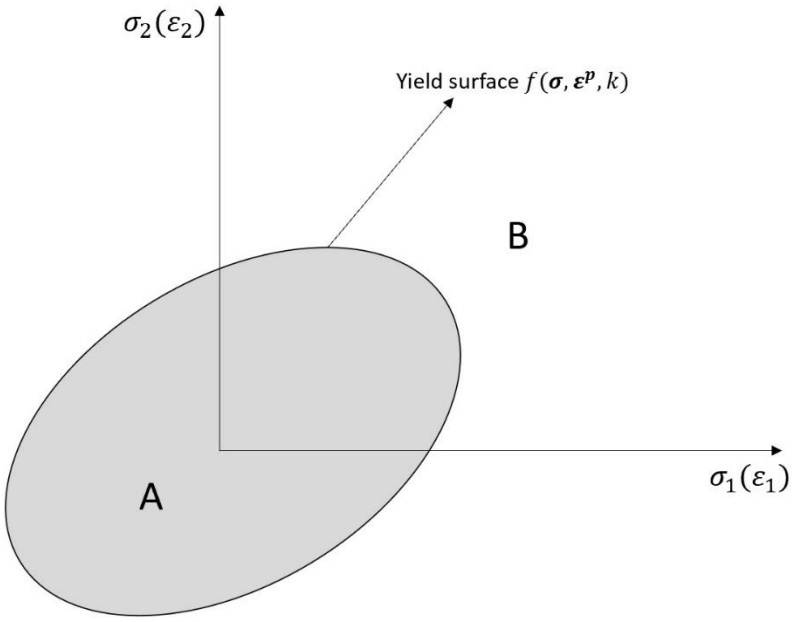

Figure 4. 3. Representation of the Yield surface

When the stress reaches to yield stress, the yield occurs. The yield surface is usually represented by equation 4.34.

$$F(\boldsymbol{\sigma}, \boldsymbol{\varepsilon^p}, \kappa) = f(\boldsymbol{\sigma}, \boldsymbol{\varepsilon^p}, \kappa) - \sigma_Y(\kappa) = 0 \tag{4.34}$$

Where the $f(\boldsymbol{\sigma}, \boldsymbol{\varepsilon^p}, \kappa)$ depends of the stress state $\boldsymbol{\sigma}$, the plastic strain $\boldsymbol{\varepsilon^p}$ and hardening parameter κ. Furthermore, the yield stress is shown by $\sigma_Y(\kappa)$ which is dependent of the hardening parameter. Since in this work, the materials are considered as homogenous and isotropic, the mentioned yield function will be independent from the hardening parameter. In this way, the equation 4.34 would be simplified as equation 4.35.

$$F(\boldsymbol{\sigma}) = f(\boldsymbol{\sigma}) - \sigma_Y = 0 \tag{4.35}$$

Two commonly used yield criteria are Tresca and von Mises. For a 2D domain, the yield surfaces are shown in figure 4.4, where the discontinuity is obvious for the Tresca yield criterion, which makes the computational implementation more difficulty [135].

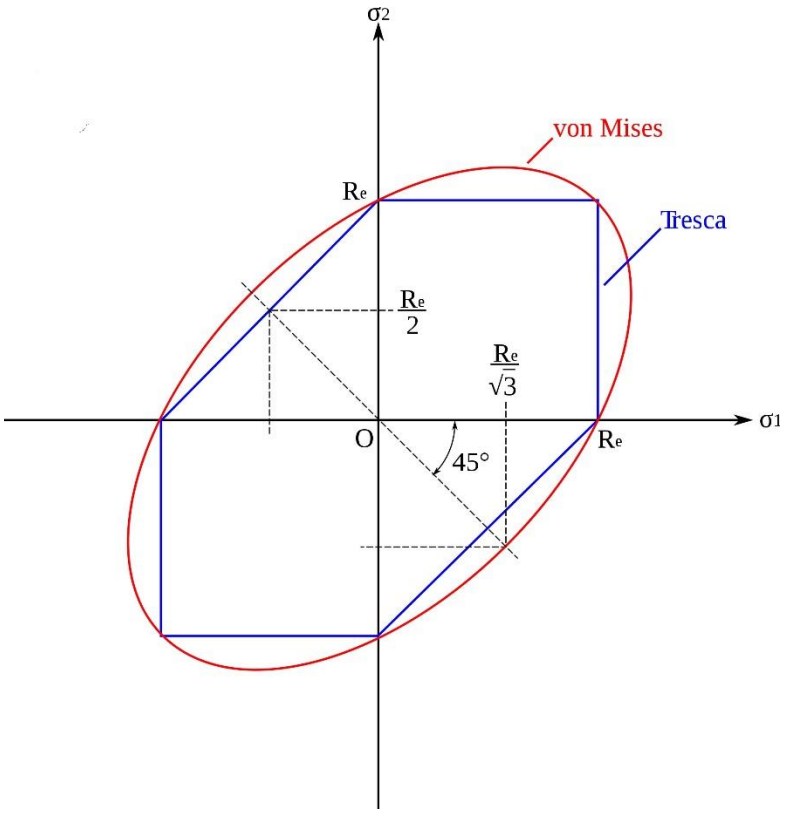

Figure 4. 4. Comparison of the Tresca (in blue) and von Mises (in red) yield surfaces

The materials in this work are ductile and due to their mechanical properties, the von Mises yield criterion has been selected. The von Mises yield criterion is independent of the first stress invariant, which allows to use this criterion in an analysis of plastic deformation for ductile materials such as the dental restorative composites (as the ones used in this work). On the other hand, when the second stress invariant reaches a certain value, yielding occurs. In equation 4.36, the second stress invariant is shown as the assumption.

$$I_2 = \left(\frac{\sigma_Y}{\sqrt{3}}\right)^2 \tag{4.36}$$

It is important to mention that the von Mises yield criterion can also be represented in the form of equation 4.37, which is the so-called effective stress. This term is used to show the results in this work.

$$\bar{\sigma}^2 = {\sigma_Y}^2 = 3I_2 \tag{4.37}$$

By extending the second stress invariant regarding the stress tensor components, the above equation can be expressed as follow in equation 4.38.

$$\bar{\sigma} = \sqrt{\frac{1}{2}\left[\left(\sigma_{xx} - \sigma_{yy}\right)^2 + \left(\sigma_{yy} - \sigma_{zz}\right)^2 + (\sigma_{zz} - \sigma_{xx})^2 + 6\left({\sigma_{yz}}^2 + {\sigma_{zx}}^2 + {\sigma_{xy}}^2\right)\right]} \tag{4.38}$$

$$F(\boldsymbol{\sigma}) = \sqrt{\frac{1}{2}\left[\left(\sigma_{xx} - \sigma_{yy}\right)^2 + \left(\sigma_{yy} - \sigma_{zz}\right)^2 + (\sigma_{zz} - \sigma_{xx})^2 + 6\left({\sigma_{yz}}^2 + {\sigma_{zx}}^2 + {\sigma_{xy}}^2\right)\right]} - \sigma_Y(\kappa) = 0 \tag{4.39}$$

4.4.2 Plastic flow

The material will experience the transition from elasticity to plastic behavior when the function mentioned above $f(\boldsymbol{\sigma})$ (stated in equation 4.35) reaches to the critical value equal to the yield stress of

that material. Nevertheless, the material behavior in the plastic zone will be dependent on the value of the variation of the yield function $f(\boldsymbol{\sigma})$, as it is indicated in equation 4.40.

$$df = \left(\frac{\partial f}{\partial \boldsymbol{\sigma}}\right)^T d\boldsymbol{\sigma} \tag{4.40}$$

In equation 4.40, $\frac{\partial f}{\partial \boldsymbol{\sigma}}$ is a normal vector to the yield surface and dependent of $\boldsymbol{\sigma}$, as represented in figure 4.5. It is known as the plastic flow vector.

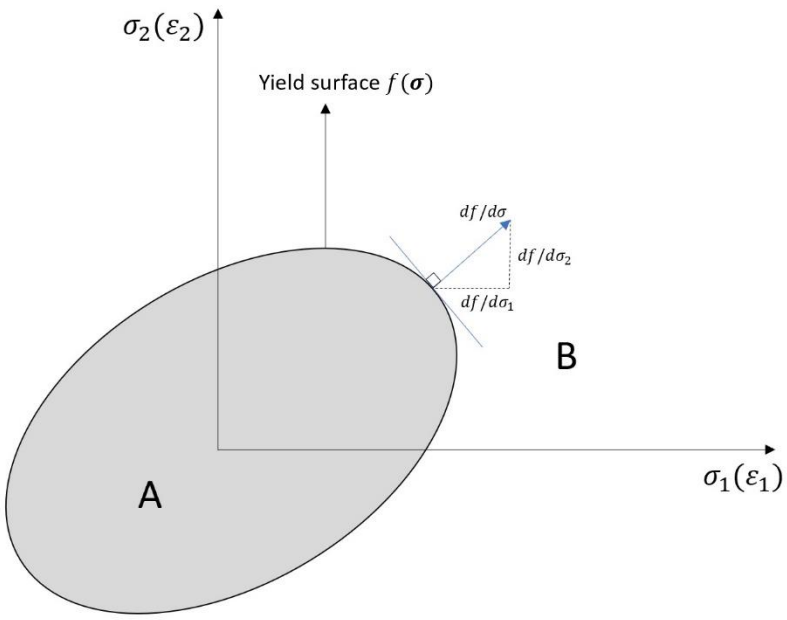

Figure 4. 5. Flow rule for an isotropic material (orthogonality principle)

The Prandtl-Reuss flow rule being applied to the yield function produces equation 4.41.

$$d\boldsymbol{\varepsilon^p} = d\lambda \frac{\partial f}{\partial \boldsymbol{\sigma}} \tag{4.41}$$

The $d\lambda$ in equation 4.41, is the plastic strain-rate multiplier and referring to figure 4.5, the conditions can be drawn according to the value of $d\lambda$ as follow. If $d\lambda < 0$, the Hook's law is valid and after unloading the material will return back to its initial state. If $d\lambda = 0$, stress value is critical, being on the yield

surface. For an isotropic material, material hardening is neglected which means that the model is a perfectly plastic model. If $d\lambda > 0$, the stress will remain on the yield surface. This case is when the hardening is considered for the material.

4.4.3 Hardening Rule

In a plastic deformation, the yield surface changes. The hardening rule is a description of the prior-mentioned phenomenon. Hardening causes changes in size and/or position of elastic zone except for an elastic-perfectly model. Isotropic Hardening, Kinematic Hardening, or Independent Hardening is the rules would help to determine how the yield function changes along the plastic flow, see figure 4.6.

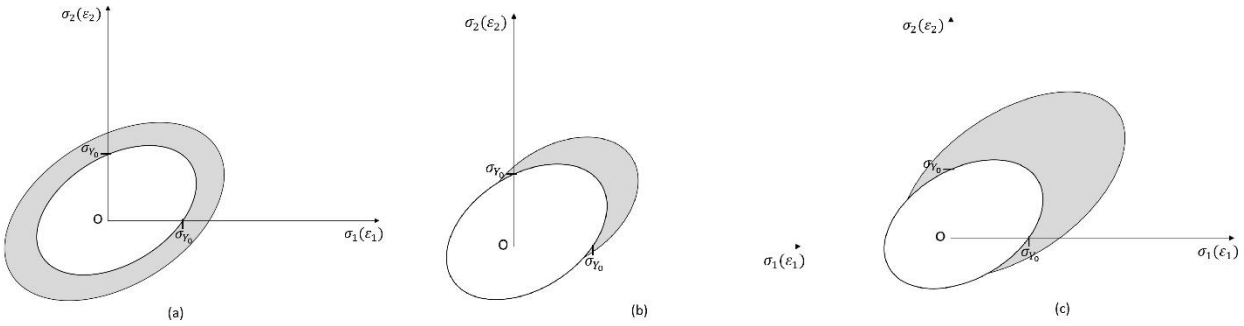

Figure 4. 6. Hardening rule: (a) Isotropic Hardening (b) Kinematic Hardening (c) Independent Hardening

The Isotropic Hardening Rule (Figure 4.6 (a)) has the assumption of initial surface expansion for the evolution of the yield surface along the plastic flow. This rule considers that the yield function has the same effect on tension and compression.

The Kinematic Hardening Rule represented in Figure 4.6 (b), shows the evolution of the yield surface as a translation of the surface, maintaining the initial size. This rule considers the Bauschinger effect.

Finally, the Independent Hardening Rule, shown in Figure 4.6 (c), presents the evolution to have translation, expansion, and/or rotation. In this case, the material is supposed to harden differently in tension and compression.

4.4.4 Nonlinear solution algorithms

A set of nonlinear equations are needed for an elastoplastic analysis of structures. There are generally two types of numerical algorithms to obtain the solutions, the incremental method, and the Newton-Raphson's method which is also known as an incremental and iterative method. The first one is simple, and usually, errors are high due to being simplified to some linear equations. The latter one, however, for each increment, there is an iteration process which reduces the error.

To reduce the computational costs, KT0 and KT1 (well-known modified versions of Newton-Raphson) were developed. For KT0 algorithm, initial data must be introduced in the first step. This data would be problem dimensions and discretization information, material properties, maximum load, essential boundary conditions and the number of increments and iterations of the algorithm. The maximum number of increments in this work was 10 increments.

With this information, the nodal mesh is constructed, along with the integration mesh. The influence domains are defined and the interpolation functions are calculated. With the material properties and the nodal connectivity, the initial stiffness matrix can be determined. With the natural and essential boundary conditions, the final stiffness matrix $\mathbf{K_0}$ is obtained. After this pre-processing phase, the KT0 algorithm can start.

The incremental load $\boldsymbol{f}_i$ is defined as in equation 4.42.

$$\boldsymbol{f}_i = \frac{\boldsymbol{F}}{inc} \tag{4.42}$$

Where $\boldsymbol{F}$ is the maximum load and inc is the number of increments. The displacement field can be obtained by equation 4.43.

$$\boldsymbol{u}_i = \boldsymbol{K}_0{}^{-1}\boldsymbol{f}_i \tag{4.43}$$

And consequently, the stress field will be as in equation 4.44.

$$\boldsymbol{\sigma}_i = \boldsymbol{cBu}_i \tag{4.44}$$

The stress state is verified for every Gauss point. If the stress passes the yield surface, the return algorithm is applied. In the end of this process, the actualized stress vector of the increment, see equation 4.45.

$$\boldsymbol{\sigma}_i = \boldsymbol{\sigma}_{i-1} + \Delta\boldsymbol{\sigma} \tag{4.45}$$

Chapter 5

Numerical Methods

Numerical methods used in this work are the Finite Element Method (FEM) and Meshless Methods. To have a general idea about these methods, Figure 5.1a demonstrates a physical domain of a half-brain, Figure 5.1b, and 5.1c give an example related to a half-brain, discretized by FEM and Meshless Method, respectively.

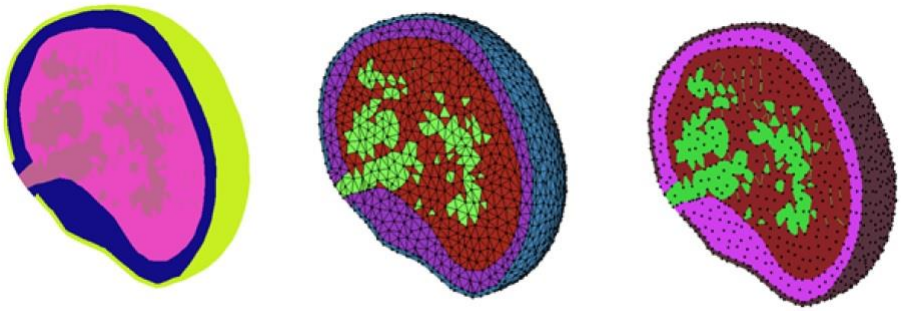

Figure 5. 1- (a) Physical domain of a half-brain. (b) Element mesh. (c) Nodal discretization.[136]

5.1 Finite Element Method

As it is mentioned above, the need for an approximation method for a continuum problem with a complex geometry led to the development of a discretization numerical technique known as FEM.

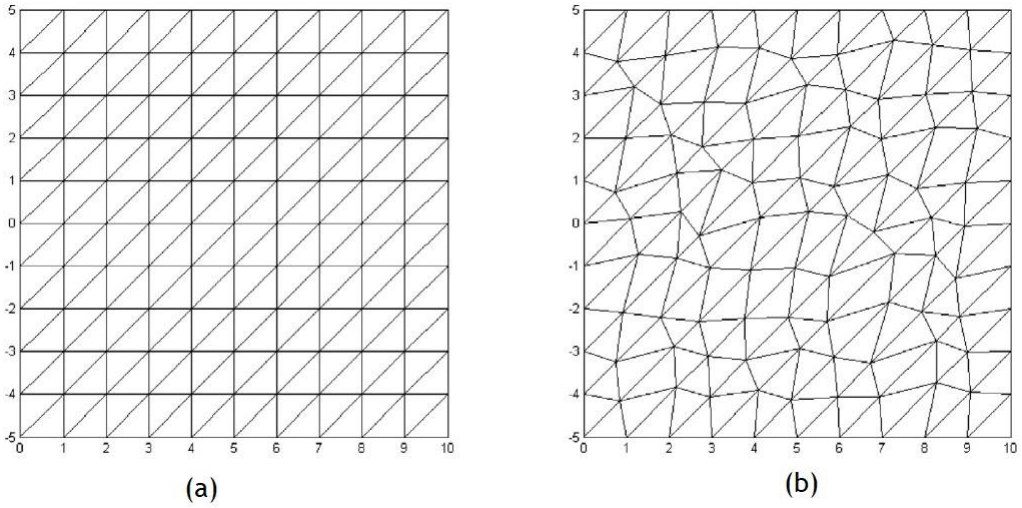

Figure 5. 2- (a) 2D regular mesh. (b) 2D irregular mesh.[137]

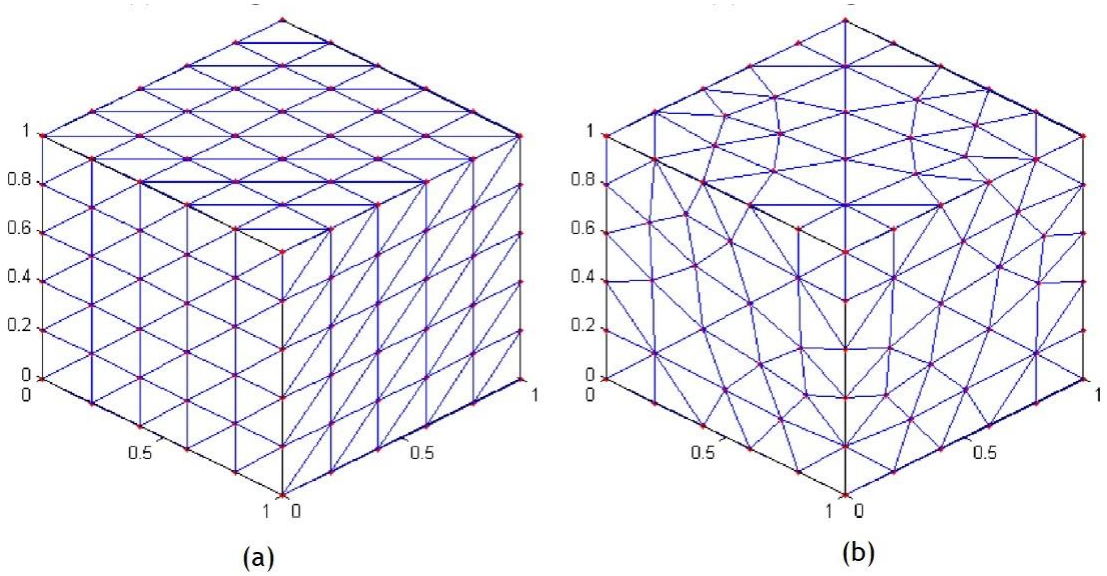

Figure 5. 3- (a) 3D regular mesh. (b) 3D irregular mesh.[137]

Although there are many numerical integration techniques, Gauss quadrature is one of the most efficient techniques for functions that are polynomials or nearly polynomials. In FEM, the integrals usually involve polynomials, so Gauss quadrature is a natural choice [134]. Finite element method has been used most often, however, besides its pros, there are some cons like the lack of accuracy due to large distortion of the elements in large displacements, or the re-meshing difficulties, reducing its overall

efficiency. Although using Lagrangian elements would be useful in large-displacements [138], FEM is still under-developed in comparison to meshless methods.

5.2 Meshless Methods

This work uses two meshless methods - the Radial Point Interpolation Method (RPIM), and the Natural Neighbor Radial Point Interpolation Method (NNRPIM). Meshless methods allows to reduce the time spent in the mesh generation phase. This fact has encouraged many authors in the last 20 years to use these methods. Furthermore, researchers would like to set a condition independent of mesh quality [137].

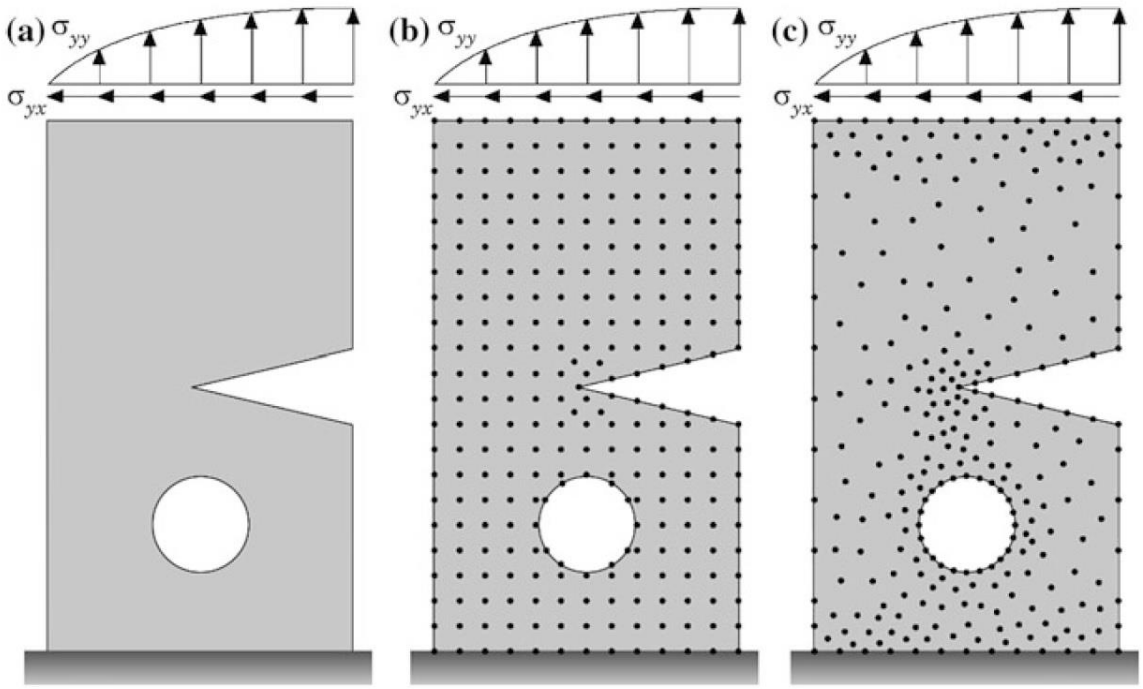

Figure 5. 4- a. Solid domain. b. Regular nodal discretization. c. Irregular nodal discretization [128].

In both meshless methods and element dependent methods, the nodal density of the discretization, as well as the nodal distribution (to be either regular or irregular) can affect the accuracy of the performance. Increasing the number of nodes, usually, can lead to a better result [128]. On the other hand, one of the main factors affecting the acceptance of a numerical technique is computational cost. Usually, the cost is measured for a prescribed accuracy for a problem [139]. So, by taking into account that more nodes would increase the computational cost, it is necessary to optimize the cost meticulously

without a negative effect on accuracy. Furthermore, it is usually recommended to set a high nodal density close to the locations in which are expected stress concentration, such as crack tips, convex, natural, and essential boundaries, domain discontinuities, etc. [140].

5.2.1 Generic Procedure of meshless methods

The first step is to define the geometry of the problem due to the need of establishment a solid domain and its surface. Then, the natural and the essential boundary conditions should be applied, see Figure 5.1a. Discretization of the domain with a nodal set can be either regular or irregular, as shown in Figure 5.1b and the Figure 5.1c, respectively. The only information required to construct an approximation or an interpolation function is the nodal spatial location, because contrary to the FEM, the distribution of nodes do not form a mesh [128].

5.2.2 Nodal connectivity

5.2.2.1 RPIM

In the FEM, the nodal connectivity is applied to the pre-processing phase by the establishment of predefined finite element mesh. On the other hand, in meshless methods, because of non-existence of a predefined connectivity mesh, it is needed to build one [141]. So, in the meshless methods, in general, after nodal discretization, the nodal connectivity is imposed with the “influence-domain” geometric construction [142]. By the overlap of the influence-domain of each node, the nodal connectivity in RPIM can be obtained [143]. Many of the meshless methods [144], [145], [146] employ fixed size influence-domain. However, RPIM uses a fixed number of nodes inside influence-domains with flexible size. Previous works suggest that each influence-domain should have between n = [9,16] nodes [146], [144], but Behzad V. Farahani et al. in a recent work, recommended that each 2D influence-domain should possess 20 nodes [147].

Figure 5.5a presents an example of rectangular fixed size influence-domain, and Figure 5.5b shows a circular shaped fixed size influence-domain. One of the cons of fixed size influence-domain is the virtual impossibility to fix a constant number of nodes inside each influence domain. Fixed and regular shaped influence-domains can decrease the accuracy of the numerical analysis [128]. Therefore, to avoid the loss of accuracy, it’s better to use the flexible size of influence-domain. Then, it’ll be easier to consider the same number of nodes inside the influence-domains, see Figure 5.5c.

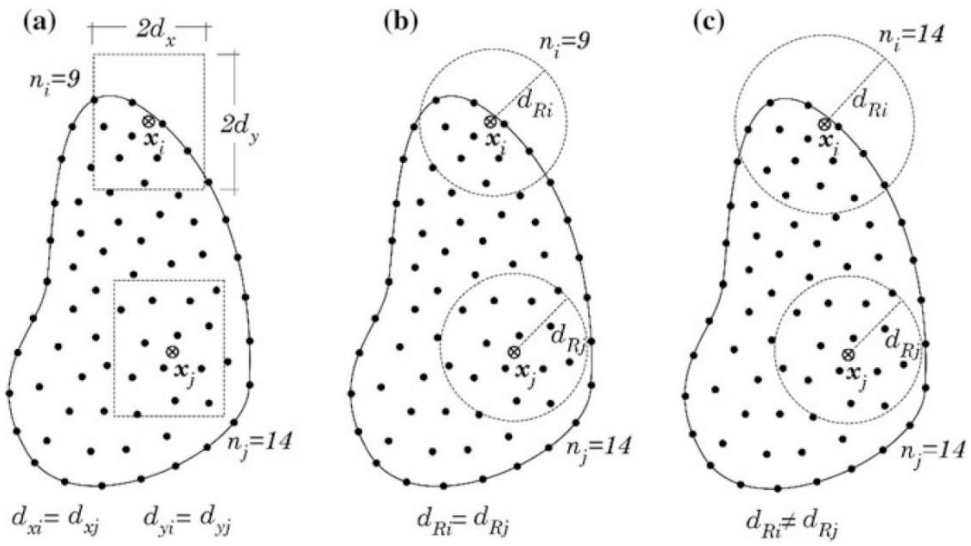

Figure 5. 5-(a) Fixed rectangular shaped influence-domain. (b) Fixed circular shaped influence-domain. (c) Flexible circular shaped influence-domain. [128]

5.2.2.2 NNRPIM

Sibson in 1981 [148], introduced the natural neighbor concept to obtain the Voronoi diagram. The NNRPIM combines the radial point interpolators with the natural neighbor mathematical concept [142]. Definition of a Voronoi cell could be consideration of a domain $\Omega \subset \mathbb{R}^d$, with a boundary of $\Gamma \in \Omega$, discretized in several nodes $N = \{n_0, n_1, \dots, n_N\} \in \mathbb{R}^d$ with coordinates: $X = \{\boldsymbol{x}_0, \boldsymbol{x}_1, \dots, \boldsymbol{x}_N\}$ with $\boldsymbol{x}_i \in \mathbb{R}^d$:

$$V_i \coloneqq \left\{\boldsymbol{x}_I \in \Omega \subset \mathbb{R}^d : \| \boldsymbol{x}_I - \boldsymbol{x}_i \| < \| \boldsymbol{x}_J - \boldsymbol{x}_j \|, \quad \forall i \neq j \right\} \tag{5.1}$$

The Voronoi cell V_i is where all the interior nodes are closer to n_i than the other nodes [142]. Since it is easier to visualize a 2D domain, d can be considered 2. Gathering the Voronoi cells together, makes the Voronoi diagram, 5.6a-f, [128].

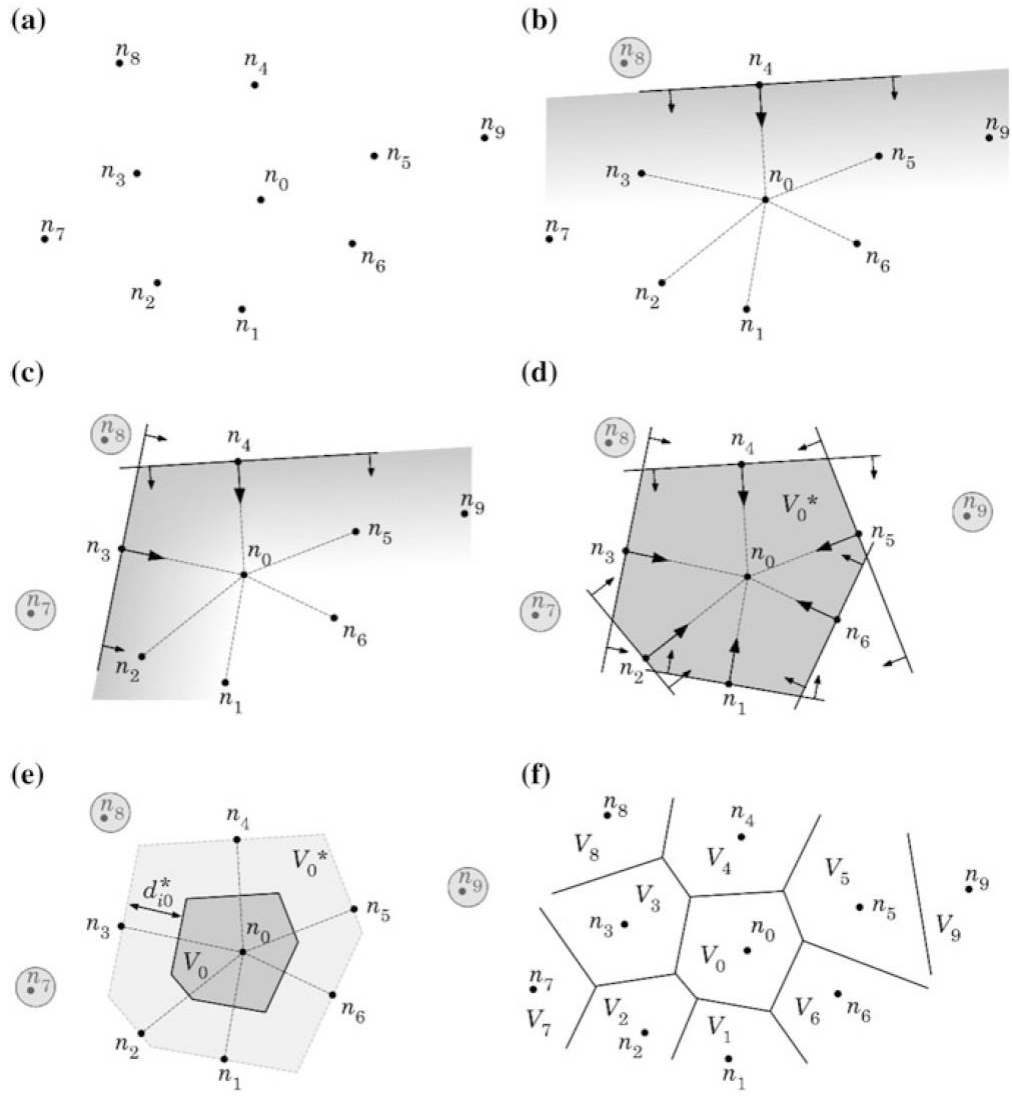

Figure 5. 6- (a) initial nodal set of potential neighbor nodes of the node n_0. (b) First trial plane. (c) Second trial plane. (d) Final trial cell containing just the natural neighbors of node n_0. (e) Node n_0 Voronoi cell V_0. (f) Voronoi diagram [128]

5.2.3 Numerical integration

5.2.3.1 RPIM

As it is demonstrated in Figure 5.7, based on Gauss-Legendre integration schemes, meshless RPI is capable to construct the back ground integration mesh to perform its numerical integration [144]. In the previous works, some nodal integration techniques have been proposed for integration of weak form methods [149] and [150] . Contrary to the basic integration scheme, Gauss-Legendre subdivides the sub-

cell again but only as quadrilaterals. After the centre of the geometric shape is determined, to obtain the integration points, and after the new sub-quadrilaterals are defined, it is possible to apply the Gauss-Legendre quadrature [151]. The bilinear quadrilateral which is the simplest member of the quadrilateral family is defined as follow. Isoparametric interpolation functions, N_i, as it is presented in the following equation 5.2, would help to obtain the Cartesian coordinates of the quadrature points [152].

$$\begin{cases} N_1(\xi,\eta) = \frac{1}{4}(1-\xi)(1-\eta) \\ N_2(\xi,\eta) = \frac{1}{4}(1-\xi)(1+\eta) \\ N_3(\xi,\eta) = \frac{1}{4}(1+\xi)(1+\eta) \\ N_4(\xi,\eta) = \frac{1}{4}(1+\xi)(1-\eta) \end{cases} \tag{5.2}$$

Then, the Cartesian coordinates are given by

$$\begin{aligned} x &= \sum_{i=1}^{m} N_i(\xi,\eta)\cdot x_i \\ y &= \sum_{i=1}^{m} N_i(\xi,\eta)\cdot y_i \end{aligned} \tag{5.3}$$

In equation 6.3, m is the number of the nodes inside the grid-cell and x_i and y_i are the natural coordinates of the cells' nodes.

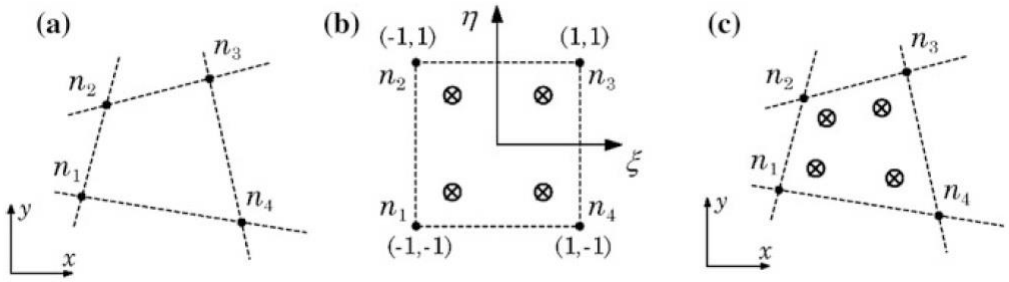

Figure 5. 7. (a) Initial quadrilateral from the grid-cell (b) Transformation of the initial quadrilateral into an isoparametric square shape and application of the 2X2 quadrature point rule. (c) Return to the initial quadrilateral shape [126]

Figure 5.8 presents the triangular and the quadrilateral sub-cells. By considering the area for the triangular shape and also quadrilateral shape, which the equation 5.4 and 5.5 present respectively, the integration weight of each integration point x_I is obtained using the equation 5.6 [128]. A_I^T shows the area of a triangular shape and also A_I^Q shows the area of a quadrilateral shape.

$$A_I^T = \frac{1}{2}\left|\det\begin{bmatrix} x_2 - x_1 & y_2 - y_1 \\ x_3 - x_1 & y_3 - y_1 \end{bmatrix}\right| \tag{5.4}$$

$$A_I^Q = \frac{1}{2}\left|\det\begin{bmatrix} x_2 - x_1 & y_2 - y_1 \\ x_3 - x_1 & y_3 - y_1 \end{bmatrix} + \det\begin{bmatrix} x_4 - x_1 & y_4 - y_1 \\ x_3 - x_1 & y_3 - y_1 \end{bmatrix}\right| \tag{5.5}$$

$$\widehat{w_I} = w_\eta w_\xi \left(\frac{A_I^Q}{4}\right) \tag{5.6}$$

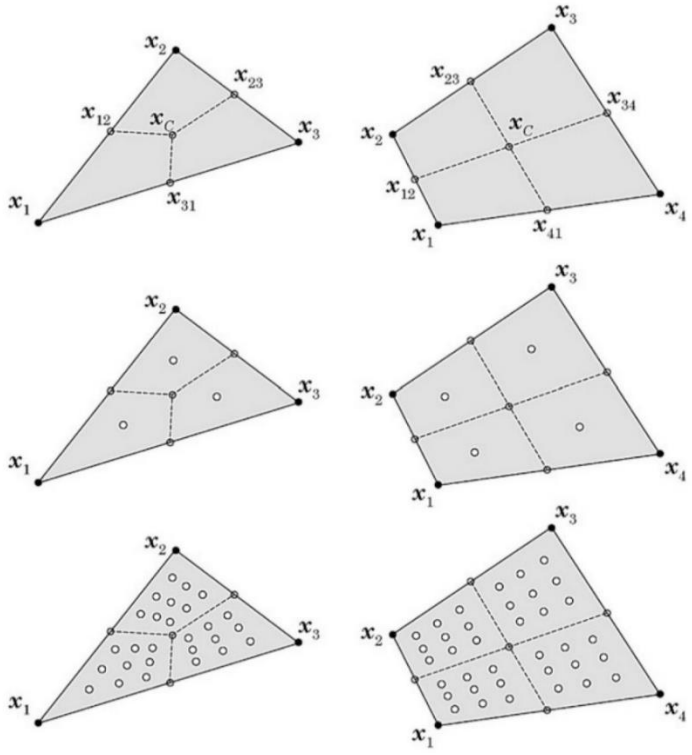

Figure 5. 8- Triangular and quadrilateral shape and the respective integration points using the Gauss-Legendre integration scheme [128]

Liu et al. in 2007, have developed a nodal integration technique as a stable technique for meshless weak form methods, which is implemented in the integration process of NNRPIM [153]. For the mentioned purpose, they have used Taylor's expansion to get rid of instability which is common in nodal integration

methods. Using Taylor's expansion is recognizable in some FEM studies [154] and also meshfree studies [155],[156], and [150]. However, in Nagashima's work, the formulation base is EFG method that uses MLS shape functions, and Taylor's first-order expansion is applied to the strain matrix in order to achieve a stabilization [155]. On the other hand, Liu has used RPIM formulation, and Taylor's expansion is applied entirely to B^TDB and is expanded up to second-order [153].

Figure 5.8 shows a schematic illustration of a 13-node influence-domain as another example of RPIM integration.

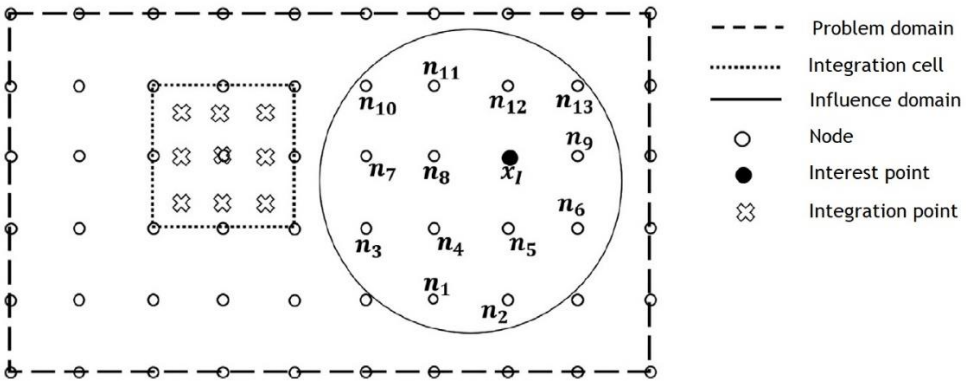

Figure 5. 9- A RPIM problem domain and its influence domain about the interest point and an integration cell with 3×3 integration points in the discrete model illustration.[157]

5.2.3.2 NNRPIM

NNRPIM can use the previously described integration scheme, or it can use a form of nodal integration, which is as simple as considering the integration point, x_I, as the center of each Voronoi cell in the Voronoi diagram. In NNRPIM, an integration mesh is necessary to integration the integro-differential equations of the Galerkin weak form. This integration mesh uses directly nodal distribution, which is so called Voronoi diagram, as previously was mentioned [158]. Alternatively, the NNRPIM can construct the integration background integration mesh as figure 5.10 indicates. This will lead to a background integration mesh completely dependent on the nodal distribution [128].

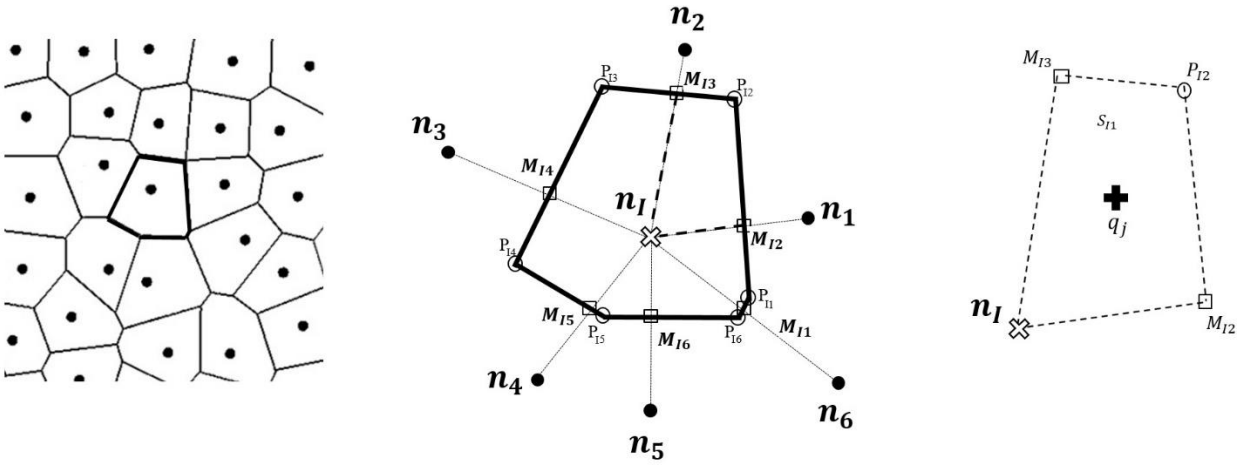

Figure 5. 10. - (a) Voronoi cell and the respective P_Ii intersection points. (b) Middle points M_Ii and the respectively generated quadrilaterals. (c) Quadrilateral n_I M_12 P_12 M_13.

As it is demonstrated in Figure 5.9 and 5.10, construction of sub-cells generates two basic shapes of triangles or quadrilaterals, respectively. In equation 5.7, A can refer to length in a 1D domain. Also, it would refer to the area in a 2D problem and volume, for a 3D problem. Furthermore, to present a sub-cell, S_{Ii} is used. Thus, utilizing equation 5.7, gives the size of the Voronoi cell of an interested point.

$$A_{V_I} = \sum_{i=1}^{n} A_{S_{Ii}}, \quad \forall A_{S_{Ii}} \geq 0 \tag{5.7}$$

By holding the size of the Voronoi cell, the spatial location of each integration point could be obtained by equation 5.8.

$$\boldsymbol{x}_I = \frac{\sum_{i=1}^{n} \boldsymbol{x}_{S_i} A_{S_{Ii}}}{\sum_{i=1}^{n} A_{S_{Ii}}} \tag{5.8}$$

Being $\boldsymbol{x}_{S_i}$ the barycenter of the sub-cell S_{Ii} and $A_{S_{Ii}}$ is the size of the sub-cell S_{Ii}.

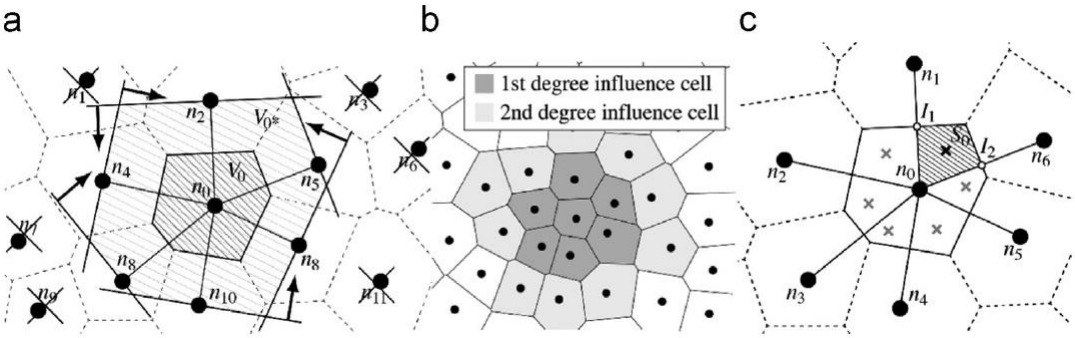

Figure 5. 11- (a) generation of Voronoi diagram. (b) types of influence cells used. (c) generation of integration mesh.[159]

5.2.4 Interpolating shape functions

Both of the RPIM and NNRPIM possess Kronecker delta property. This is one of the pros of these methods because, in some meshless methods (such as the MLS - Moving Least Square), which do not have this property, the imposition of the essential boundary conditions is not that easy. However, in RPIM and NNRPIM, owing to this property, it's possible to apply the essential boundary conditions directly to the stiffness matrix. Considering the main domain $\Omega \subset \mathbb{R}^d$ and the function space *T* on the mentioned domain and the finite dimensional space $T_H \subset T$ which discretizes the domain Ω that is indicated as in 5.9,

$$T_H := \langle r(\boldsymbol{x}_i - \boldsymbol{x}) : i \in \mathbb{N} \wedge i \leq N \rangle + p_k(\boldsymbol{x}) \tag{5.9}$$

For an interest point $\boldsymbol{x_I} \in \mathbb{R}^d$, interpolation function of $u(\boldsymbol{x_I})$ can be as follow in equation 5.10,

$$u(\boldsymbol{x_I}) = \sum_{i=1}^{n} R_i(\boldsymbol{x_I}) a_i(\boldsymbol{x_I}) + \sum_{j=1}^{m} P_j(\boldsymbol{x_I}) b_j(\boldsymbol{x_I}) = \boldsymbol{R}^T(\boldsymbol{x_I})\boldsymbol{a}(\boldsymbol{x_I}) + \boldsymbol{p}^T(\boldsymbol{x_I})\boldsymbol{b}(\boldsymbol{x_I}) \tag{5.10}$$

where n is the number of nodes inside the influence-domain of interest point $\boldsymbol{x_I}$ and $R_i(\boldsymbol{x_I})$ is the radial basis function (RBF), see equation 5.11. On the other hand, the number of monomials of the complete polynomial basis P_j, is *m*, which can be expressed in equation 5.12 by using the triangle of Pascal. Also, $a_i(\boldsymbol{x_I})$ and $b_j(\boldsymbol{x_I})$ are non-constant coefficients for $\boldsymbol{R}(\boldsymbol{x_I})$ and $\boldsymbol{p}(\boldsymbol{x_I})$, respectively, defined as equations 5.13 and 5.14,

$$\boldsymbol{R}(\boldsymbol{x_I}) = \{\, R_1(\boldsymbol{x_I}) \quad R_2(\boldsymbol{x_I}) \quad \dots \quad R_n(\boldsymbol{x_I})\}^{\boldsymbol{T}} \tag{5.11}$$

$$\boldsymbol{p}(\boldsymbol{x_I}) = \{\, p_1(\boldsymbol{x_I}) \quad p_2(\boldsymbol{x_I}) \quad \dots \quad p_m(\boldsymbol{x_I})\}^{\boldsymbol{T}} \tag{5.12}$$

$$\boldsymbol{a}(\boldsymbol{x_I}) = \{\, a_1(\boldsymbol{x_I}) \quad a_2(\boldsymbol{x_I}) \quad \dots \quad a_n(\boldsymbol{x_I})\}^{\boldsymbol{T}} \tag{5.13}$$

$$\boldsymbol{b}(\boldsymbol{x_I}) = \{\, b_1(\boldsymbol{x_I}) \quad b_2(\boldsymbol{x_I}) \quad \dots \quad b_m(\boldsymbol{x_I})\}^{\boldsymbol{T}} \tag{5.14}$$

The number of m should be lower than the number of nodes inside the influence-domain to obtain stable functions. The Euclidean norm between the interest point and the field nodes is d_{iI} which for a 2D domain, can be written as equation 5.15.

$$d_{iI} = \sqrt{(x_i - x_I)^2 + (y_i - y_I)^2} \tag{5.15}$$

In this work, the multi-quadrics function was selected to be used in the following formulation 5.16.

$$R(r_{Ii}) = \left({d_{Ii}}^2 + c^2\right)^p \tag{5.16}$$

where c and p are shape parameters requiring optimization, and by the works of Wang [160], the optimum value for these parameters are c=1.42 and p=1.03, and in this work, they are chosen as mentioned by Wang for RPIM. Furthermore, for NNRPIM these parameters are considered as c=0.0001 and p=0.9999.

In this work, the model is 2D, and the polynomial bases are considered as in equation 5.17 so-called linear basis (m=3) for RPIM.

$$\boldsymbol{p}^T(\boldsymbol{x}) = \{1 \quad x \quad y\} \tag{5.17}$$

For NNRPIM analysis, constant basis (m=1) was chosen, see equation 5.18.

$$\boldsymbol{p}^T(\boldsymbol{x}) = \{1\} \tag{5.18}$$

The Radial Point Interpolation functions have some properties such as consistency, reproducibility, the partition of unity, compact support, compatibility, and Kronecker Delta. Kronecker delta is one of the most important properties of RPI methods reducing the computational costs in comparison to the methods using approximation methods. Interpolating shape functions pass through all the nodes inside the influence-domain which allows the direct boundary conditions imposition.

it is possible to obtain the following set of equations, written in matrix form:

$$\begin{bmatrix} \boldsymbol{R} & \boldsymbol{P} \\ \boldsymbol{P^T} & \boldsymbol{Z} \end{bmatrix} \begin{Bmatrix} \boldsymbol{a}(\boldsymbol{x_I}) \\ \boldsymbol{b}(\boldsymbol{x_I}) \end{Bmatrix} = \boldsymbol{M_T} \begin{Bmatrix} \boldsymbol{a}(\boldsymbol{x_I}) \\ \boldsymbol{b}(\boldsymbol{x_I}) \end{Bmatrix} = \begin{Bmatrix} \boldsymbol{u_s} \\ \boldsymbol{z} \end{Bmatrix} \tag{5.19}$$

Where $Z_{ij} = 0$ for $\{i, j\} = 1, 2, \dots, m$ and $z_i = 0$ for $i = 1, 2, \dots, m$. Thus, it is possible to obtain the non-constant coefficients $\boldsymbol{a}(\boldsymbol{x}_I)$ and $\boldsymbol{b}(\boldsymbol{x}_I)$:

$$\begin{Bmatrix} \boldsymbol{a}(\boldsymbol{x_I}) \\ \boldsymbol{b}(\boldsymbol{x_I}) \end{Bmatrix} = \boldsymbol{M_T^{-1}} \begin{Bmatrix} \boldsymbol{u_s} \\ \boldsymbol{z} \end{Bmatrix} \tag{5.20}$$

After some substitutions, it is possible to re-write Equation. (5.10) and obtain the following equation:

$$u^h(\boldsymbol{x_I}) = \{\boldsymbol{r}(\boldsymbol{x_I})^T \quad \boldsymbol{p}(\boldsymbol{x_I})^T\} \, \boldsymbol{M_T^{-1}} \begin{Bmatrix} \boldsymbol{u_s} \\ \boldsymbol{z} \end{Bmatrix} \tag{5.21}$$

Because the field variable value for an interest point $\boldsymbol{x}_I$ is interpolated using the shape function values obtained at the nodes inside the influence cell of the interest point, it is possible to identify the interpolation function vector $\varphi(\boldsymbol{x}_I)$, with size n:

$$\boldsymbol{u^h}(\boldsymbol{x_I}) = \{\boldsymbol{r}(\boldsymbol{x_I})^T \quad \boldsymbol{p}(\boldsymbol{x_I})^T\} \, \boldsymbol{M_T^{-1}} \begin{Bmatrix} \boldsymbol{u_s} \\ \boldsymbol{z} \end{Bmatrix} = \{\boldsymbol{\varphi}(\boldsymbol{x_I})^T \quad \boldsymbol{\psi}(\boldsymbol{x_I})^T\} \begin{Bmatrix} \boldsymbol{u_s} \\ \boldsymbol{z} \end{Bmatrix} \tag{5.22}$$

Where, $\boldsymbol{\psi(x_I)^T}$ is a by-product vector, that only exists if a polynomial basis is considered, otherwise it does not exist. Therefore, the RPI shape function can be defined as:

$$\boldsymbol{u^h(x_I) = \{r(x_I)^T \quad p(x_I)^T\} M_T^{-1} \begin{Bmatrix} u_s \\ z \end{Bmatrix} = \{\varphi(x_I)^T \quad \psi(x_I)^T\} \begin{Bmatrix} u_s \\ z \end{Bmatrix}} \qquad 5.23$$

Chapter 6

Numerical Applications

In this work, a 2D model as a molar tooth of a human has been proposed to be investigated under certain loading situations. Load cases simulating normal occlusal loads and paranormal loads, such as bruxism, are considered to be discussed and analysed. Furthermore, three dental composite materials are considered as restorative materials, and the comparison is made for three of them and the natural tooth.

6.1 Elastic Analysis

6.1.1 Model Description

The 2D model which is indicated in Figure 6.1, is a molar tooth of a human inserted into the mandibular bone (both cortical and trabecular tissue are represented). On the right side of the represented tooth there is another tooth (a molar, not represented in the figure), and on the left side there is a void, an absence of tooth. This case represents a real clinical case, in which the left tooth was removed to insert there an implant. Then, during the night, due to the absence of the left tooth and due to bruxism (the patient presents evident signs of bruxism), the central tooth (the one represented in the figure) has fractured. Thus, this study aims to understand the stress field of the central tooth due to normal occlusal loads and bruxism loads.

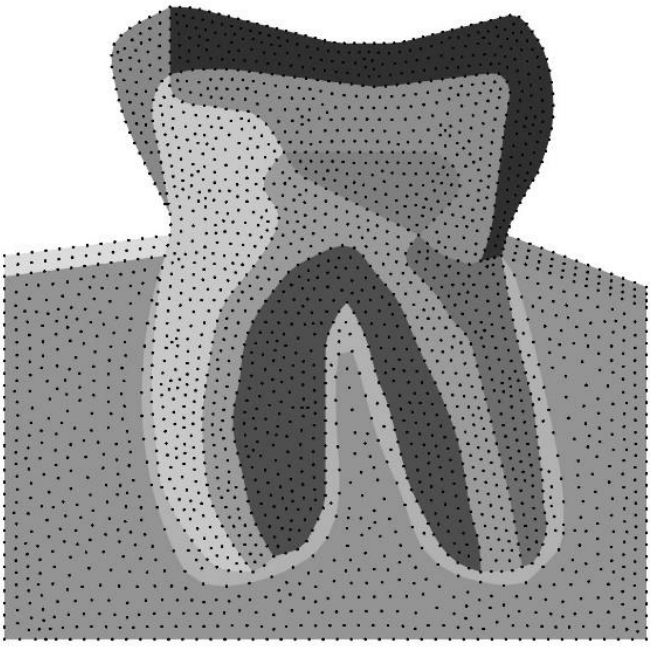

Figure 6. 1. 2D model of a molar tooth

The model is drawn and meshed in FEMAP© software (student version). Then, the model is exported as an "inp" file and imported to FEMAS (Finite Element and Meshless Analysis Software) developed by Dr. Belinha [161] (cmech.webs.com). This software is based on MATLAB®, possessing a graphical user interface (GUI) and it is capable of to perform analyses using the FEM and meshless methods. Several problems can be analysed using FEMAS, such as:

- Linear Elasto-static analysis
- Free vibration linear elastic analysis
- Buckling linear elastic analysis
- Elasto-plastic non-linear analysis
- Bine tissue remodeling analysis
- Fluid flow analysis (low velocities)
- Crack opening path (fracture mechanics)

The model has 4968 elements and 2467 nodes. Since the model possesses an irregular geometry, the triangular elements were selected to mesh the model. This kind of element allows to generate meshes capable of accommodating to highly irregular boundaries. This mesh is necessary to implement the finite element analysis. The triangular elements are useful for the RPIM, since they allow to construct the background integration mesh for the RPIM. Regarding the NNRPIM, the formulation only requires the nodal mesh of the model, the element mesh is discarded. All the boundary conditions and the material

properties are imposed in FEMAS. Besides, the dimensional approach of the numerical analysis is 2D plane strain.

The 2D model is constituted by 13 patches to manage the material properties easily and mesh homogeneously. Each color represents each patch, from which it gets their material properties, see Figure 6.2. Table 6.1 indicates the materials of each patch. The patches 1, 2, and 3 assume a tooth attribute when the normal tooth is considered for the analysis. Nevertheless, when the restored tooth is being analyzed, the mentioned patches get the material properties of three commercial restorative dental composites which are being investigated in this work.

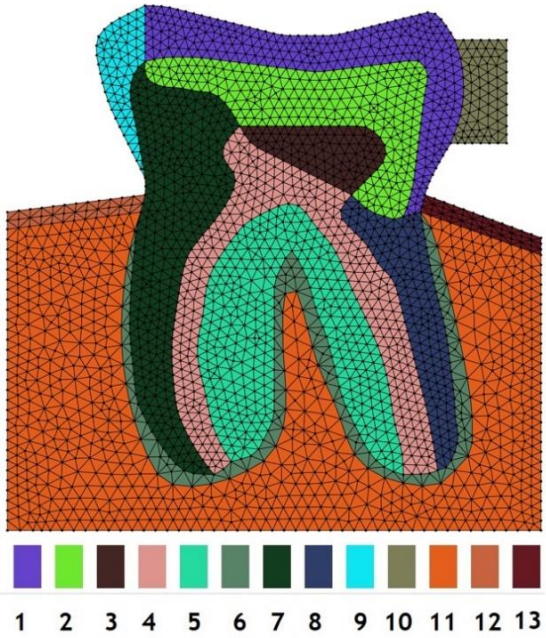

Figure 6. 2. The 2D model is combined with 13 patches

Patch 1	Patch 2	Patch 3	Patch 4	Patch 5	Patch 6	Patch 7
Enamel / composite	Dentine / composite	Pulp / composite	Pulp	Dentine	Periodontal Ligament	Dentine
Patch 8	Patch 9	Patch 10	Patch 11	Patch 12	Patch 13	
Dentine	Enamel	Fictitious Material	Trabecular Bone	Cortical Bone	Cortical Bone	

Table 6. 1. Patch legend for the 2D model

As it is mentioned previously, 4 load cases are imposed to this analysis as normal boundary conditions representing Bruxism load cases: ORV (Occlusal Right Vertical); OLV (Occlusal Left Vertical); BRV (Bruxism Right Vertical); BLV (Bruxism Left Vertical); and for the essential boundary conditions, the lower edge is fixed in Y direction, right and left edge of the bone is fixed in X direction. Nevertheless, in two particular load cases - BRV and ORV – in which the forces are orientation from left to right, the fictitious material gets involved in the problem and assumes the material properties of enamel and its boundary condition are fixed in the X direction. However, in load cases BLV and OLV there is no fictitious material, see Figure 6.3. It's important to mention that each force is divided by 5 and applied to 5 nodes which in overall gives the total force being assumed to impose.

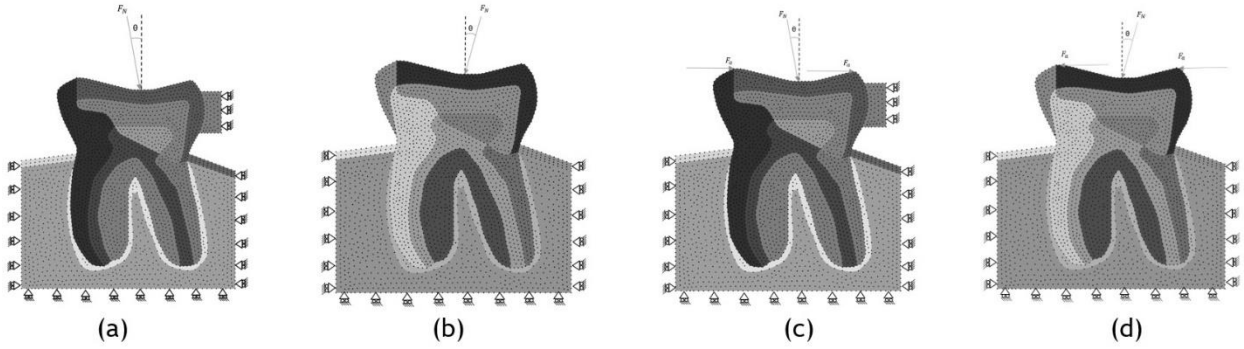

Figure 6. 3. 4 Bruxism load cases (a) ORV (b) OLV (c) BRV (d) BLV

Carey and his colleagues in 2007 determined a force range of 25N to 450N as an occlusal load to investigate the relationship between applied occlusal load and articulating paper mark area [162]. Furthermore, Vasudeva and Bogra used a force range of 100N to 500N in their finite element study on the effect of occlusal restoration and loading on the development of abfraction lesions [163]. Based on the literature, in this work, 225N and 405N are applied in load cases ORV, OLV, and BRV, BLV, respectively, see table 6.2. According to Figure 6.2, F_N has 225N imposed to the top edge of the tooth with an angle of 11 degrees apart from the vertical line. On the other hand, F_a is a horizontal force with a magnitude of 90N at each side which means totally in BRV and BLV load case, the magnitude of the horizontal load is 180N.

Load case	Force Magnitude (N)
ORV	225
OLV	225
BRV	405
BLV	405

Table 6. 2. Force magnitude for each load case

6.1.2 Results

The results are obtained for a normal tooth and restored the tooth with three different commercial materials including Z250™, Z100™, and Herculite XRV Ultra™ in von Mises effective stress. The results are shown for nine different points distributed in the 2D model as it is shown in figure 6.4.

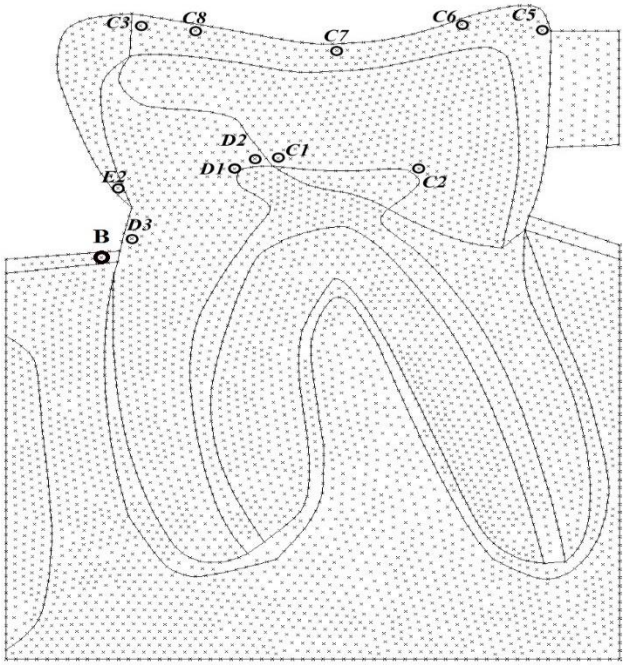

Figure 6. 4. Interest points for the results of the elastic analysis

The results in table 6.3 are for ORV load case, table 6.4 for OLV, table 6.4 for BRV, and table 6.5 for BLV load case.

For the load case ORV, the most critical point is D1 based on FEM results. However, there is a significant difference between the meshless results and FEM solution. Possibly, the difference could be explained by the curvature in that region, which complexify locally the geometry. Thus, finite element method would lose its accuracy in such location and meshless methods seem more reliable than FEM.

The remaining interest nodes in table 6.3, show low values and as a comparison between the materials, usually the results are close between each other. Although Z100™ in C5, C3, D2, is tolerating more stress, among the points, Integral (normal tooth) sometimes conveys more stress than the artificial materials. In contrast to the normal tooth, which does not have stable strength in different points, it is possible to make a rank for the composites as follow: Regarding higher von Mises effective stress, Z100™ > Z250™ > Herculite XRV Ultra™ except for E2, D1, and B.

Point	Method	Integral (MPa)	Z250 (MPa)	Z100 (MPa)	Herculite XRV Ultra (MPa)
C5	FEM	5.5952	7.43012	8.2087	6.5964
	RPIM	3.1879	5.1495	6.0377	4.2507
	NNRPIM	3.0583	4.8616	5.6786	4.0303
C3	FEM	3.0043	1.5492	1.5718	1.5326
	RPIM	2.9271	1.1701	1.2382	1.1129
	NNRPIM	2.7548	1.0847	1.1539	1.0267
C1	FEM	18.0439	20.3075	19.9072	20.7158
	RPIM	15.8312	19.5161	19.1893	22.877
	NNRPIM	16.0076	19.1120	18.7017	19.6347
C2	FEM	21.8503	13.9843	14.3727	13.5835
	RPIM	30.0217	14.1785	14.6037	13.7516
	NNRPIM	27.5532	12.228	12.5756	11.8722
D2	FEM	16.4741	20.34	20.5958	20.1866
	RPIM	23.9457	21.4297	22.4601	20.3266
	NNRPIM	26.7256	22.5997	23.684	21.4450
D3	FEM	14.8746	12.0566	12.4032	11.7164
	RPIM	16.7952	11.9556	12.4094	11.4415
	NNRPIM	15.5338	10.9617	11.4198	10.4253
E2	FEM	9.58194	11.7963	9.8119	14.0172
	RPIM	13.4354	14.5379	12.7529	16.4638
	NNRPIM	11.5316	12.5365	10.9973	14.2158
D1	FEM	45.4805	46.6307	44.845	48.0606
	RPIM	22.3672	20.1448	19.6552	20.5324
	NNRPIM	18.7050	16.6096	16.2573	16.8364
B	FEM	21.7572	19.1773	19.2216	18.8358
	RPIM	13.8255	11.3787	11.2742	11.2445

	NNRPIM	12.9580	10.7112	10.6182	10.5690

Table 6. 3. Effective stress for each interest point obtained by FEM and meshless methods for ORV load case

For the OLV load case, as well as ORV load case, the maximum value goes for D1 and there is still a significant difference between the meshless and finite element method solution. RPIM and NNRPIM often show close results.

Point	Method	Integral (MPa)	Z250 (MPa)	Z100 (MPa)	Herculite XRV Ultra (MPa)
C5	FEM	3.2316	1.1708	1.0558	1.2839
	RPIM	3.6085	1.3075	1.2011	1.4073
	NNRPIM	3.5353	1.2184	1.1287	1.3025
C3	FEM	3.0996	1.6256	1.6425	1.6137
	RPIM	3.1023	1.3092	1.3823	1.2437
	NNRPIM	2.9258	1.2034	1.2801	1.1353
C1	FEM	18.9798	21.7983	23.3290	22.4492
	RPIM	14.7185	22.1492	21.7127	22.8770
	NNRPIM	14.5064	21.7049	21.1701	22.5106
C2	FEM	21.6884	21.1461	12.5521	11.6889
	RPIM	27.8121	12.2385	12.6862	11.7462
	NNRPIM	24.9512	10.5006	10.8783	10.0753
D2	FEM	17.3721	22.5175	22.7049	22.5585
	RPIM	8.54979	8.9952	7.78260	10.4186
	NNRPIM	26.9725	26.6770	27.7546	25.6310
D3	FEM	20.3721	18.8777	19.2488	18.4803
	RPIM	24.1549	23.9154	24.2661	23.4855
	NNRPIM	22.5088	22.1515	22.4919	21.7279
E2	FEM	6.5531	6.4611	6.0973	7.2954
	RPIM	8.5497	8.9952	7.7826	10.4186
	NNRPIM	7.5632	7.7938	6.9172	8.8877
D1	FEM	46.1949	49.9664	47.7495	52.0633
	RPIM	23.8774	23.4906	22.7504	24.2522
	NNRPIM	20.0176	19.5382	18.9596	20.1017
B	FEM	25.9951	26.2203	25.7937	26.5950
	RPIM	16.1607	17.4401	16.9566	17.8891
	NNRPIM	15.1778	16.4417	15.9900	16.8561

Table 6. 4. Effective stress for each interest point obtained by FEM and meshless methods for OLV load case

The results for BRV load case, shown in table 6.5, indicate that the von Mises stress is increased for the points distributed on tooth and the composite material. Composites and integral tooth in E2 are under more stress than the previous load cases. On the other hand, composites in E2, based on results of meshless methods and finite element method, are experiencing more stress than the normal tooth with a significant difference in values.

Point	Method	Integral (MPa)	Z250 (MPa)	Z100 (MPa)	Herculite XRV Ultra (MPa)
C5	FEM	39.7102	37.9113	38.6150	37.0119
	RPIM	38.3552	37.1061	38.5027	35.5844
	NNRPIM	36.8642	34.7265	36.2392	33.0846
C3	FEM	25.3540	21.3811	22.1834	20.5036
	RPIM	29.9554	20.8321	22.5078	19.1341
	NNRPIM	27.0347	18.3408	19.9967	16.6424
C1	FEM	19.1716	21.4403	21.0295	21.6692
	RPIM	15.7509	18.5243	18.2419	18.8107
	NNRPIM	15.9590	18.1396	17.8301	18.4366
C2	FEM	19.4929	13.7986	14.0769	13.5317
	RPIM	32.7543	14.2363	14.4835	13.9903
	NNRPIM	30.0026	12.4467	12.6549	12.2514
D2	FEM	17.8141	20.9214	21.3380	20.5362
	RPIM	23.7431	19.6274	21.0298	18.0866
	NNRPIM	26.4761	20.8919	22.3942	19.2456
D3	FEM	18.1325	24.7435	22.3729	27.6387
	RPIM	18.3844	29.7177	26.3941	33.9760
	NNRPIM	16.8826	27.6732	24.5873	31.6365
E2	FEM	35.4201	49.1697	44.7463	54.2320
	RPIM	36.5170	49.9415	46.0833	54.3765
	NNRPIM	32.6821	45.3985	41.8638	49.4808
D1	FEM	54.5954	56.2522	55.3494	56.4029
	RPIM	23.5858	22.0611	21.9461	22.0130
	NNRPIM	19.5265	17.9892	17.9685	17.8555
B	FEM	21.1916	17.4999	18.4097	15.8918
	RPIM	12.6315	9.6560	10.3579	8.3808

	NNRPIM	11.8546	9.1480	9.83233	7.9058

Table 6. 5. Effective stress for each interest point obtained by FEM and meshless methods for BRV load case

The 2D model in this work under the BLV load case of bruxism, leads to more different results than the previous load cases, see table 6.6. The main reason could be the absence of tooth next to the tooth being investigated. Nevertheless, in BLV load case the magnitude of the force is maximum, 405N. For the point C1, RPIM and NNRPIM show higher values in comparison to FEM and almost 20-30 MPa is the difference in the results. The normal tooth tolerates more stress than the composites and in the same way, for the points D2, D3, and B as well as C1, the results obtained by meshless methods are much higher than the results calculated by finite element method. It's possible to consider the large displacement of the tooth due to the absence of the boundary condition on the crown of the tooth on the left side, as the main reason of deflection in results between FEM and meshless methods.

Point	Method	Integral (MPa)	Z250 (MPa)	Z100 (MPa)	Herculite XRV Ultra (MPa)
C5	FEM	5.5952	7.4301	8.2087	6.5964
	RPIM	14.21672	14.8627	15.3873	14.2443
	NNRPIM	13.4670	13.5846	14.2223	12.8502
C3	FEM	3.0043	1.5492	1.5717	1.5326
	RPIM	25.3480	21.2172	22.2648	20.2184
	NNRPIM	22.5456	18.4079	19.5268	17.2881
C1	FEM	18.0434	20.3075	19.9072	20.7158
	RPIM	59.6881	49.6677	48.7771	50.9274
	NNRPIM	58.6407	47.9447	46.9156	49.3245
C2	FEM	21.8503	13.9843	14.3727	13.5835
	RPIM	30.2588	6.4873	6.7323	6.2777
	NNRPIM	26.4456	5.5126	5.7269	5.3327
D2	FEM	16.4741	20.3400	20.5958	20.1866
	RPIM	68.6000	51.8678	53.7432	49.8918
	NNRPIM	73.8941	54.2345	56.2879	52.1206
D3	FEM	14.8746	12.0566	12.4032	11.7164
	RPIM	105.7243	108.3852	106.2645	111.3297
	NNRPIM	97.3938	99.8801	97.9097	102.6059
E2	FEM	9.5819	11.7963	9.8119	14.01724
	RPIM	22.4015	36.7175	35.8006	38.1626
	NNRPIM	24.1321	37.0049	36.0867	38.4068
D1	FEM	45.4805	46.6307	44.8450	48.0606
	RPIM	50.8510	48.8107	47.3982	50.3479
	NNRPIM	44.5052	42.1236	40.9082	43.4088
B	FEM	21.7572	19.1773	19.2216	18.8358
	RPIM	61.7801	56.7008	55.0999	58.7133
	NNRPIM	58.0249	53.2134	51.6836	55.1382

Table 6. 6. Effective stress for each interest point obtained by FEM and meshless methods for BLV load case

All the isomaps (von Mises stresses) obtained for all four load cases are shown in table 6.7 for OLV load case, table 6.8 for ORV load case, table 6.9 for BRV and 6.10 for BLV load case. All these captured isomaps visually show the results represented previously for a normal tooth and three commercial dental restorative composites implemented by meshless methods and finite element method. According to these isomaps, stress is observed mostly on the borders, close to boundary conditions, either natural boundary conditions or essential boundary conditions. Nevertheless, the maximum stress for OLV, ORV, and BRV is in the zone under oblique load. On the other hand, in the BLV load case, the maximum stress distribution is mostly on the left side of the tooth, starting from the region under oblique load, smoothly gets curved and goes to cortical bone and the spot on the border between the cortical bone and the dentine of the tooth is standing the highest amount of stress.

Materials	FEM	RPIM	NNRPIM
Integral	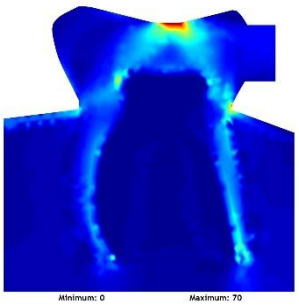	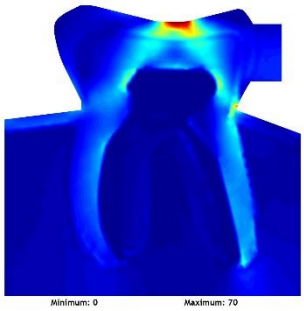	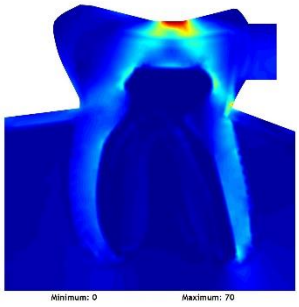
Z250	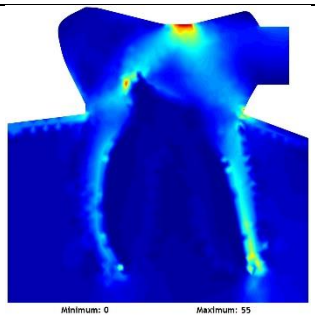	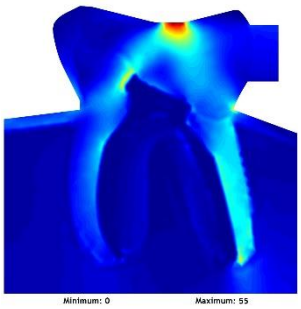	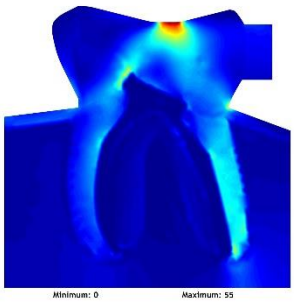
Z100	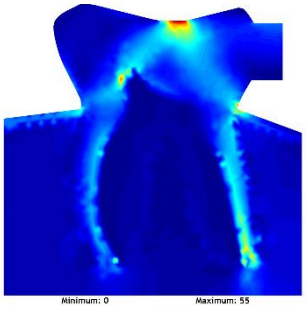	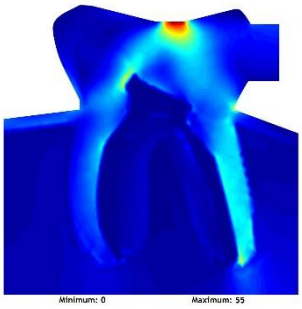	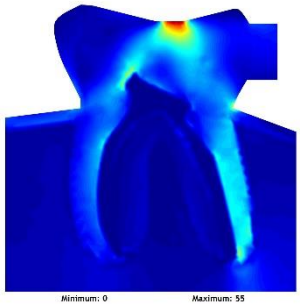
Herculite XRV Ultra	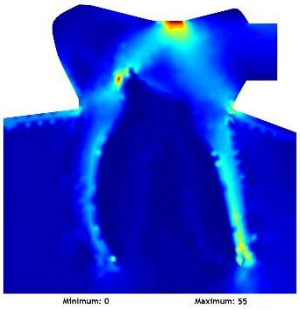	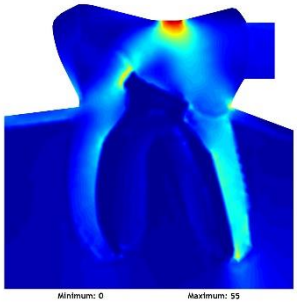	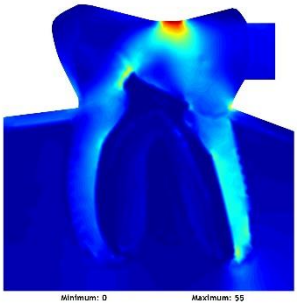
			

Table 6. 7. OLV load case: Final von Mises effective stress isomap for all considered materials obtained by FEM, RPIM, and NNRPIM

Materials	FEM	RPIM	NNRPIM
Integral	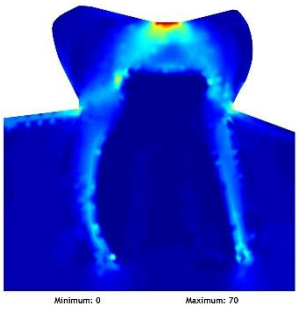	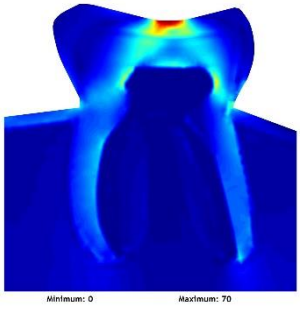	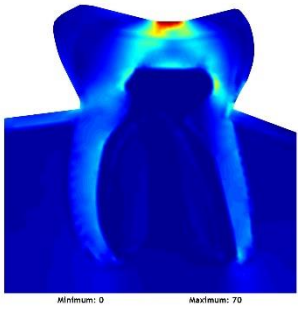
Z250	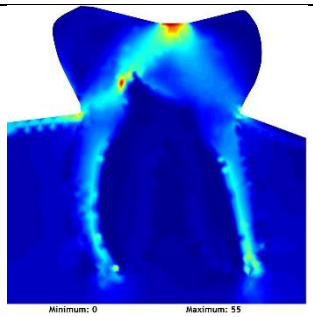	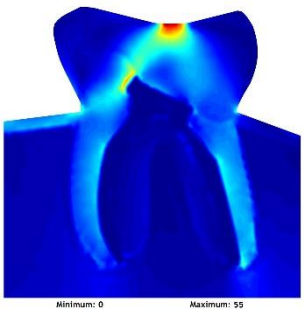	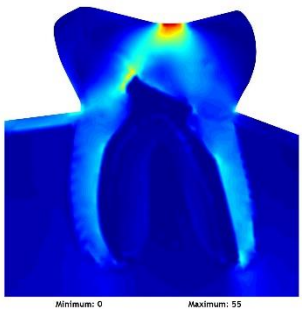
Z100	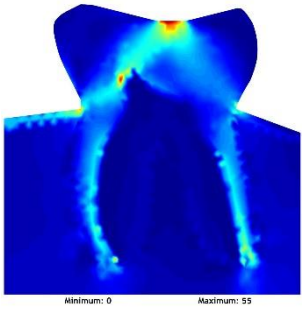	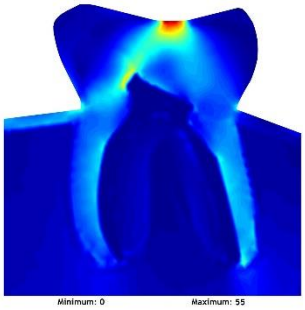	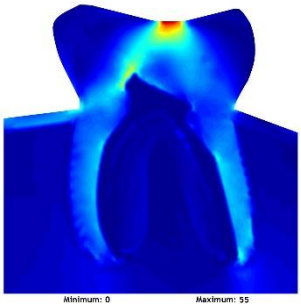
Herculite XRV Ultra	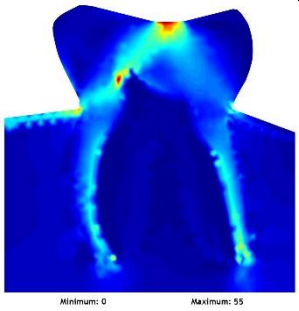	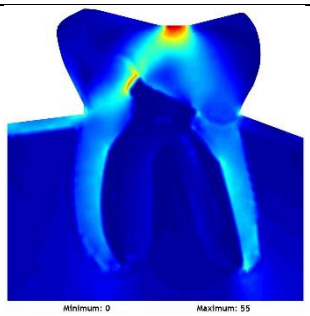	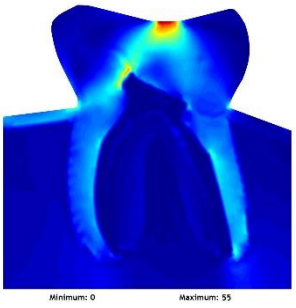
 [MPa]			

Table 6. 8. ORV load case: Final von Mises effective stress isomap for all considered materials obtained by FEM, RPIM, and NNRPIM

Materials	FEM	RPIM	NNRPIM
Integral	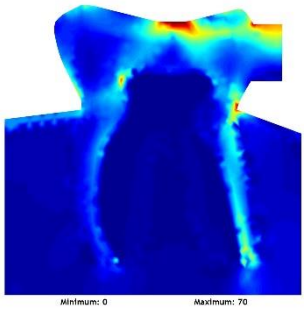	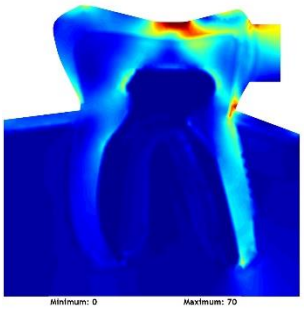	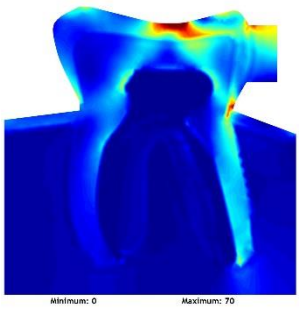
Z250	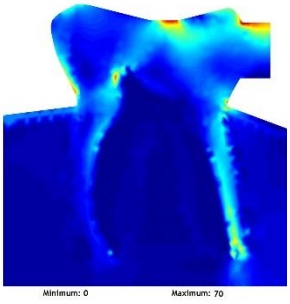	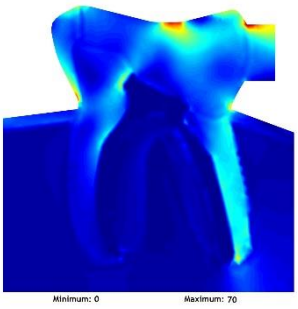	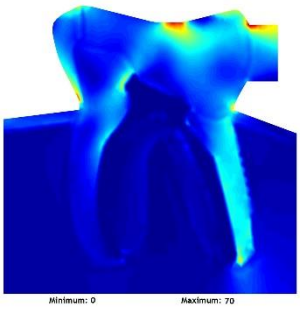
Z100	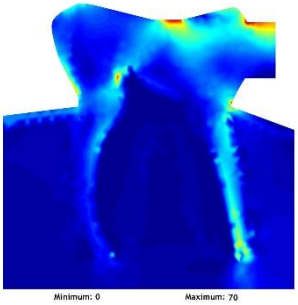	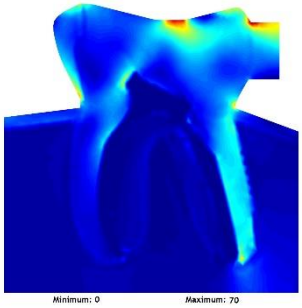	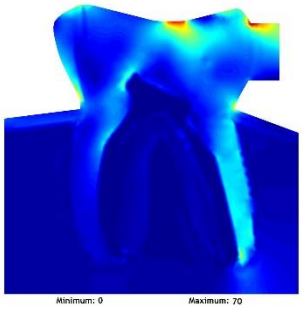
Herculite XRV Ultra	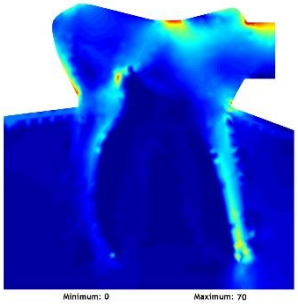	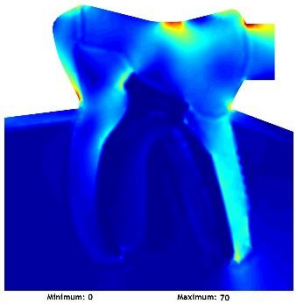	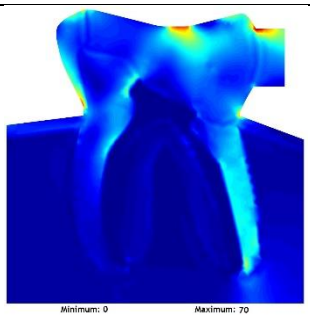
	 Min Max [MPa]		

Table 6. 9. BRV load case: Final von Mises effective stress isomap for all considered materials obtained by FEM, RPIM, and NNRPIM

Materials	FEM	RPIM	NNRPIM
Integral	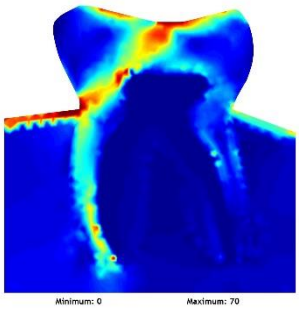	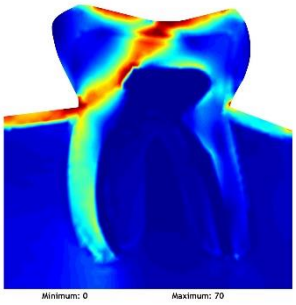	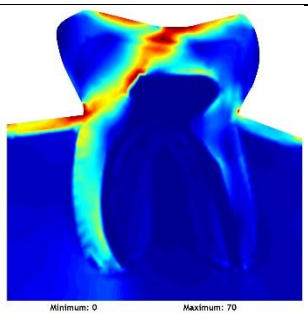
Z250	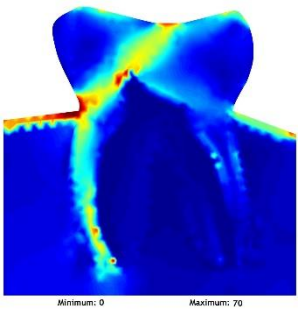	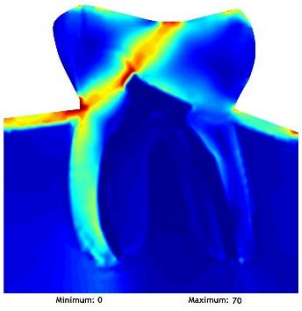	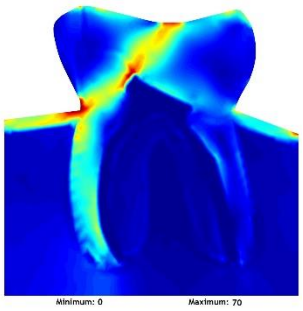
Z100	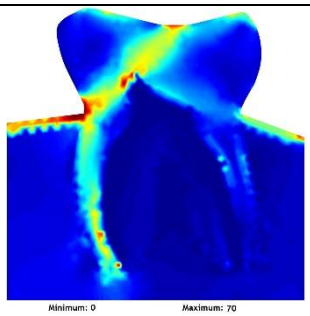	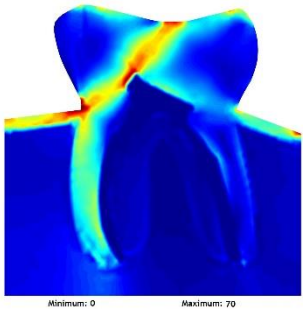	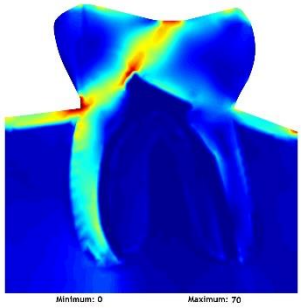
Herculite XRV Ultra	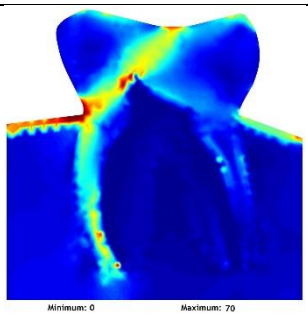	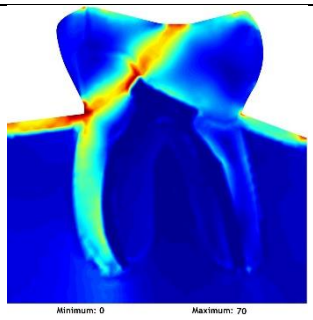	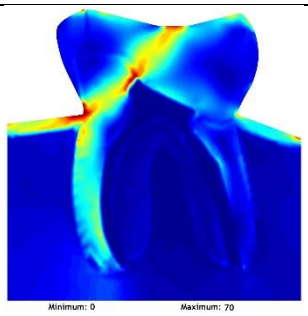
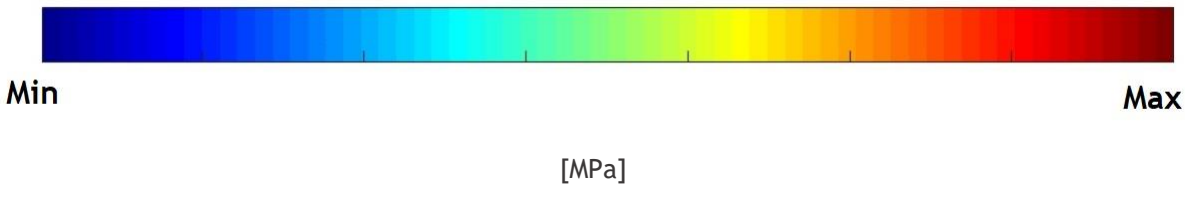			

Table 6. 10. BLV load case: Final von Mises effective stress isomap for all considered materials obtained by FEM, RPIM, and NNRPIM

6.2 Elasto-plastic Analysis

6.2.1 Model description and process

The same model under the same load cases which are already expressed in section 6.1.1, was used to perform elasto-plastic analyses. For this aim, two commercial materials are imposed as the dental restorative composites. The first material is Tetric N-Ceram Bulk™ produced by Ivoclar Vivadent ™ and the second one is Filtek Z250™ produced by 3M™. For the mechanical properties for these materials, please check out chapter 2, section 2.3.2 (Novel Materials and Techniques). The analysis on both materials for all four load cases is performed with the aid of Finite Element Method, and meshless methods including Radial Point Interpolation Method, and Natural Neighbor Radial Point Interpolation Method. All the results are compared to each other for each load case and material. The graphs are obtained regarding Load-Displacement, Load-Plastic Strain, Effective Stress-Effective Strain, and finally Effective Stress-Plastic Strain. Nevertheless, the growth of plastic zone on the materials is captured in 5 pictures during the process to make it easier to see how the materials plasticizes. The results are obtained for four different points on the tooth, see Figure 6.5. These points (C3, C7, P1, and P2) are chosen due to their close distance from border lines of the composite and normal tooth and being critical either taking plastic behavior or maintaining the elastic behavior as it will be revealed in the next sections.

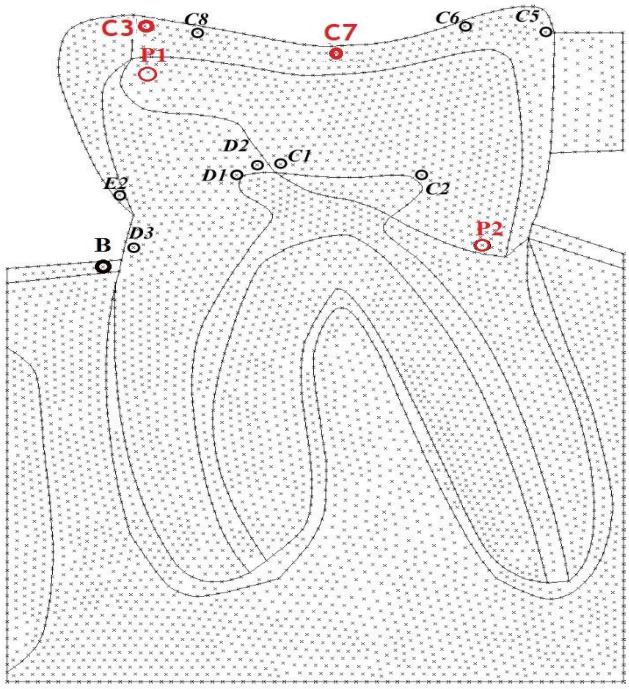

Figure 6. 5. Interested points for results in elasto-plastic analysis, highlighting the points C3, C7, P1, and P2

6.2.2 Results for NC-B

The analysis for this material is done under four loading situations, similar to the elasto-static section. The growth of the plastic zone in this material, for BLV, BRV, OLV, and ORV are shown in figure 6.3, 6.4, 6.5, and 6.6, respectively. According to the captured pictures, the initial plastic zone is usually in the region under force, almost in the same orientation of the load and finally, the plastic zone grows until the border of the dental restorative material with the rest of tooth. Furthermore, on the right side, the region that the cortical point gets to the tooth, contains an initial plastic zone which finally grows to catch the plastic zone started from the force zone and finally a big zone of plastic behavior comes to appear.

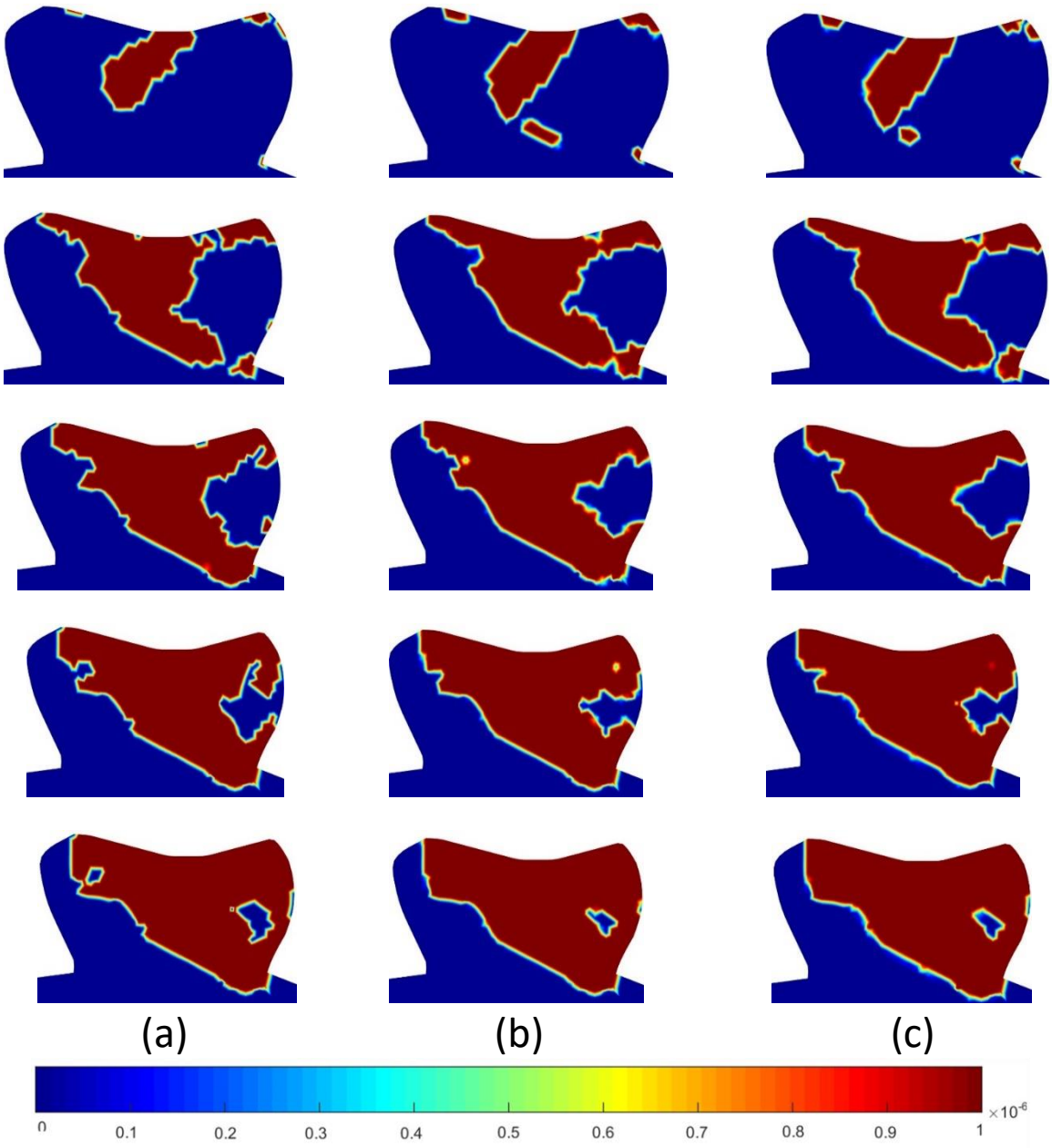

Figure 6. 6. Plastic zone growth on NC-B in the BLV load case. (a) FEM (b) RPIM (c) NNRPIM

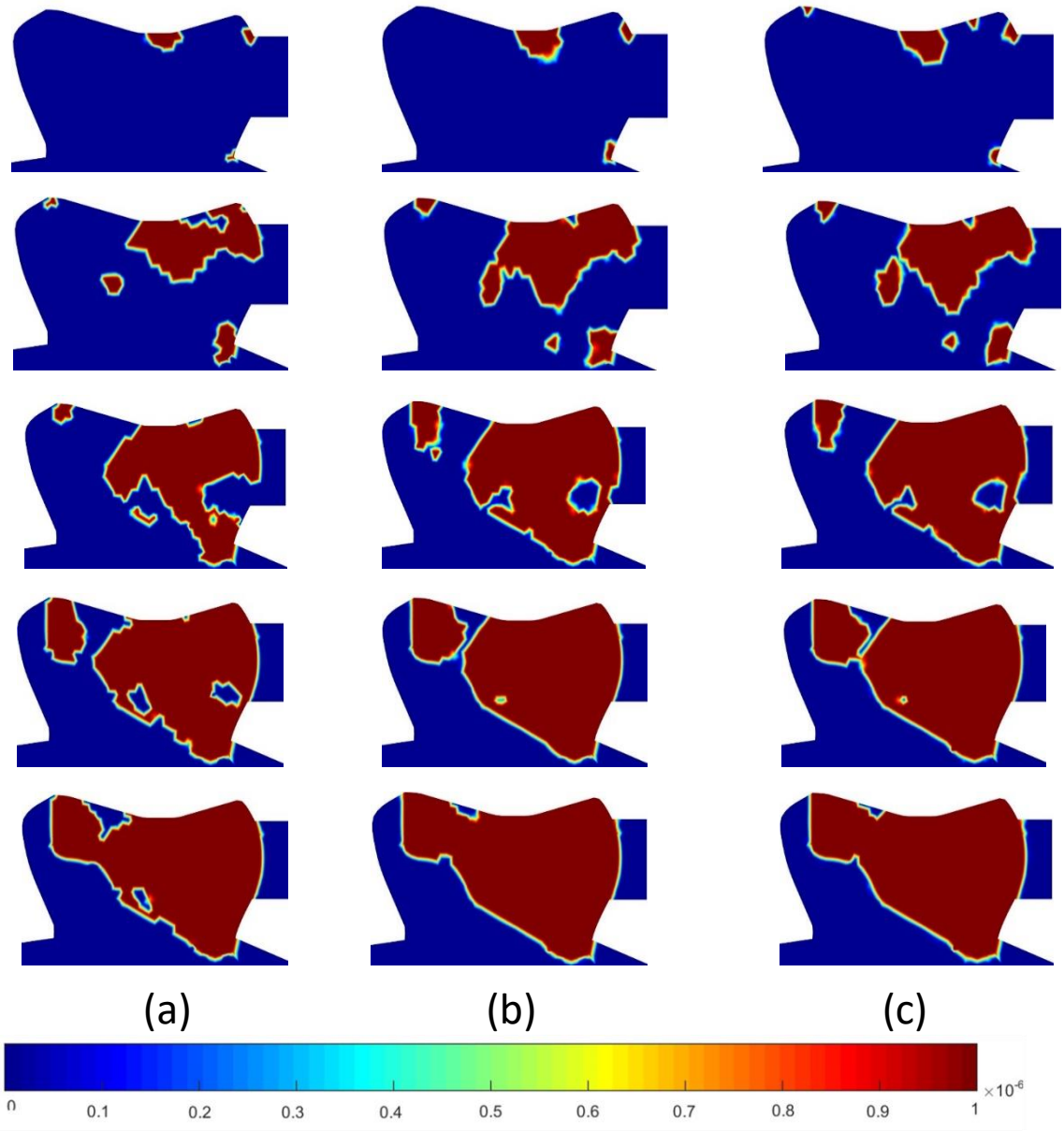

Figure 6. 7. Plastic zone growth on NC-B in the BRV load case. (a) FEM (b) RPIM (c) NNRPIM

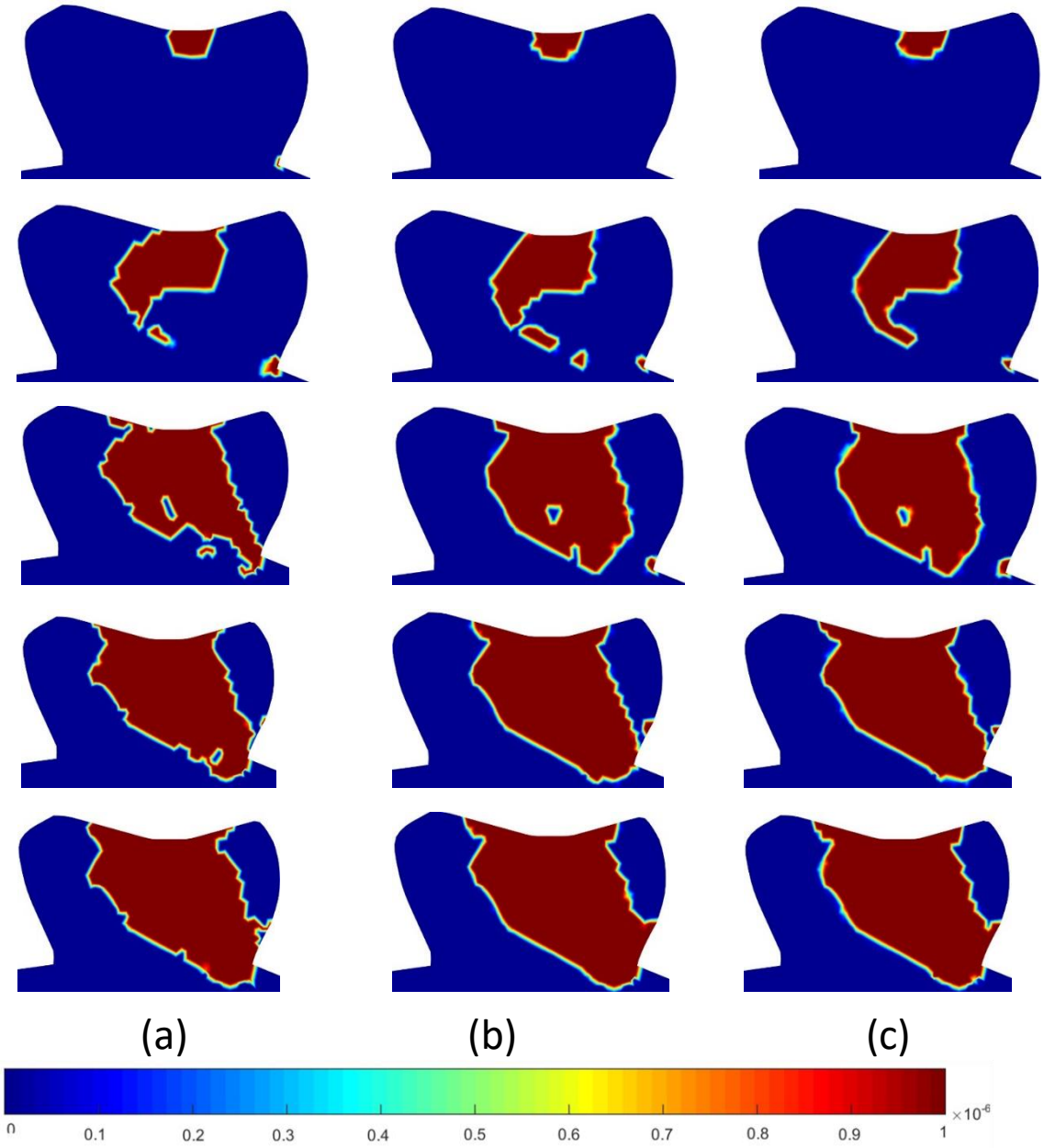

Figure 6. 8. Plastic zone growth on NC-B in the OLV load case. (a) FEM (b) RPIM (c) NNRPIM

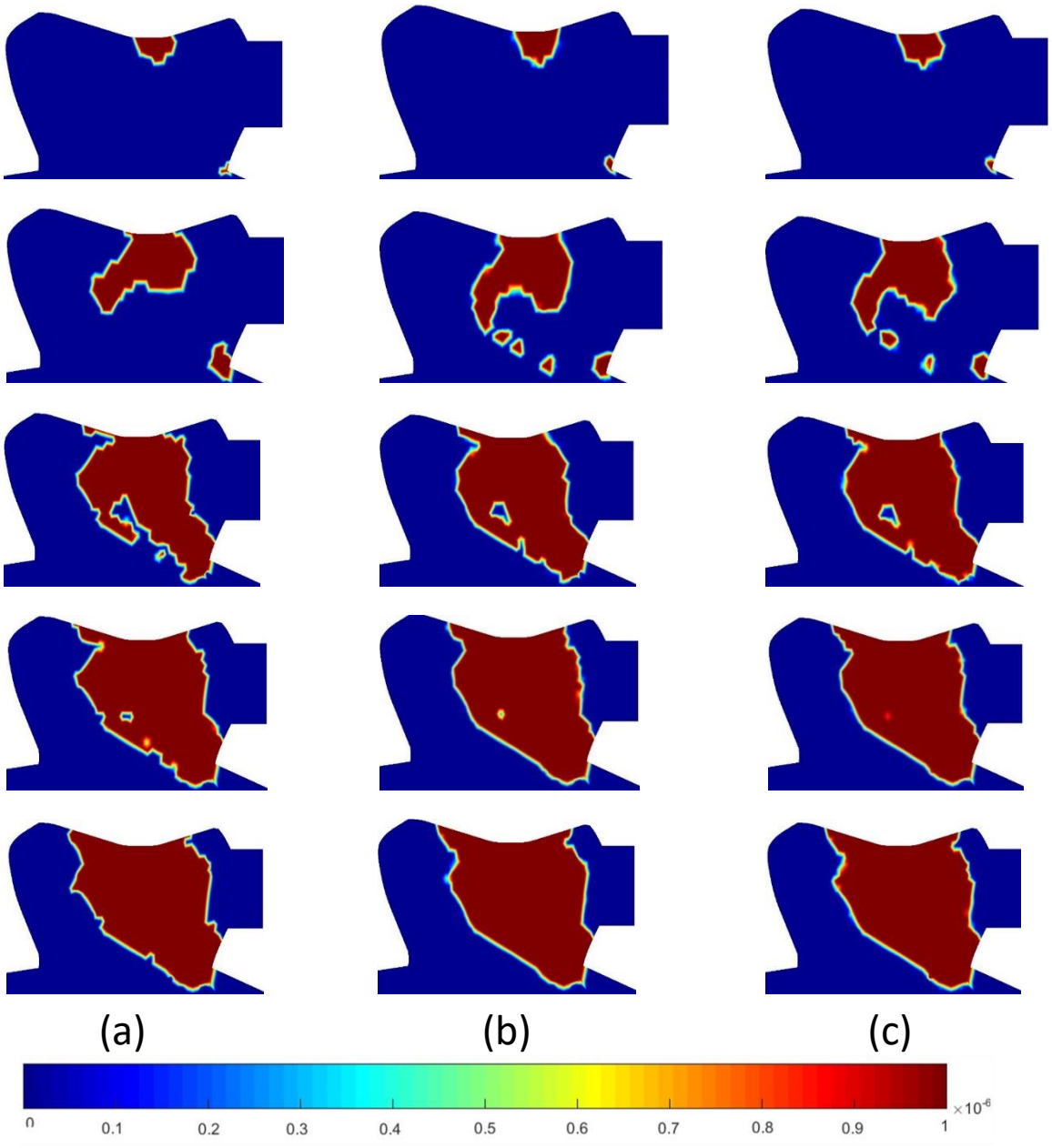

Figure 6. 9. Plastic zone growth on NC-B in the ORV load case. (a) FEM (b) RPIM (c) NNRPIM

The load-displacement graph for the BLV load case shown in figure 6.7, indicates a smooth elasto-plastic behavior for all the interested points. The maximum displacement goes for C3, which is almost 5mm based on FEM analysis, and almost 4mm based on the meshless analysis. More likely the plastic behavior starts when the lead reaches to 1000N.

Figure 6.8, shows the same graph for BRV load case, in this case, the displacement does not go up more than 2.5 mm, which belongs to C7. In contrast to the prior load case, for BRV the finite element method shows values less than meshless methods, except for the point P2. On the point P2, there is a significant deviation between FEM and meshless methods almost from the beginning. For the other points, the difference between the values is not considerable.

In the OLV load case depicted in figure 6.9, for the points C3 and P1, plastic behavior is not evident. However, C7 obviously experiences a plastic behavior and P2 according to FEM result would enter to plastic zone but based on the meshless graph, it does not. In order to come over this doubt, the Load-Plastic Strain graph can help, where the graph for point P2 shows the small value of plastic strain for three of the methods, maximum 0.03. Furthermore, this graph proves that for the points C3 and P1 there is no plastic behavior.

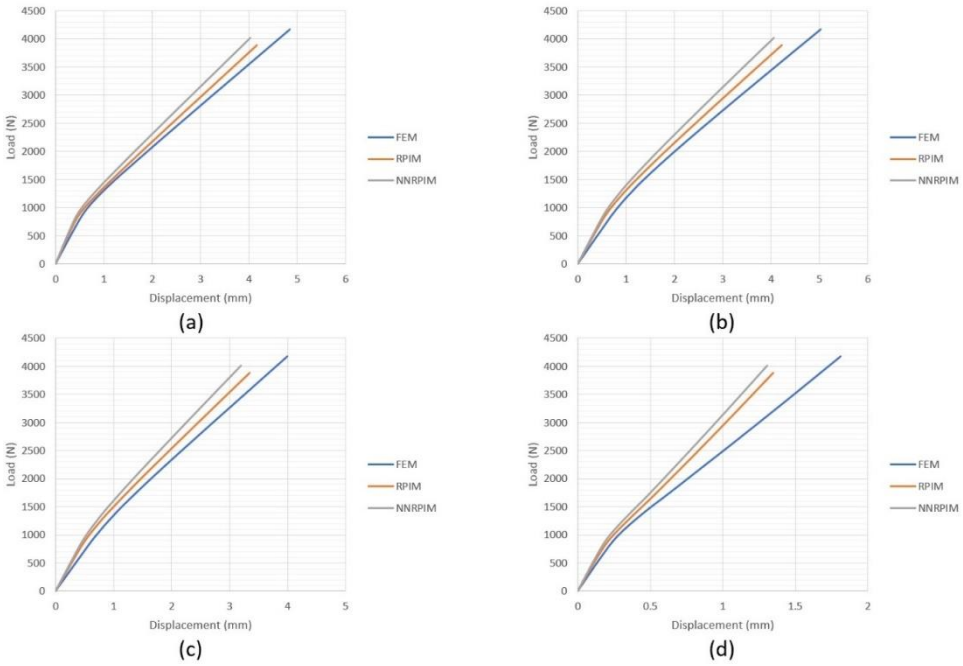

Figure 6. 10. Load-Displacement graph for the BLV load case. (a) C7 (b) C3 (c) P1 (d) P2

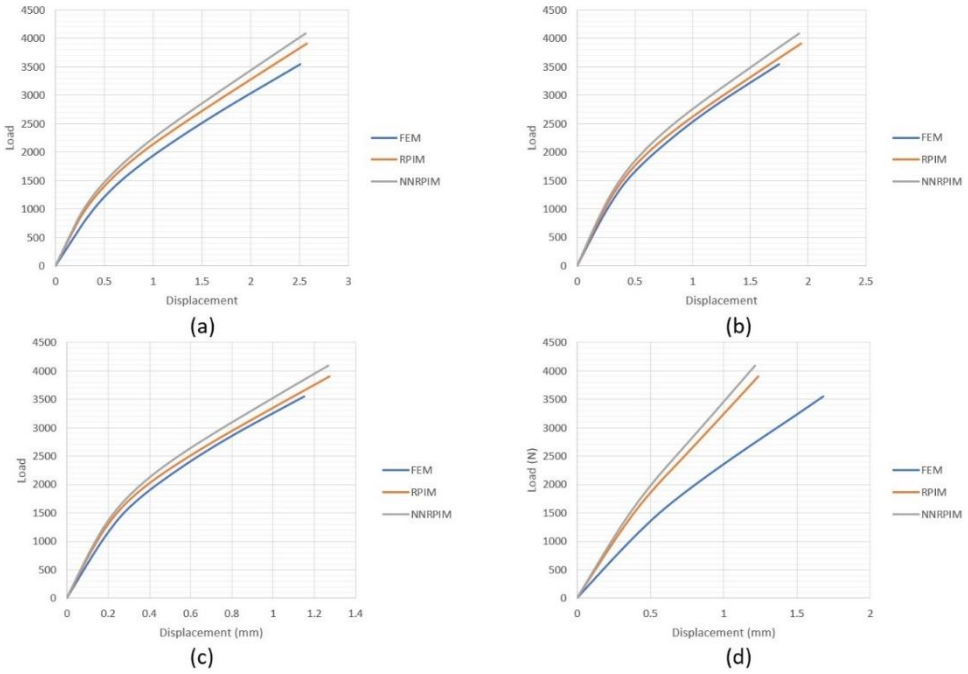

Figure 6. 11. Load-Displacement graph for the BRV load case. (a) C7 (b) C3 (c) P1 (d) P2

In the OLV load case depicted in figure 6.9, for the points C3 and P1, plastic behavior is not observed. However, C7 obviously experiences a plastic behavior and P2 according to FEM result would enter to plastic zone but based on the meshless graph, it does not enter the plastic zone. In order to come over this doubt, the Load-Plastic Strain graph can help, where the graph for point P2 shows the small value of plastic strain for three of the methods, maximum 0.03. Furthermore, this graph proves that for the points C3 and P1 there is no plastic behavior.

According to the results for ORV load case, for the points C7 and P2, plastic behavior is demonstrated and there is an excellent agreement between meshless methods and finite element method for the point C7 where the values are close to each other. In contrast to the mentioned points, for the points C3 and P1, the plastic behavior is not obvious in load-displacement graph. Thus, visualizing the load-plastic strain and the graph effective stress-plastic strain, it can be observed that there is no plastic behavior in these points.

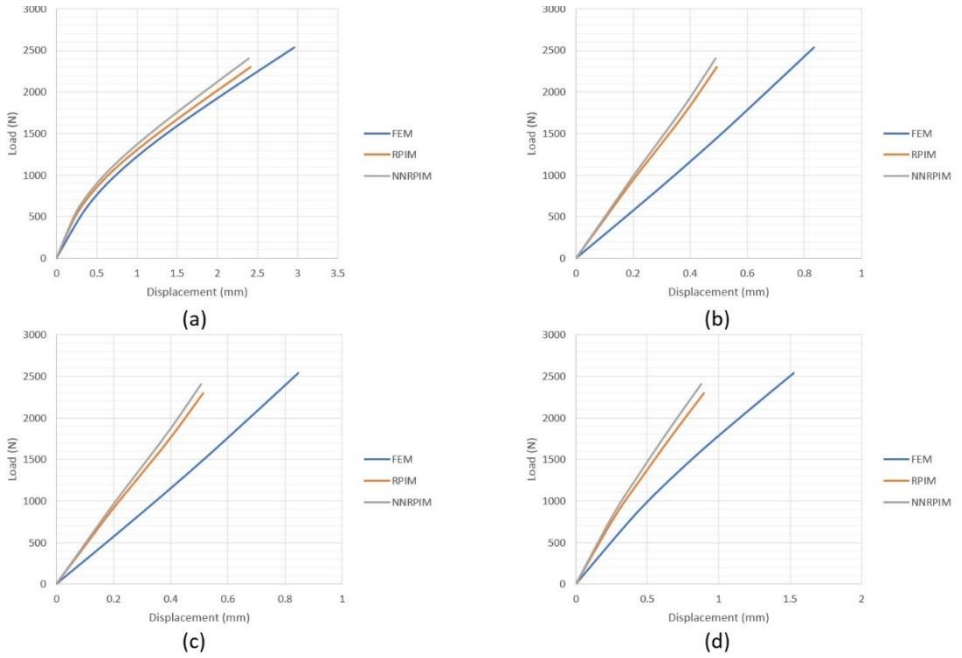

Figure 6. 12. Load-Displacement graph for the OLV load case. (a) C7 (b) C3 (c) P1 (d) P2

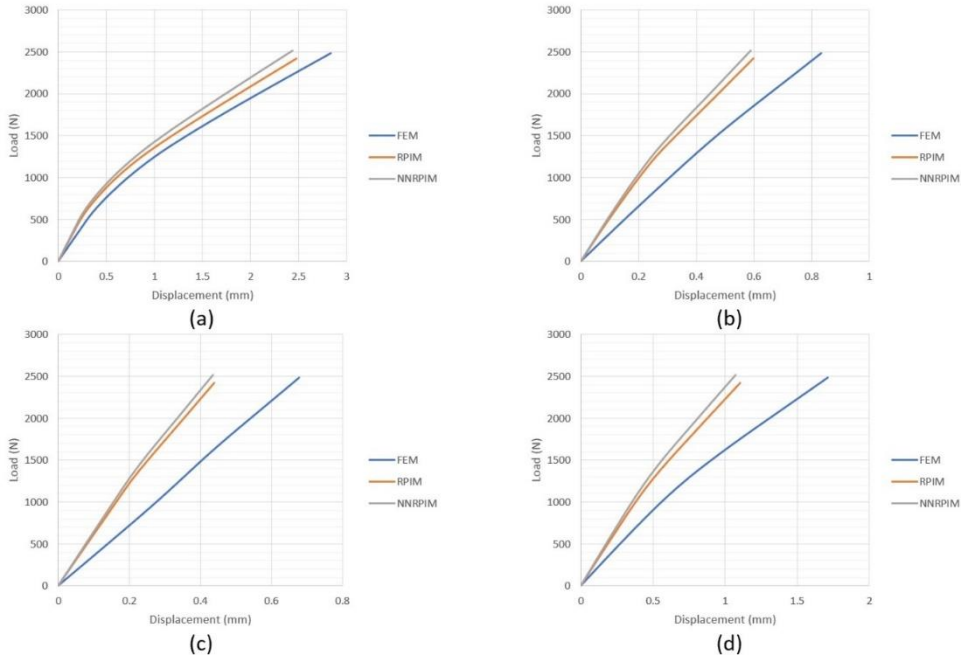

Figure 6. 13. Load-Displacement graph for the ORV load case. (a) C7 (b) C3 (c) P1 (d) P2

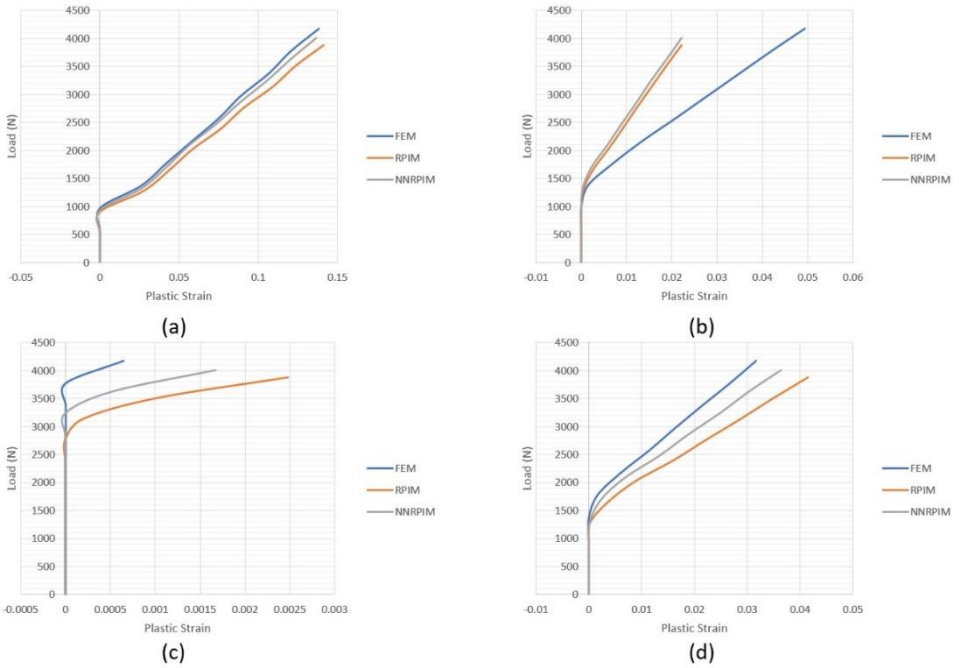

Figure 6. 14. Load-Plastic Strain graph for the BLV load case. (a) C7 (b) C3 (c) P1 (d) P2

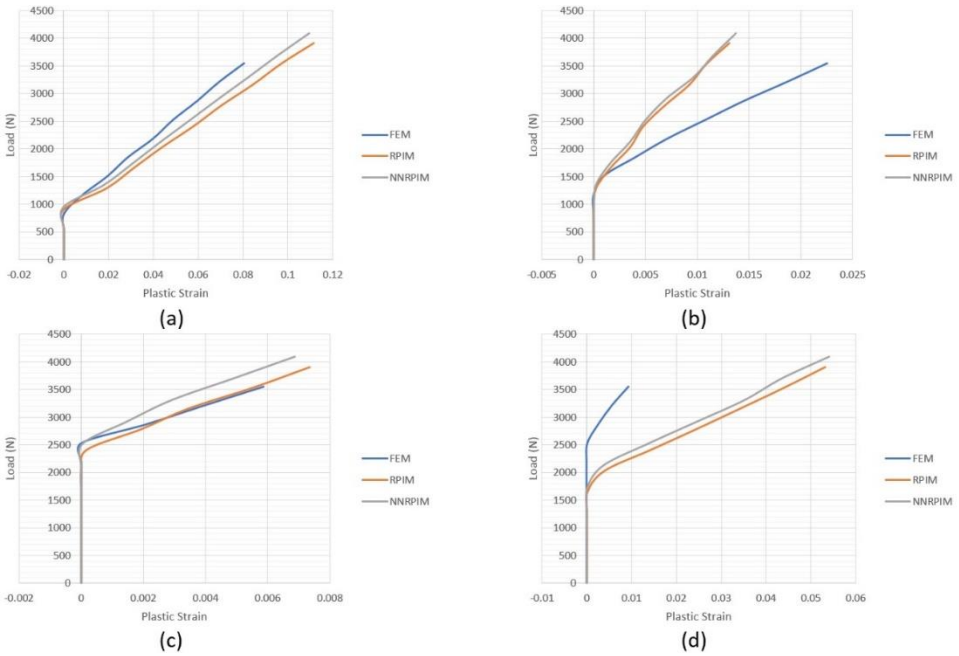

Figure 6. 15. Load-Plastic Strain graph for the BRV load case. (a) C7 (b) C3 (c) P1 (d) P2

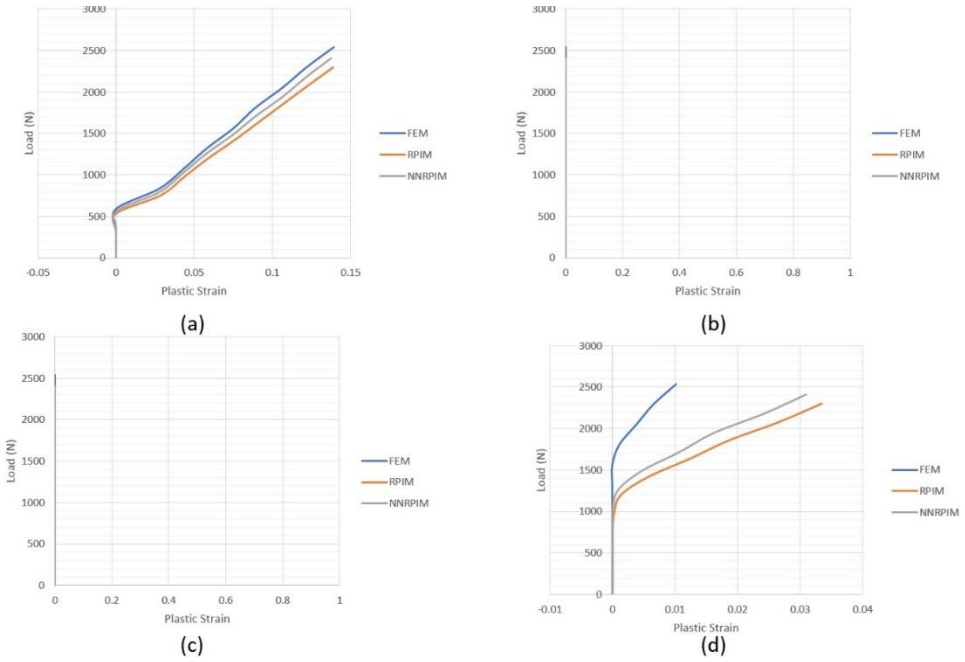

Figure 6. 16. Load-Plastic Strain graph for the OLV load case. (a) C7 (b) C3 (c) P1 (d) P2

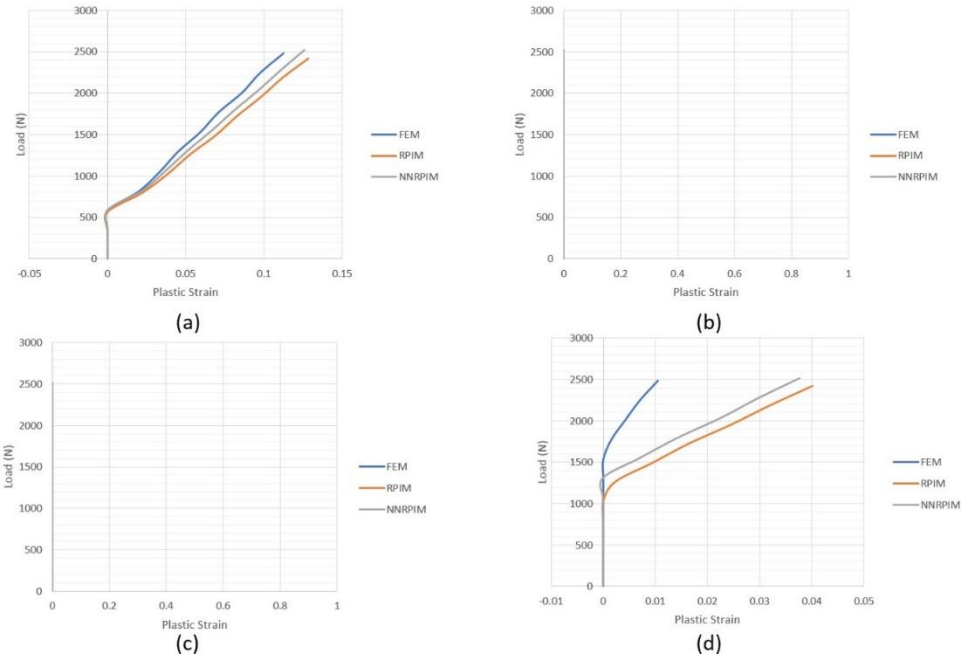

Figure 6. 17. Load-Plastic Strain graph for the ORV load case. (a) C7 (b) C3 (c) P1 (d) P2

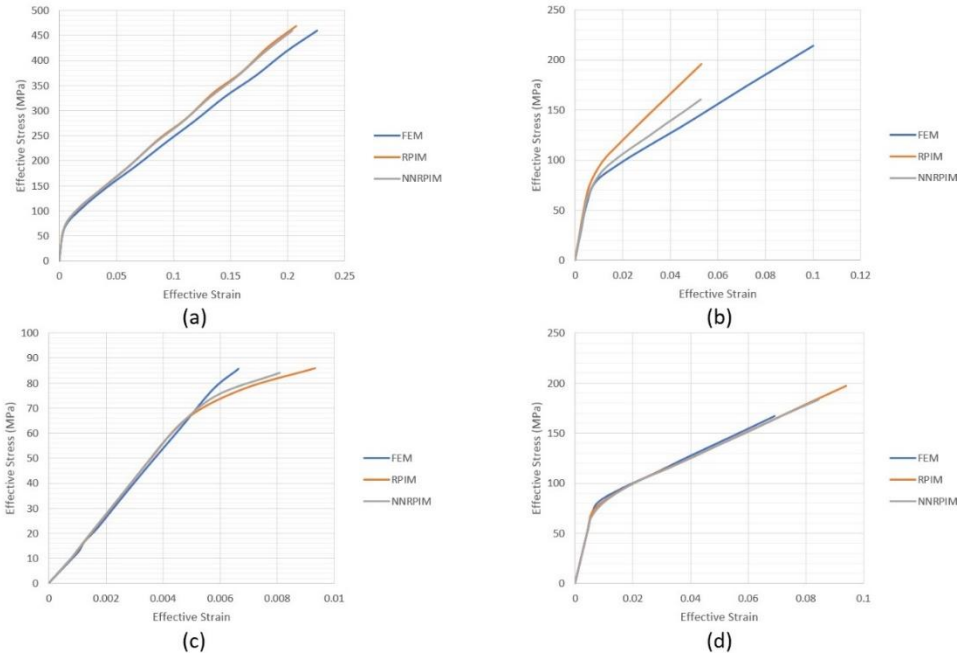

Figure 6. 18. Effective Stress-Effective Strain graph for the BLV load case. (a) C7 (b) C3 (c) P1 (d) P2

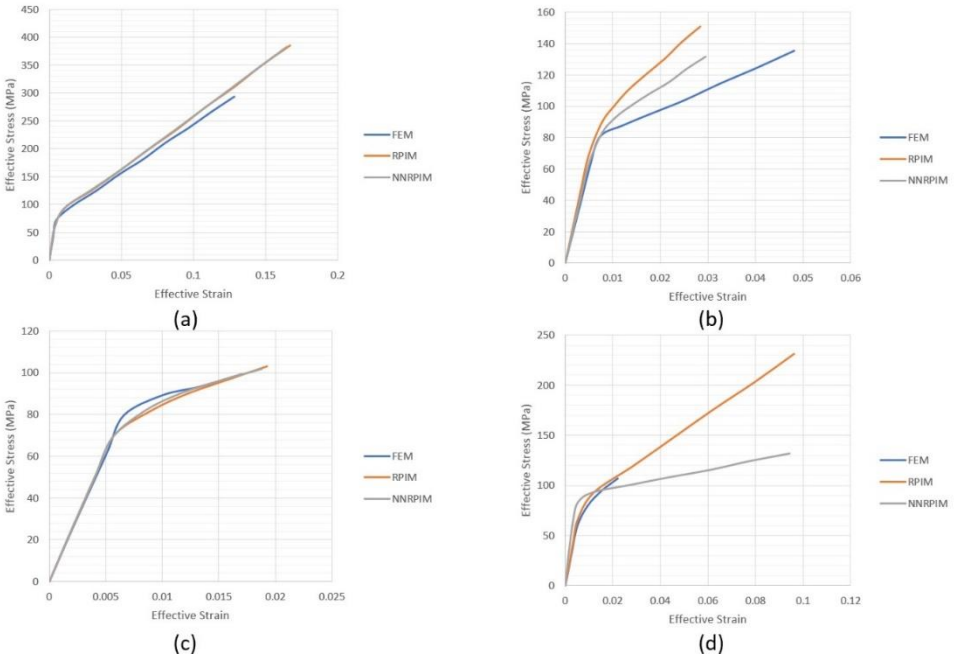

Figure 6. 19. Effective Stress-Effective Strain graph for the BRV load case. (a) C7 (b) C3 (c) P1 (d) P2

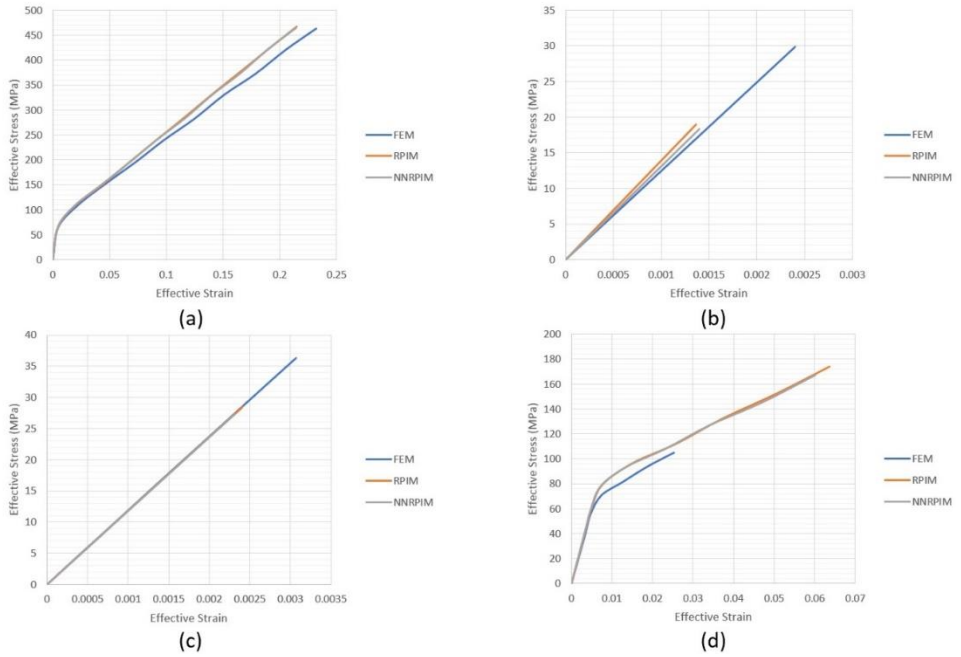

Figure 6. 20. Effective Stress-Effective Strain graph for the OLV load case. (a) C7 (b) C3 (c) P1 (d) P2

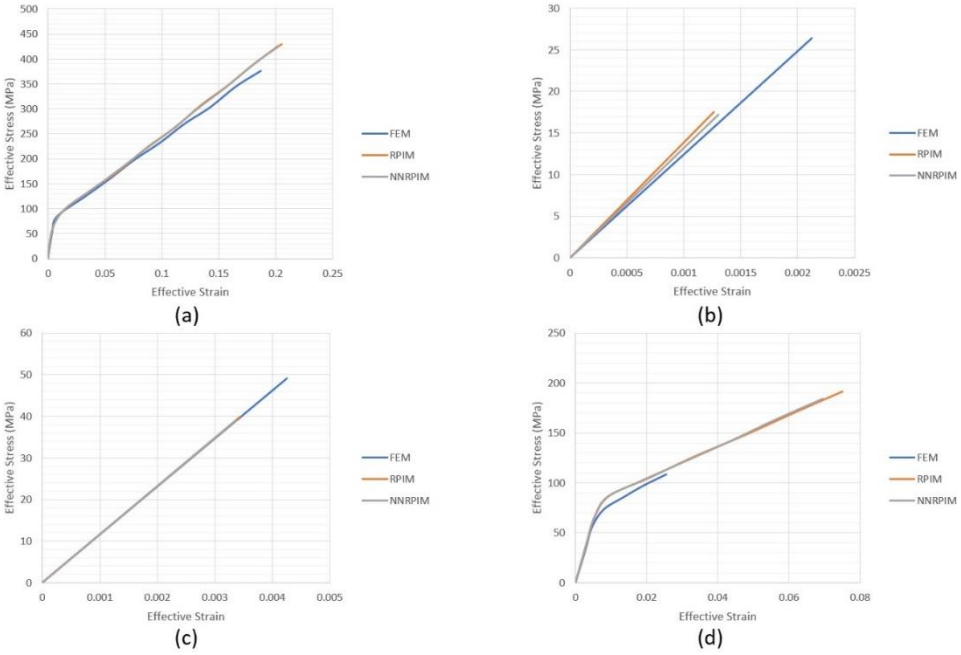

Figure 6. 21. Effective Stress-Effective Strain graph for the ORV load case. (a) C7 (b) C3 (c) P1 (d) P2

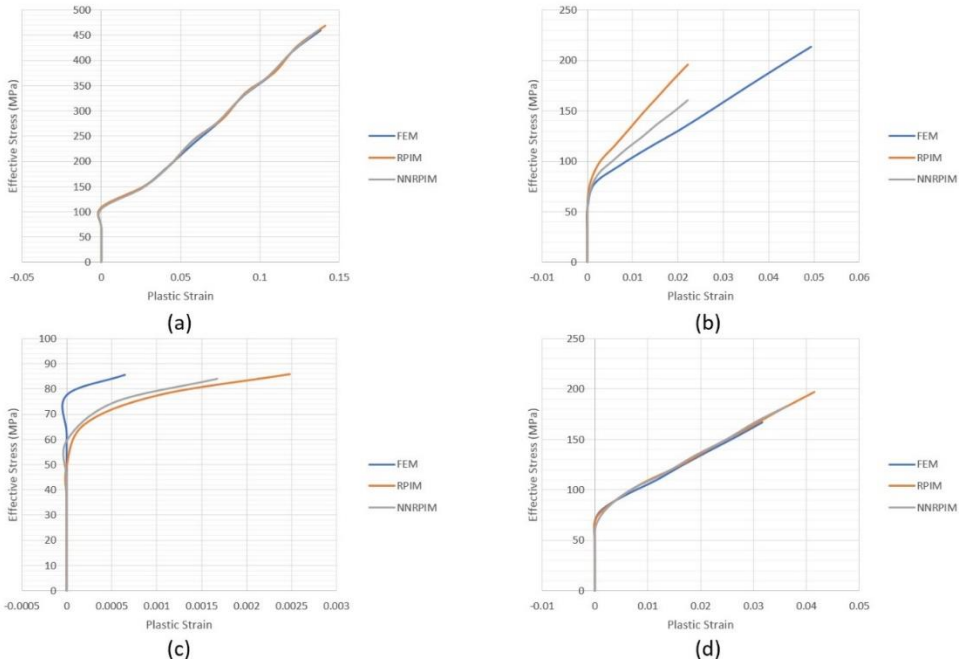

Figure 6. 22. Effective Stress-Plastic Strain graph for the BLV load case. (a) C7 (b) C3 (c) P1 (d) P2

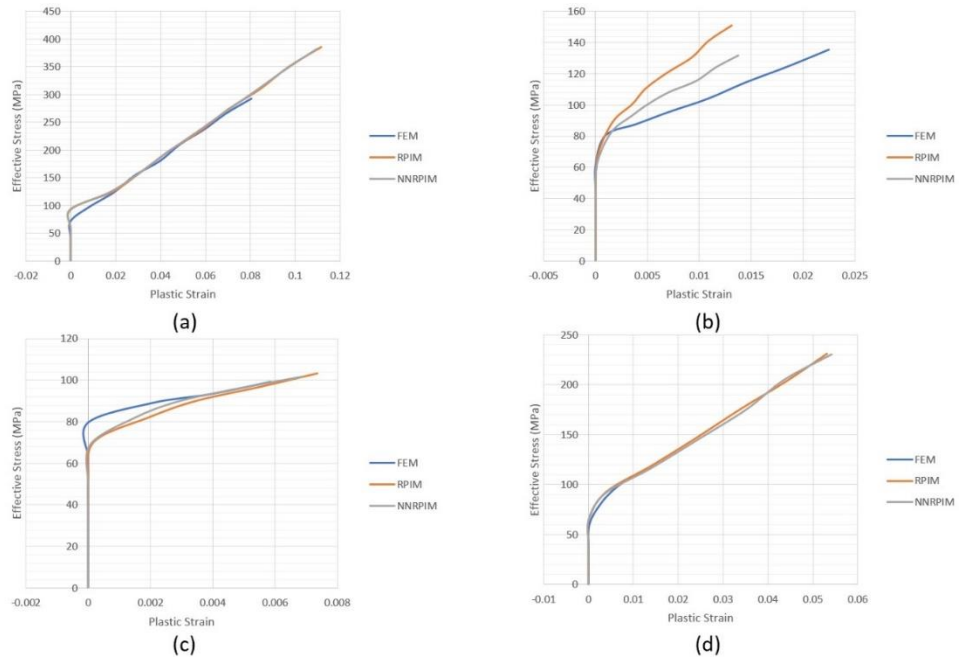

Figure 6. 23. Effective Stress-Plastic Strain graph for the BRV load case. (a) C7 (b) C3 (c) P1 (d) P2

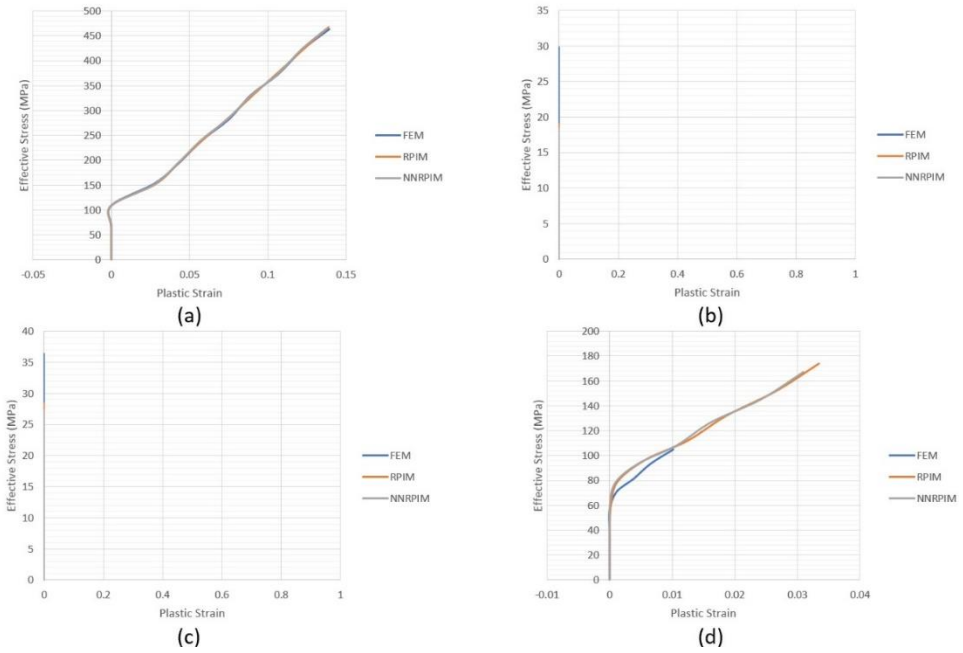

Figure 6. 24. Effective Stress-Plastic Strain graph for the OLV load case. (a) C7 (b) C3 (c) P1 (d) P2

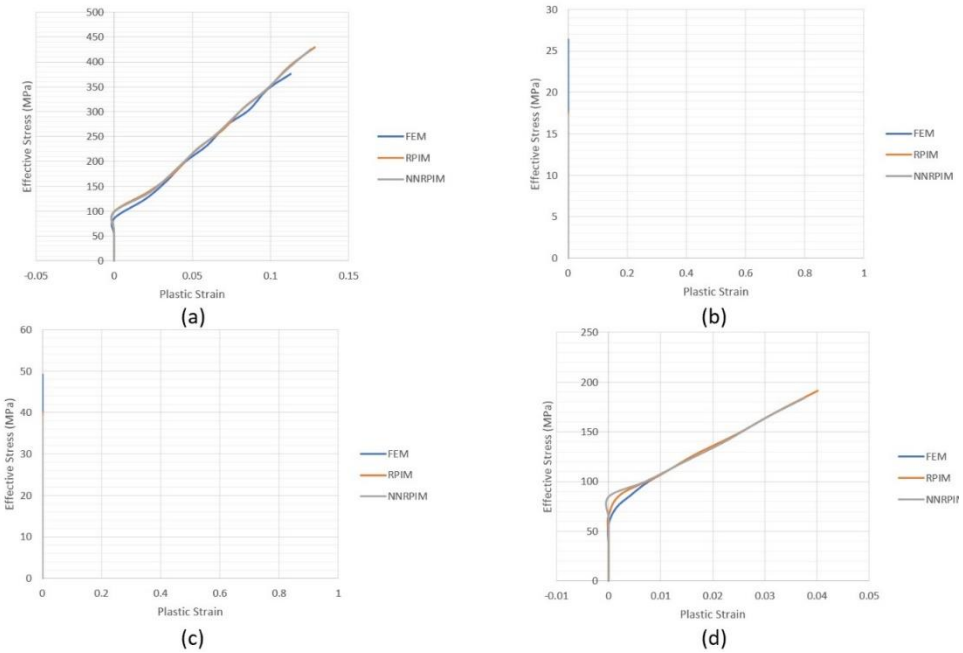

Figure 6. 25. Effective Stress-Plastic Strain graph for the ORV load case. (a) C7 (b) C3 (c) P1 (d) P2

6.2.3 Results for Z250™

In this section, the zone for restoration is replaced by Filtek Z250™ and the growth of the plastic zone from first step to the final increment is represented in figure 6.26, 6.27, 6.28, and 6.29 for BLV, BRV, OLV, and ORV load cases, respectively. As well as N-Ceram Bulk™ , the orientation of the growth is in the same direction of load and also plastic region in the contact zone between the tooth and cortical bone on the right-side initiates and comes up to the border line of the composite. In the final captured isomap, in the last increment, they all form a large plastic zone.

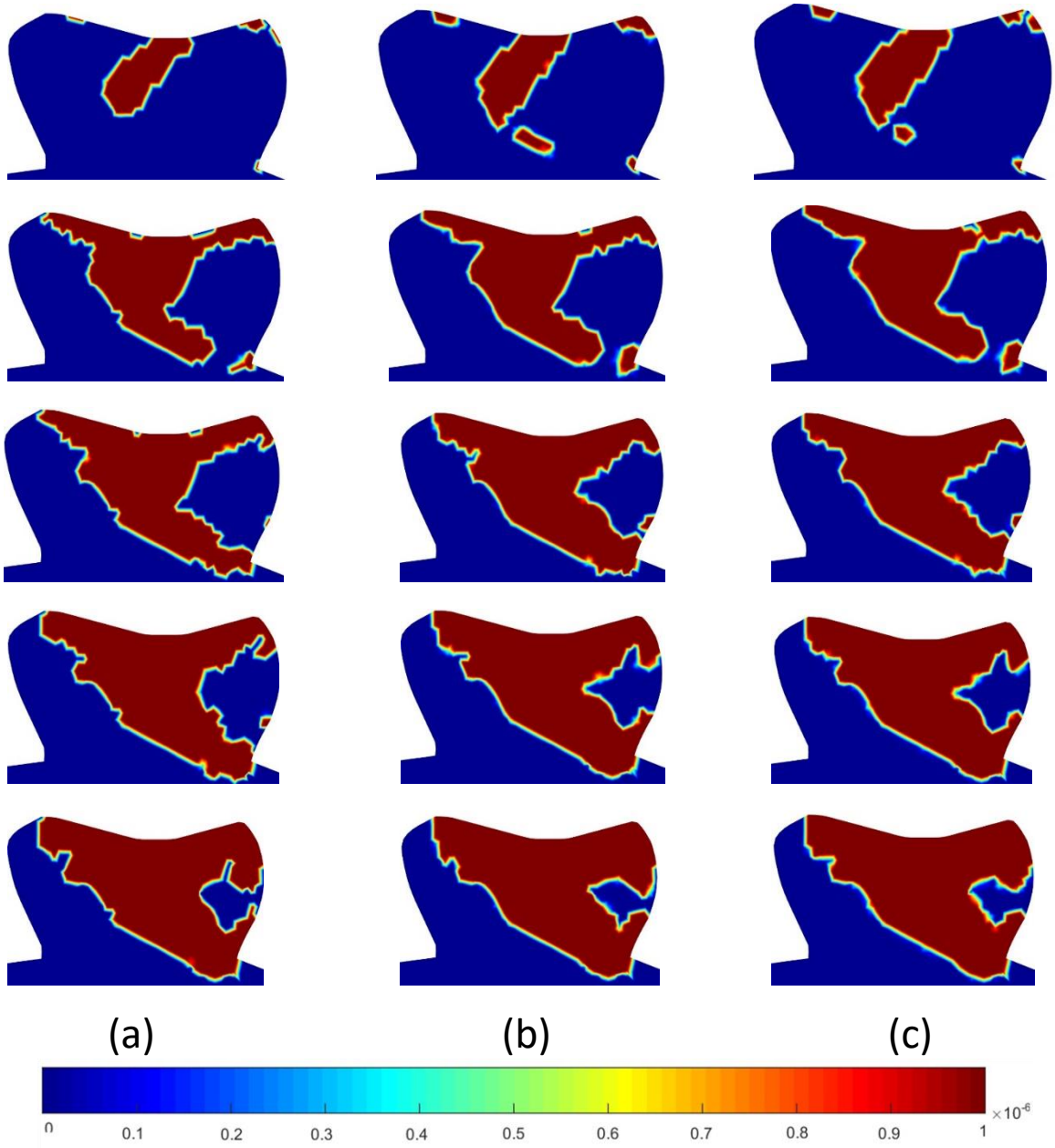

Figure 6. 26. Plastic zone growth on Z250 in the BLV load case. (a) FEM (b) RPIM (c) NNRPIM

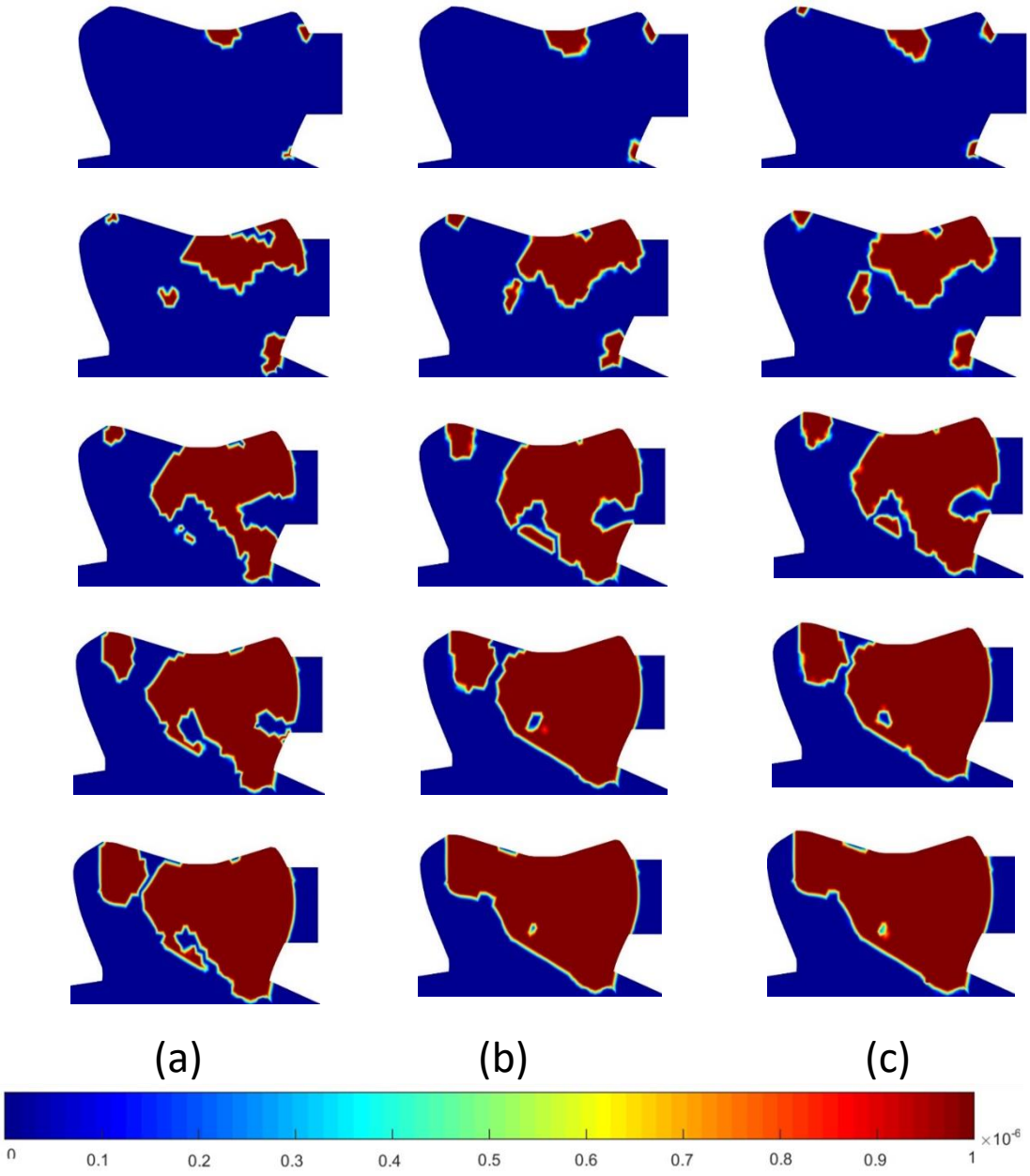

Figure 6. 27. Plastic zone growth on Z250 in the BRV load case. (a) FEM (b) RPIM (c) NNRPIM

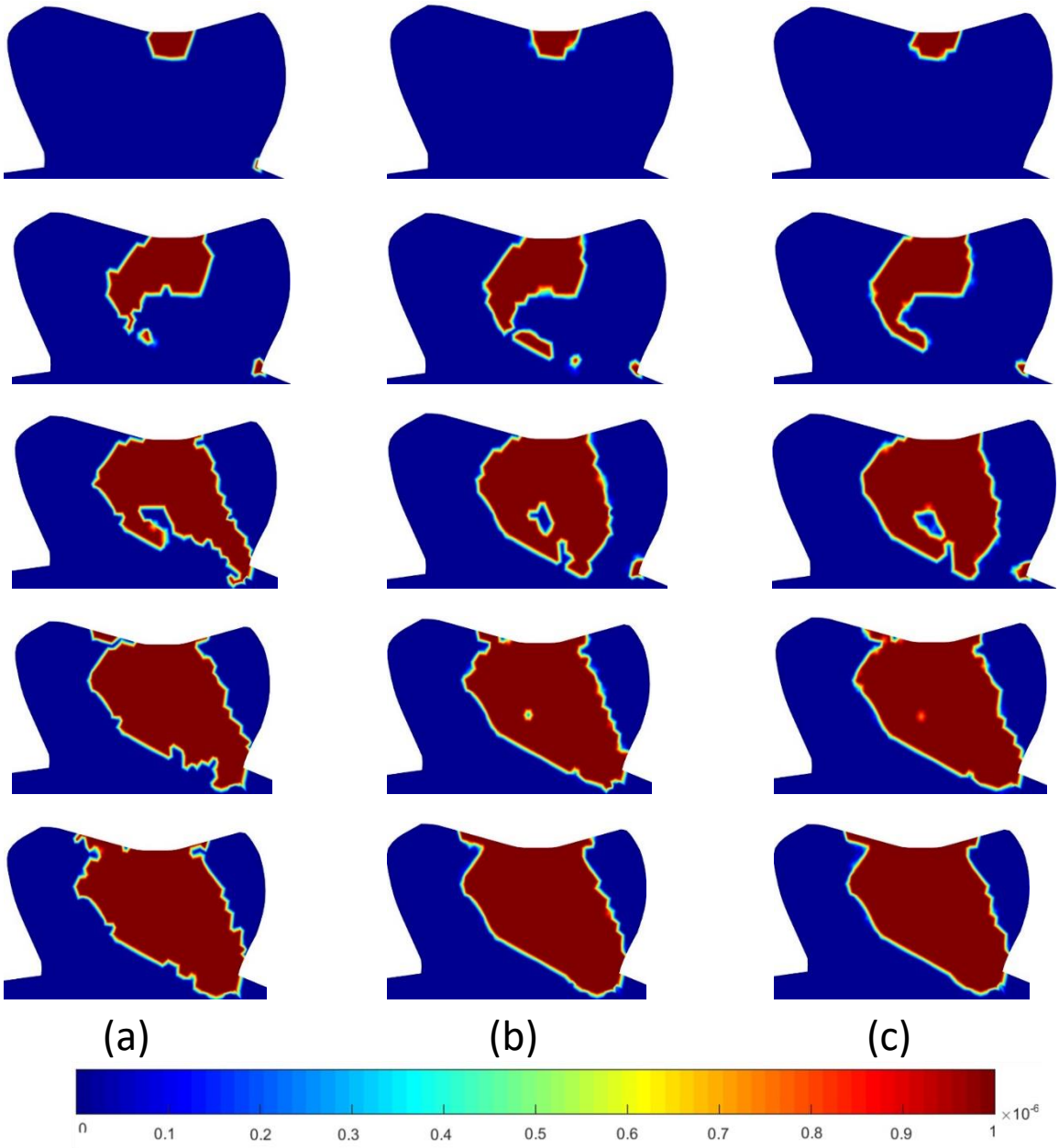

Figure 6. 28. Plastic zone growth on Z250 in the OLV load case. (a) FEM (b) RPIM (c) NNRPIM

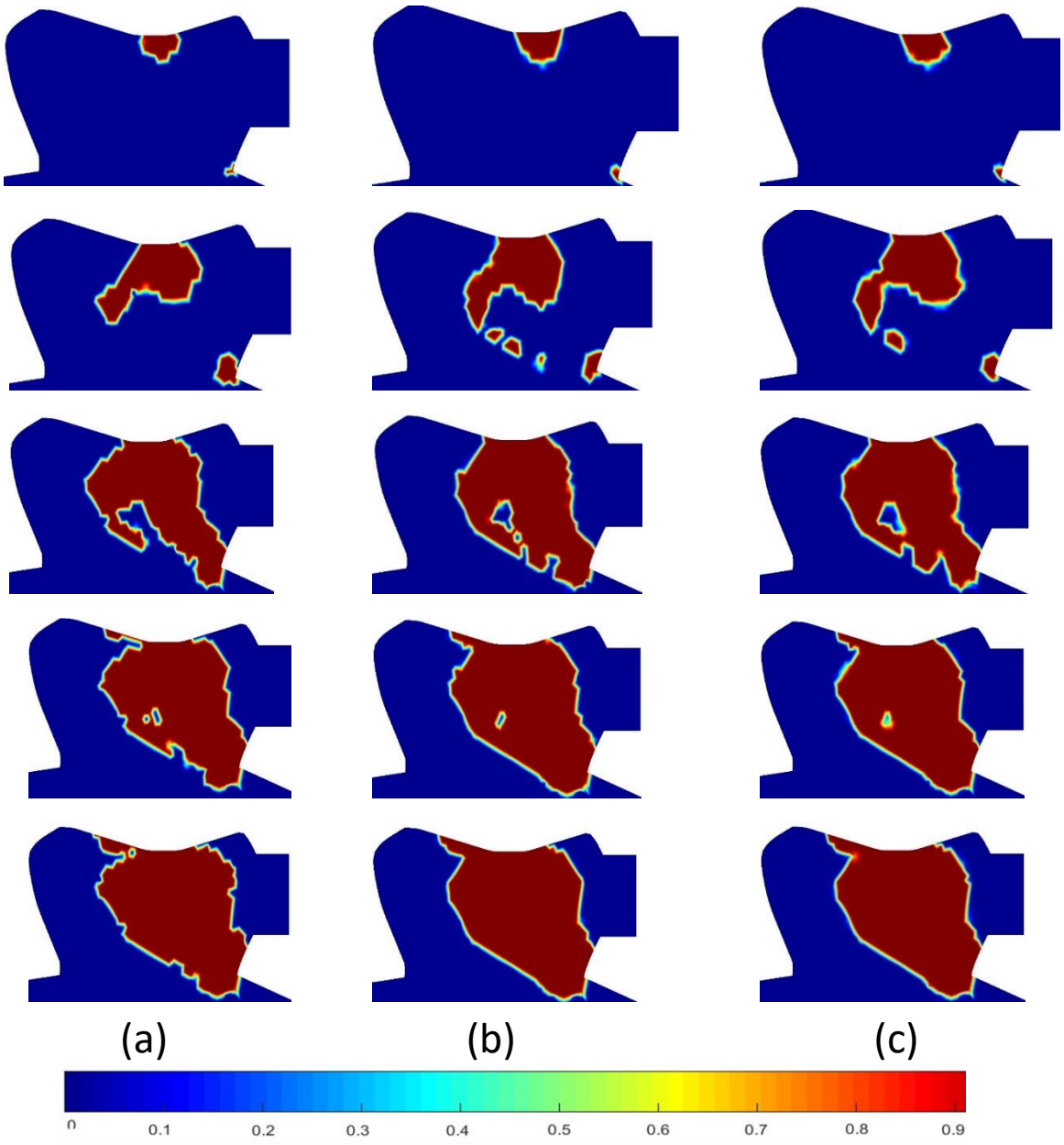

Figure 6. 29. Plastic zone growth on Z250 in the ORV load case. (a) FEM (b) RPIM (c) NNRPIM

For the BLV, BRV, OLV, and ORV load cases, the results are presented in figures 6.30 to 6.45 including the load-displacement, load-plastic strain, effective stress-effective strain, and effective stress-plastic strain graphs.

For BLV load case, force-displacement graph is not enough to see the entrance of the material into plastic zone in points C3 and P1. Therefore, the effective stress-plastic strain and load-plastic strain graphs can help and they show plastic behavior for all four interest points. The displacement is almost

4mm for the nodes in BLV load case except the point P2 which is maximum 1.5 mm based on FEM result. RPIM and NNRPIM show lower displacement for the same point. In overall, the results obtained by meshless methods and finite element method are close.

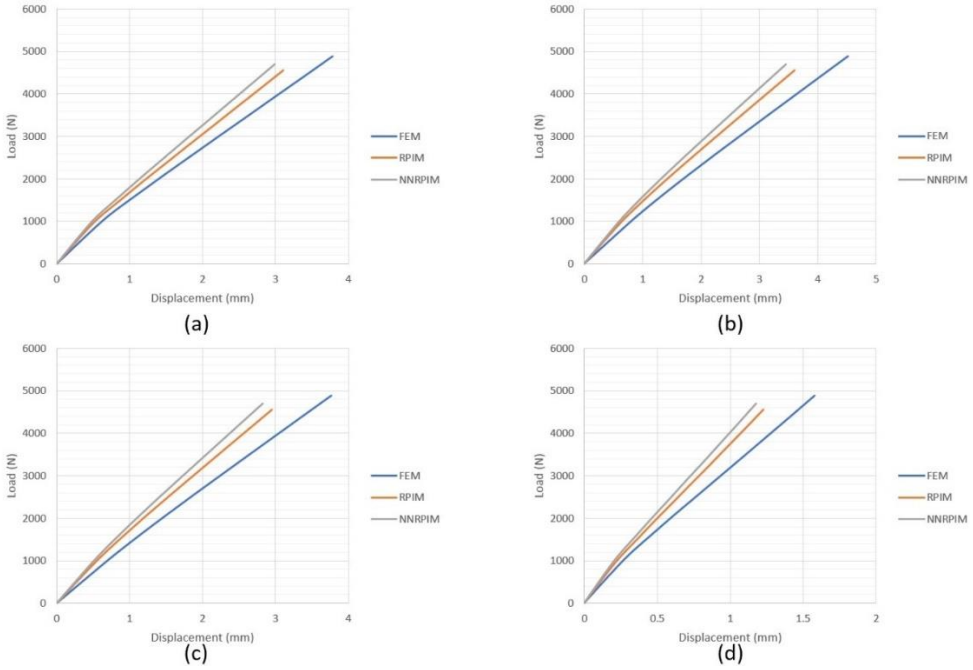

Figure 6. 30. Force-displacement graph for the BLV load case. (a) C7 (b) C3 (c) P1 (d) P2

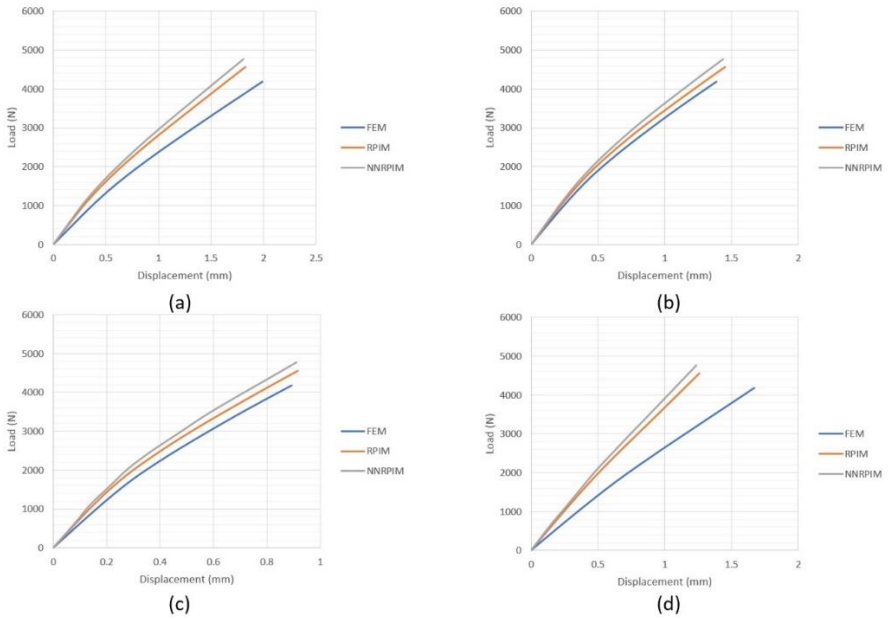

Figure 6. 31. Force-displacement graph for the BRV load case. (a) C7 (b) C3 (c) P1 (d) P2

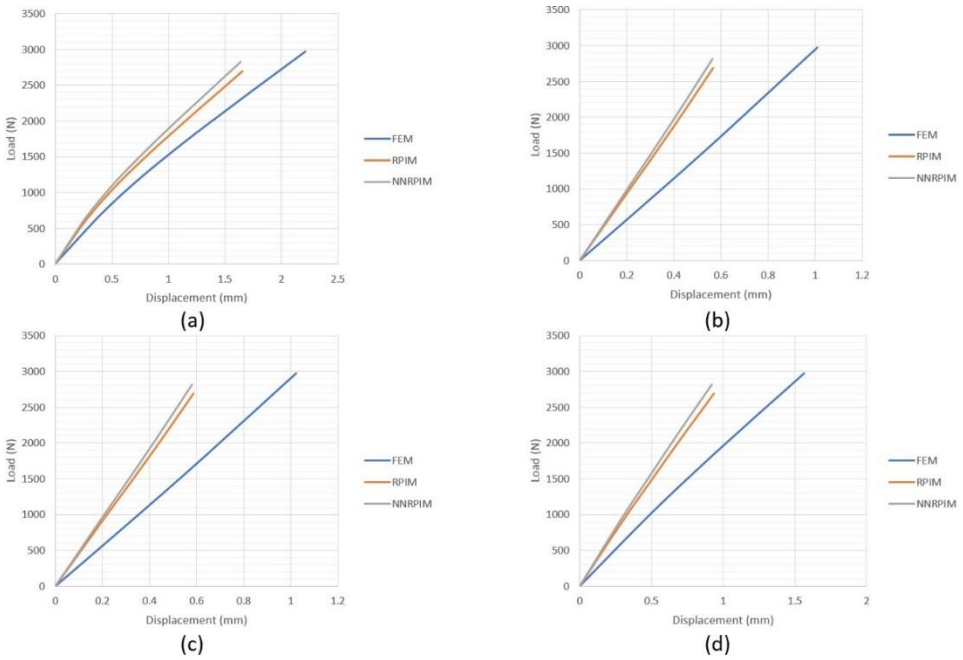

Figure 6. 32. Force-displacement graph for the OLV load case. (a) C7 (b) C3 (c) P1 (d) P2

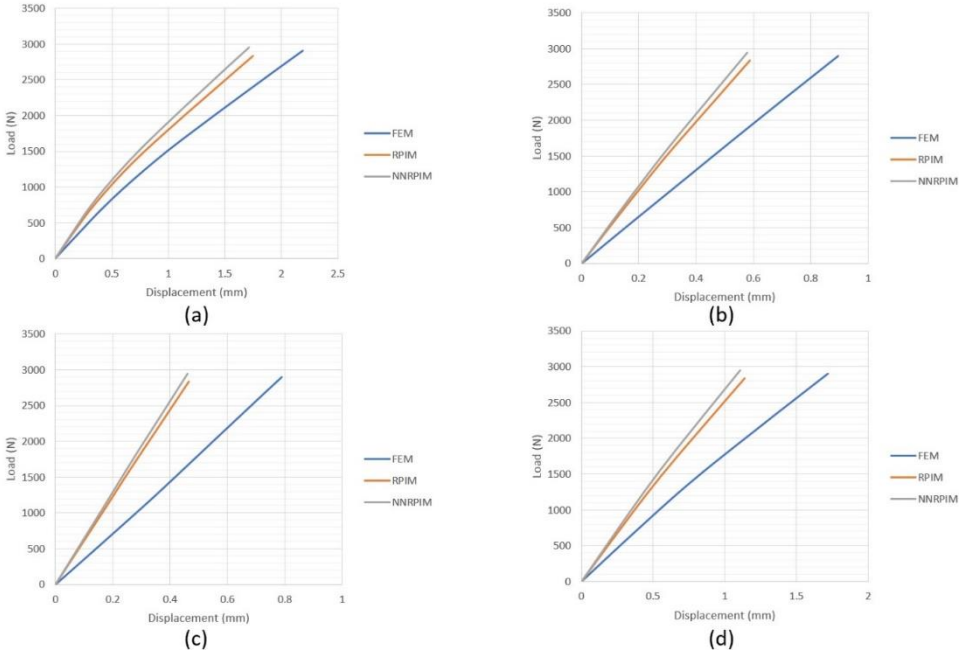

Figure 6. 33. Force-displacement graph for the ORV load case. (a) C7 (b) C3 (c) P1 (d) P2

For the BRV load case, the points C7, C3, and P1 experience transition from elastic regime to plastic regime and the results for all three methods are very close. However, point P2 does not show a very

evident plastic behavior in load-displacement graph. Nevertheless, using the graphs including plastic strain, it can easily show the plastic behavior for all nodes in this loading situation.

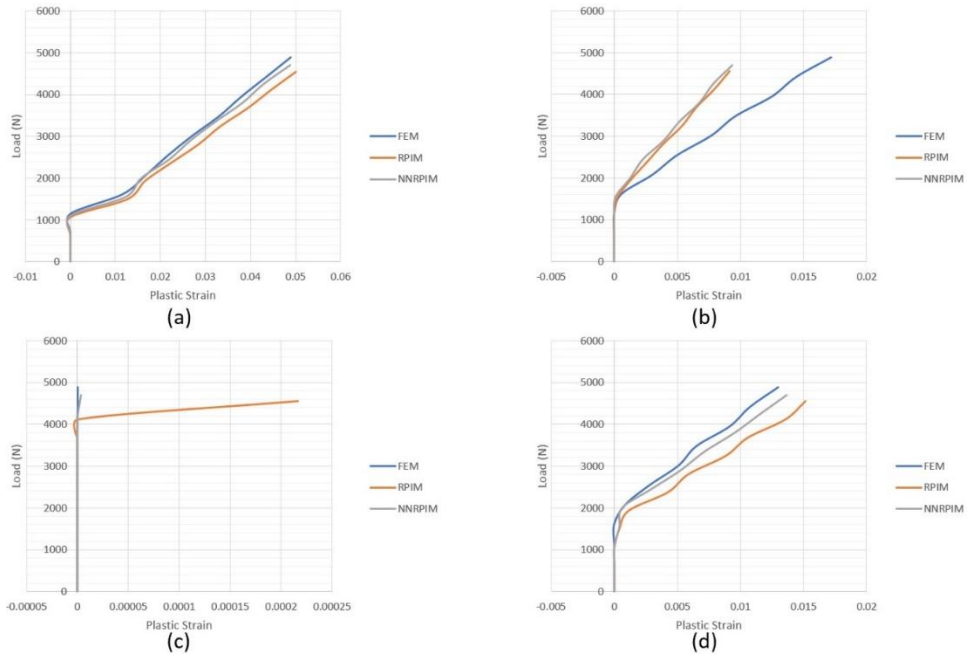

Figure 6. 34. Force-plastic strain graph for the BLV load case. (a) C7 (b) C3 (c) P1 (d) P2

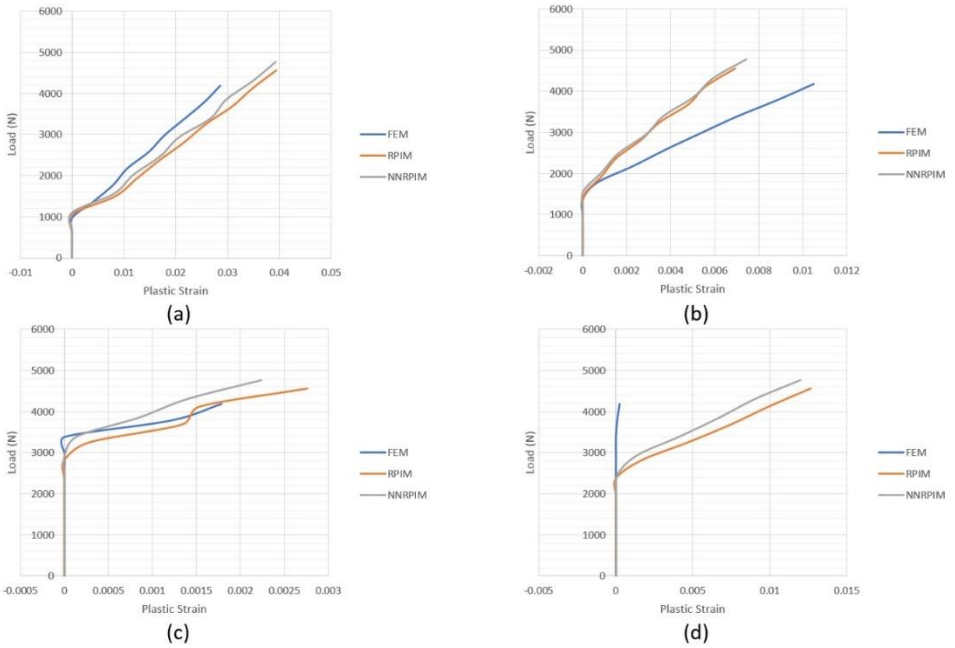

Figure 6. 35. Force-plastic strain graph for the BRV load case. (a) C7 (b) C3 (c) P1 (d) P2

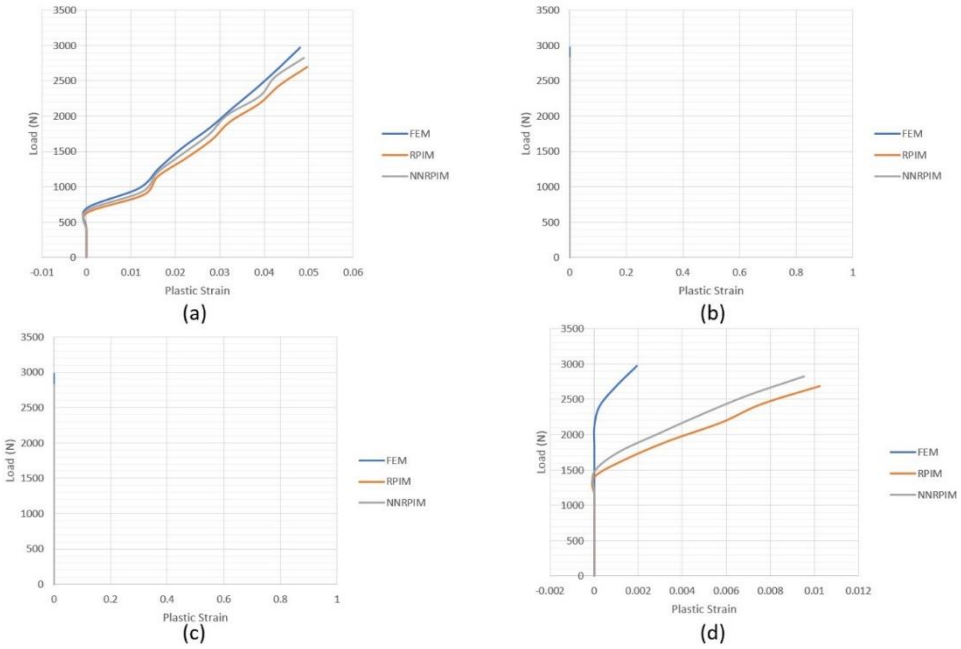

Figure 6. 36. Force-plastic strain graph for the OLV load case. (a) C7 (b) C3 (c) P1 (d) P2

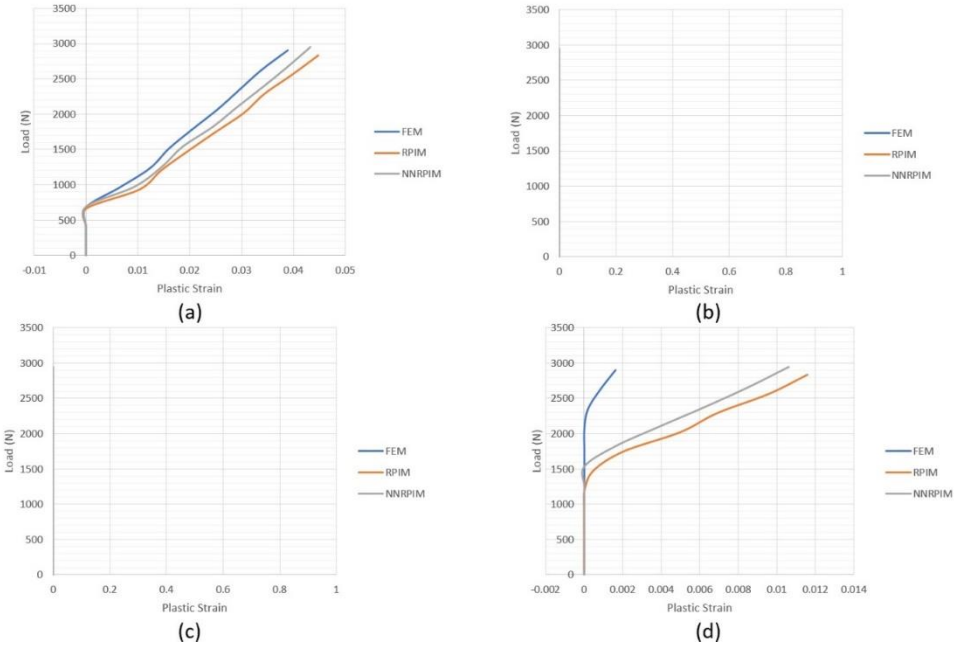

Figure 6. 37. Force-plastic strain graph for the ORV load case. (a) C7 (b) C3 (c) P1 (d) P2

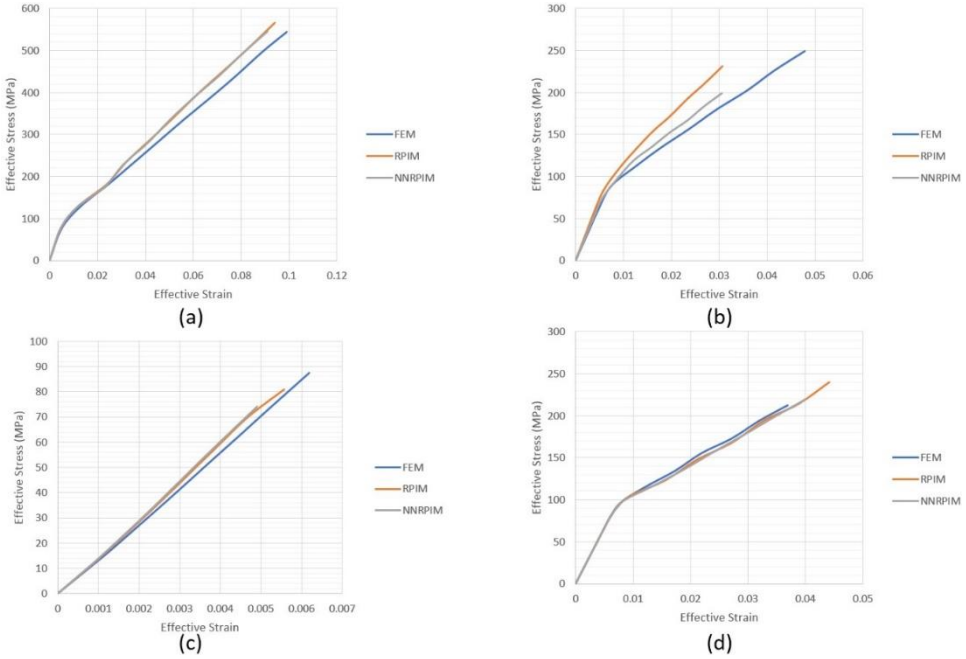

Figure 6. 38. Effective stress-effective strain graph for the BLV load case. (a) C7 (b) C3 (c) P1 (d) P2

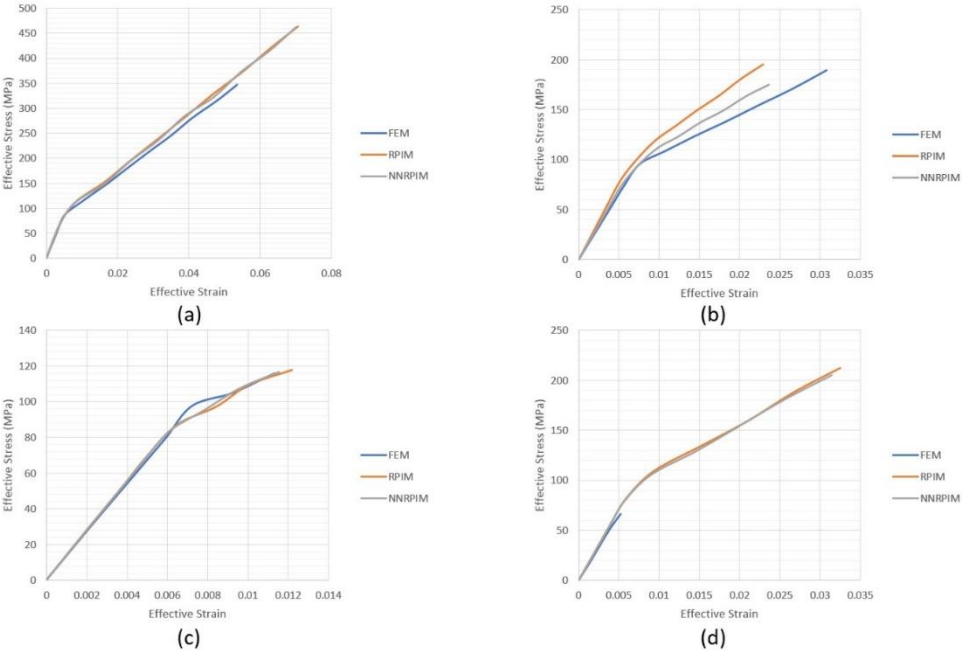

Figure 6. 39.Effective stress-effective strain graph for the BRV load case. (a) C7 (b) C3 (c) P1 (d) P2

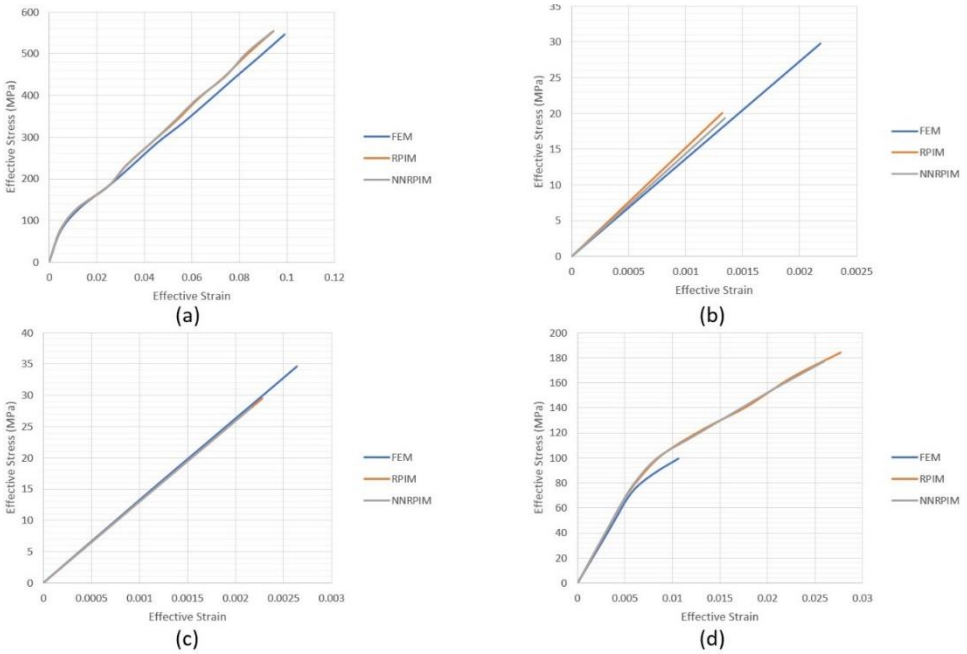

Figure 6. 40.Effective stress-effective strain graph for the OLV load case. (a) C7 (b) C3 (c) P1 (d) P2

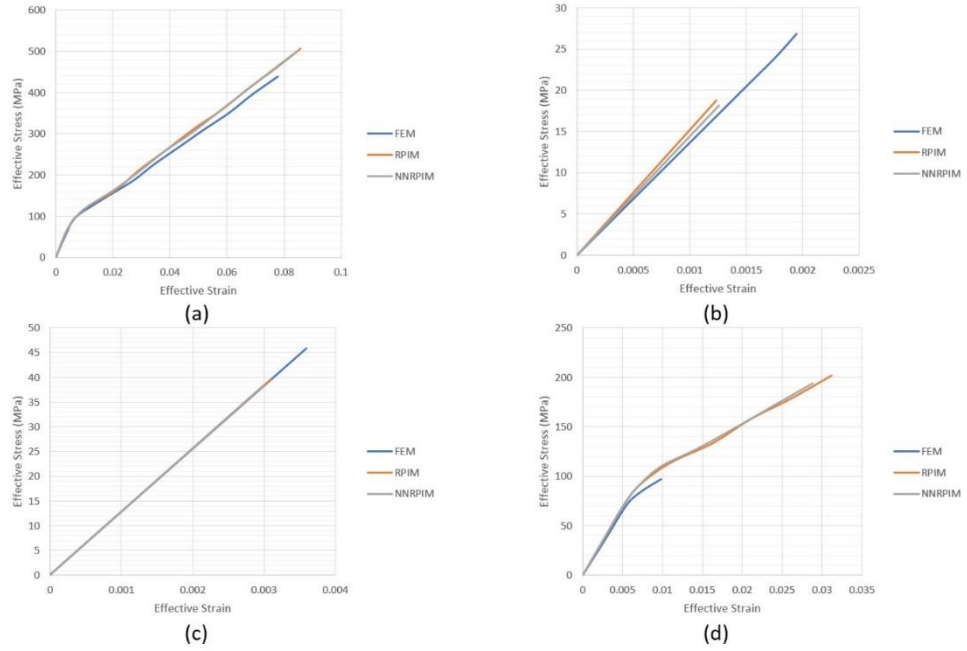

Figure 6. 41.Effective stress-effective strain graph for the ORV load case. (a) C7 (b) C3 (c) P1 (d) P2

For the OLV load case, as presented in load-displacement graph, the results calculated by finite element method are different from meshless methods. But RPIM and NNRPIM still keep their agreement and they have not any considerable deviation from each other. Plastic behavior is visible for this loading situation.

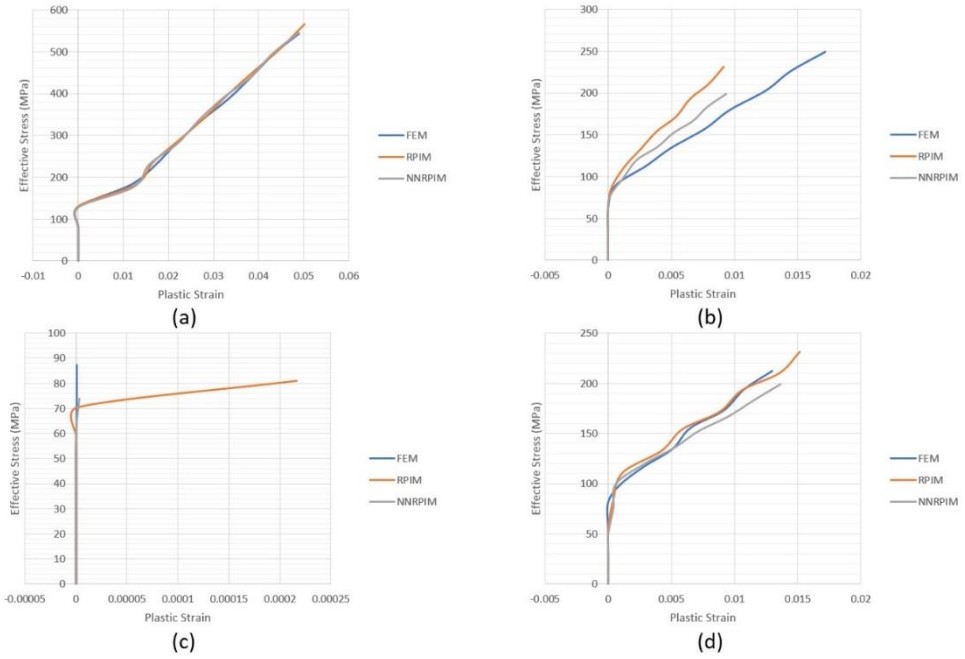

Figure 6. 42. Effective stress-plastic strain graph for the BLV load case. (a) C7 (b) C3 (c) P1 (d) P2

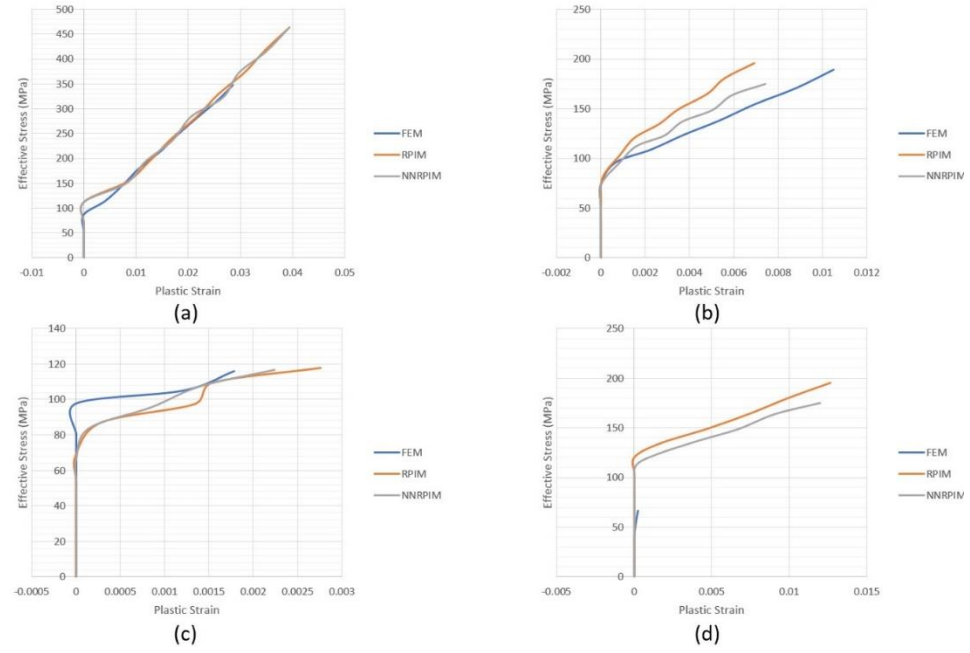

Figure 6. 43.Effective stress-plastic strain graph for the BRV load case. (a) C7 (b) C3 (c) P1 (d) P2

For the ORV load case, the only point in force-displacement graph showing an obvious plastic behavior is C7. Other ones make doubt. Therefore, referring to the graphs related to plastic strain reveal that

there is no plastic behavior for the points C3 and P1 and the maximum displacement belongs to C7 being almost 2mm based on FEM results.

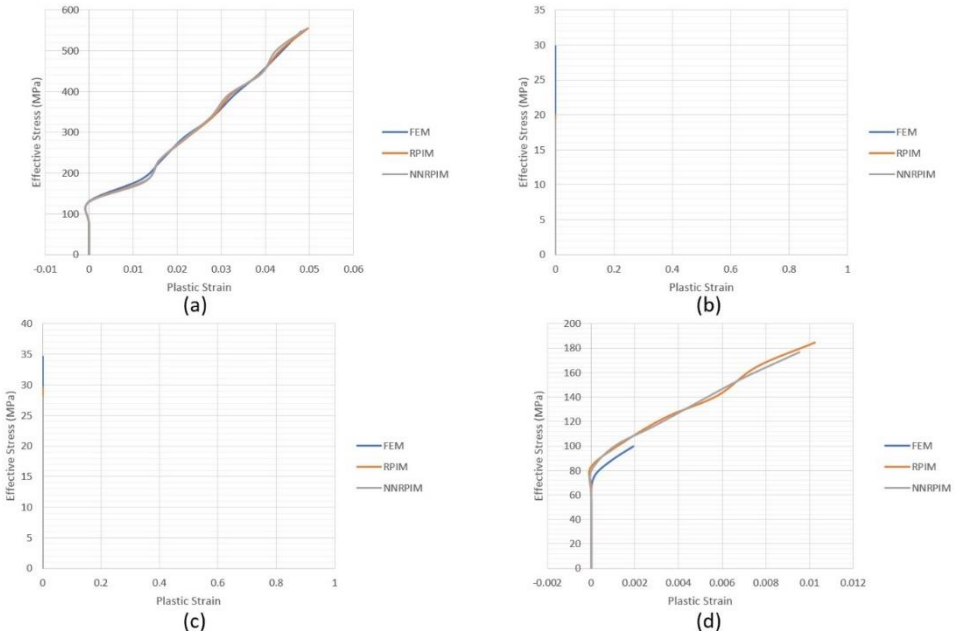

Figure 6. 44.Effective stress-plastic strain graph for the OLV load case. (a) C7 (b) C3 (c) P1 (d) P2

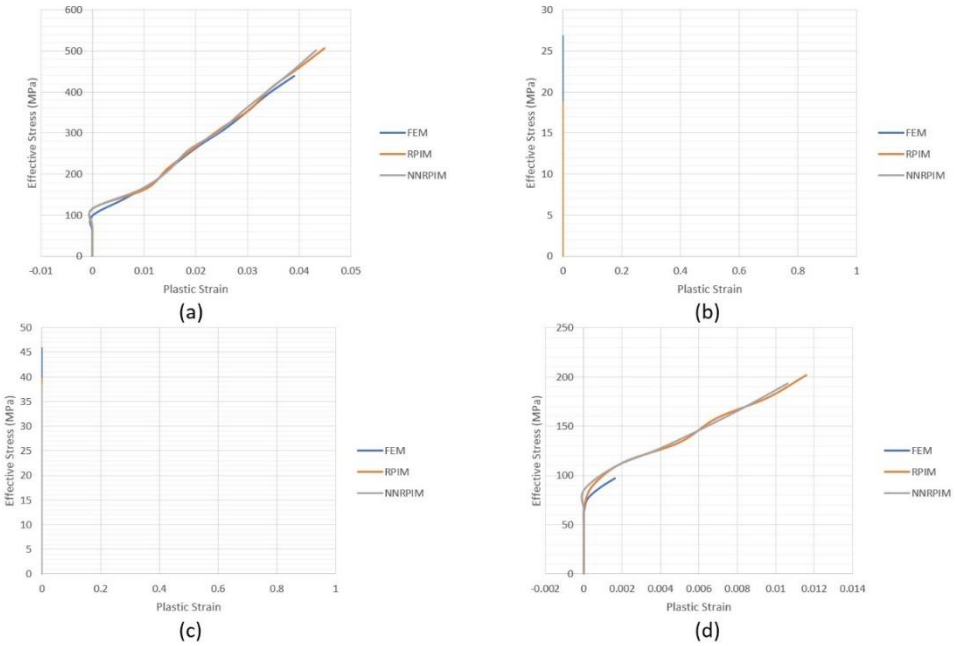

Figure 6. 45. Effective stress-plastic strain graph for the ORV load case. (a) C7 (b) C3 (c) P1 (d) P2

Conclusion

The current work aimed to investigate structural response of dental restorations using advanced numerical discretization meshless methods and finite element method.

Several materials and load cases were analysed, and although the FEM and meshless results were different for distinct points in the 2D domain, in overall Herculite XRV Ultra showed a better elastic and elasto-plastic behavior in comparison to other commercial dental restorative composites.

In the elasto-static analysis, was observed that composites are tolerating the forces better than a normal tooth in the restored area. Furthermore, it is important to demonstrate that in the depicted isomaps of BLV load case, where there is no tooth on the left side of the model (no essential boundary condition), the stress distribution shows higher value on critical regions, mostly close to boundaries. Absence of essential boundary conditions on the left side of the 2D model in BLV and OLV load case, leads the applied force to produce higher level of stress on the borders and critical spots. Nevertheless, based on the results obtained by three computational methods, there is an excellent agreement between RPIM and NNRPIM. However, in some cases, in the points close to more complex curves, finite element method gives a far value from the ones calculated by RPIM and NNRPIM.

In the elasto-plastic analysis, several graphs were shown to understand the nonlinear behaviour of the materials. According to the calculated results and the growth of the plastic regime in 10 increments, it was demonstrated with this work that the restorative dental composites under investigation show a evident plastic behaviour. Four different points are distributed in the 2D domain, close to the borders. Among these nodes, C7 and P2 always show plastic behaviour in all four load cases. It must be remarked, that in the elasto-plastic analysis, the plastic strain remains for zero value for some distinct nodes (C3 and P1) on the 2D domain, especially in the OLV and ORV load cases for both materials Filtek Z250™ and N-Ceram Bulk™ due to the low magnitude of force. Additionally, the stress does not reach the maximum strength of the material.

Considering the interface resistance zone between cortical bone and tooth (either normal or restored), is a research topic that was not included in this work and perhaps could be interesting for future works regarding contact and fracture at the bone or tooth boundary layer. Nevertheless, using a three-dimensional model assuming the boundary conditions would be an interesting topic also for the future works. Considering many numerical parameters that affect the efficiency, the computational cost, and the accuracy of the calculations, contribution of different discretization methods and involving new techniques would lead to obtain better results, capable to create reliable calculations with less errors and more efficiency.

Within the restrictions of the numerical methods, the computational simulations implemented in this work have the capacity to improve and to refine the results until they get closer to clinical observations. Performing these simulations with denser meshes could potentially lead to better results. Furthermore, future composite materials for dental restorations perhaps will possess better mechanical properties, especially a higher Young's Modulus. Thus, with a bit improvement, composites will eventually withstand under occlusal loads of bruxism.

By taking all above-mentioned arguments into consideration, it is notorious that deeper research on this topic would allow to increase the quality of life of patients.

References

[1] A. Czarnetzki and S. Ehrhardt, “Re-dating the Chinese amalgam-filling of teeth in Europe,” *Int. J. Anthropol.*, vol. 5, no. 4, pp. 325–332, 1990.

[2] World Health Organization, “Future Use of Materials for Dental Restoration,” p. 65, 2009.

[3] CDC, “Preventing Cavities, Gum Disease, Tooth Loss, and Oral Cancers,” 2011.

[4] J M ten Cate and T. Imfeld, “Dental erosion,” *Int.Dent.J.*, vol. 48, no. 6, pp. 529–539, 1996.

[5] WebMD, “Tooth Decay,” no. May, pp. 1–2, 2011.

[6] A. Bascones-Martínez, M. Muñoz-Corcuera, S. Noronha, P. Mota, C. Bascones-Ilundain, and J. Campo-Trapero, “Host defence mechanisms against bacterial aggression in periodontal disease: Basic mechanisms,” *Med. Oral Patol. Oral Cir. Bucal*, vol. 14, no. 12, pp. 10–15, 2009.

[7] G. C. Armitage, “Development of a Classification System for Atopic Dermatitis (AD),” *J. Allergy Clin. Immunol.*, vol. 4, no. 1, p. S237, 1999.

[8] J. M. Albandar, “Epidemiology and risk factors of periodontal diseases,” *Dent. Clin. North Am.*, vol. 49, no. 3 SPEC. ISS., pp. 517–532, 2005.

[9] G. C. Armitage and M. P. Cullinan, “Comparison of the clinical features of chronic and aggressive periodontitis,” *Periodontol. 2000*, vol. 53, no. 1, pp. 12–27, 2010.

[10] G. Gustafson and D. Odont Malmo, “Age Determinations on Teeth,” *J. Am. Dent. Assoc.*, vol. 41, no. 1, pp. 45–54, 1950.

[11] J. H. Lee *et al.*, “Morphological analysis of the lower second premolar for age estimation of Korean adults,” *Forensic Sci. Int.*, vol. 281, p. 186.e1-186.e6, 2017.

[12] K. K. Koh, J. S. Tan, P. Nambiar, N. Ibrahim, S. Mutalik, and M. Khan Asif, “Age estimation from structural changes of teeth and buccal alveolar bone level,” *J. Forensic Leg. Med.*, vol. 48, pp. 15–21, 2017.

[13] S. I. Kvaal, K. M. Kolltveit, I. O. Thomsen, and T. Solheim, “Age estimation of adults from dental radiographs,” *Forensic Sci. Int.*, vol. 74, no. 3, pp. 175–185, 1995.

[14] a Sayegh, E. L. Dini, R. D. Holt, and R. Bedi, “Food and drink consumption, sociodemographic factors and dental caries in 4-5-year-old children in Amman, Jordan,” *Br. Dent. J.*, vol. 193, pp. 37–42, 2002.

[15] A. K. Johansson, A. Johansson, D. Birkhed, R. Omar, S. Baghdadi, and G. E. Carlsson, “Dental erosion, soft-drink intake, and oral health in young Saudi men, and the development of a system for assessing erosive anterior tooth wear,” *Acta Odontol. Scand.*, vol. 54, no. 6, pp. 369–378, 1996.

[16] W. H. Bowen, “Comparison of the Cariogenicity of Cola, Honey, Cow Milk, Human Milk, and Sucrose,” *Pediatrics*, vol. 116, no. 4, pp. 921–926, 2005.

[17] R. Cheng, H. Yang, M. Shao, T. Hu, and X. Zhou, “Dental erosion and severe tooth decay related to soft drinks: a case report and literature review,” *J. Zhejiang Univ. Sci. B*, vol. 10, no. 5, pp. 395–399, 2009.

[18] I. Al-Majed, A. Maguire, and J. J. Murray, “Risk factors for dental erosion in 5-6 year old and 12-14 year old boys in Saudi Arabia,” *Community Dent. Oral Epidemiol.*, vol. 30, no. 1, pp. 38–46, 2002.

[19] M. Edwards, S. L. Creanor, R. H. Foye, and W. H. Gilmour, “Buffering capacities of soft drinks: the potential influence on dental erosion,” *J. Oral Rehabil.*, vol. 26, no. 12, pp. 923–927, 1999.

[20] S. Wongkhantee, V. Patanapiradej, C. Maneenut, and D. Tantbirojn, “Effect of acidic food and drinks on surface hardness of enamel, dentine, and tooth-coloured filling materials,” *J. Dent.*, vol. 34, no. 3, pp. 214–220, 2006.

[21] F. Lippert, D. M. Parker, and K. D. Jandt, “Susceptibility of deciduous and permanent enamel to dietary acid-induced erosion studied with atomic force microscopy nanoindentation,” *Eur. J. Oral Sci.*, vol. 112, no. 1, pp. 61–66, 2004.

[22] T. Jensdottir, A. Bardow, and P. Holbrook, “Properties and modification of soft drinks in relation to their erosive potential in vitro,” *J. Dent.*, vol. 33, no. 7, pp. 569–575, 2005.

[23] A. K. Johansson, P. Lingström, T. Imfeld, and D. Birkhed, “Influence of drinking method on tooth-surface pH in relation to dental erosion,” *Eur. J. Oral Sci.*, vol. 112, no. 6, pp. 484–489, 2004.

[24] P. E. Petersen, “The World Oral Health Report 2003 WHO Global Oral Health Programme,” *Community Dent. Oral Epidemiol.*, vol. 31 Suppl 1, pp. 3–23, 2003.

[25] World Health Organization, *World Health Statistics 2017 : Monitoring Health for The SDGs*. 2017.

[26] W. Li, J. Liu, S. Chen, Y. Wang, and Z. Zhang, “Prevalence of dental erosion among people with gastroesophageal reflux disease in China,” *J. Prosthet. Dent.*, vol. 117, no. 1, pp. 48–54, 2017.

[27] A. Vanka, N. M. Roshan, K. S. Ravi, and N. D. Shashikiran, “A review of tobacco cessation

services for youth in the dental clinic," *J. Indian Soc. Pedod. Prev. Dent.*, vol. 27, no. 2, p. 78–84, 2009.

[28] C. C. Alandia-Roman, D. R. Cruvinel, A. B. S. Sousa, F. C. P. Pires-De-Souza, and H. Panzeri, "Effect of cigarette smoke on color stability and surface roughness of dental composites," *J. Dent.*, vol. 41, no. SUPPL. 3, pp. e73–e79, 2013.

[29] B. Gupta, F. Bray, N. Kumar, and N. W. Johnson, "Associations between oral hygiene habits, diet, tobacco and alcohol and risk of oral cancer: A case–control study from India," *Cancer Epidemiol.*, vol. 51, no. March, pp. 7–14, 2017.

[30] A. Basavaraju and K. Slade, "Dental damage in anaesthesia," *Anaesth. Intensive Care Med.*, vol. 18, no. 9, pp. 438–441, 2017.

[31] S. Y. Ham, J. Kim, Y. J. Oh, B. Lee, Y. S. Shin, and S. Na, "Risk factors for peri-anaesthetic dental injury," *Anaesthesia*, vol. 71, no. 9, pp. 1070–1076, 2016.

[32] F. A. Fontijn-Tekamp *et al.*, "Biting and chewing in overdentures, full dentures, and natural dentitions," *J. Dent. Res.*, vol. 79, no. 7, pp. 1519–1524, 2000.

[33] N. Givol, Y. Gershtansky, T. Halamish-Shani, S. Taicher, A. Perel, and E. Segal, "Perianesthetic dental injuries: Analysis of incident reports," *J. Clin. Anesth.*, vol. 16, no. 3, pp. 173–176, 2004.

[34] P. H. Rompré, D. Daigle-Landry, F. Guitara, J. Y. Montplaisir, and G. J. Lavigne, "Identification of a sleep bruxism subgroup with a higher risk of pain," *J. Dent. Res.*, vol. 86, no. 9, pp. 837–842, 2007.

[35] J. M. Serra-Negra, F. Lobbezoo, C. C. Martins, E. Stellini, and D. Manfredini, "Prevalence of sleep bruxism and awake bruxism in different chronotype profiles: Hypothesis of an association," *Med. Hypotheses*, vol. 101, pp. 55–58, 2017.

[36] P. Mojon, J. Thomson, and A. Walls, "The impact of falling rates of edentulism," *Int. J. Prosthodont*, vol. 17, no. 4, pp. 434–440, 2004.

[37] V. Baelum, W. Van Palenstein Helderman, A. Hugoson, R. Yee, and O. Fejerskov, "A global perspective on changes in the burden of caries and periodontitis: Implications for dentistry," *J. Oral Rehabil.*, vol. 34, no. 12, pp. 872–906, 2007.

[38] W. Marcenes *et al.*, "Global burden of oral conditions in 1990-2010: A systematic analysis," *J. Dent. Res.*, vol. 92, no. 7, pp. 592–597, 2013.

[39] H. Tan, K. G. Peres, and M. A. Peres, "Retention of teeth and oral health-related quality of life," *J. Dent. Res.*, vol. 95, no. 12, pp. 1350–1357, 2016.

[40] Y. Heianza, D. Sun, E. B. Rimm, J. E. Manson, K. J. Joshipura, and L. Qi, “Abstract P219: Changes in Dental Health and Coronary Heart Disease Risk: Two Prospective Cohort Studies in Men and Women,” *Circulation*, vol. 137, no. Suppl 1, p. AP219 LP-AP219, Mar. 2018.

[41] “Globocon 2012: Estimated Incidence and Mortality and Prevalence Worldwide in 2012 Population Fact Sheet Portugal,” *International Agency for Research on Cancer*, 2012. [Online]. Available: http://globocan.iarc.fr/Pages/fact_sheets_population.aspx?country=364.

[42] N. J. Kassebaum, E. Bernabé, M. Dahiya, B. Bhandari, C. J. L. Murray, and W. Marcenes, “Global burden of untreated caries: A systematic review and metaregression,” *J. Dent. Res.*, vol. 94, no. 5, pp. 650–658, 2015.

[43] B. a Dye *et al.*, “Trends in oral health status: United States, 1988-1994 and 1999-2004.,” *Vital Health Stat. 11.*, no. 248, pp. 1–92, 2007.

[44] R. R. Seghi, I. L. Denry, and S. F. Rosenstiel, “Relative fracture toughness and hardness of new dental ceramics,” *J. Prosthet. Dent.*, vol. 74, no. 2, pp. 145–150, 1995.

[45] G. Sundh, A., Molin, M. and Sjögren, “Fracture Resistance of Yttrium Oxide Partially-Stabilized Zirconia All- Ceramic Bridges after Veneering and Mechanical Fatigue Testing.,” *Dent. Mater.*, vol. 21, no. 5, pp. 476–82, 2005.

[46] T. W. Clarkson and L. Magos, “The Toxicology of Mercury and Its Chemical Compounds,” *Crit. Rev. Toxicol.*, vol. 36, no. 8, pp. 609–662, 2006.

[47] K. J. Donly, A. Segura, M. Kanellis, and R. L. Erickson, “CLINICAL PERFORMANCE AND CARIES INHIBITION OF RESIN-MODIFIED GLASS IONOMER CEMENT AND AMALGAM RESTORATIONS,” *J. Am. Dent. Assoc.*, vol. 130, no. 10, pp. 1459–1466, 1999.

[48] B. M. Eley, “The future of dental amalgam: a review of the literature. Part 1: Dental amalgam structure and corrosion,” *Br. Dent. J.*, vol. 182, no. 7, pp. 247–249, 1997.

[49] A. Paulauskas, A. Selskis, V. Bukauskas, V. Vaicikauskas, A. Ramanavicius, and Z. Balevicius, “Real time study of amalgam formation and mercury adsorption on thin gold film by total internal reflection ellipsometry,” *Appl. Surf. Sci.*, vol. 427, pp. 298–303, 2018.

[50] M. Bernardo *et al.*, “Survival and reasons for failure of amalgam versus composite posterior restorations placed in a randomized clinical trial,” *J. Am. Dent. Assoc.*, vol. 138, no. 6, pp. 775–783, 2007.

[51] ADA COUNCIL ON SCIENTIFIC AFFAIRS, “DENTAL AMALGAM: UPDATE ON SAFETY CONCERNS,” *JADA*, vol. 129, no. April, 1998.

[52] H. J. Busscher, M. Rinastiti, W. Siswomihardjo, and H. C. Van Der Mei, “Biofilm formation on

dental restorative and implant materials," *J. Dent. Res.*, vol. 89, no. 7, pp. 657–665, 2010.

[53] A. Shenoy, "Is it the end of the road for dental amalgam? A critical review," *J. Conserv. Dent.*, vol. 11, no. 3, pp. 99–107, 2008.

[54] J. Sampson, H. S. Luis, M. Bernardo, and J. Leitão, "Dental Amalgam and Antibiotic- and / or," pp. 475–479, 2008.

[55] N. M. Kilpatrick and A. Neumann, "Durability of amalgam in the restoration of class II cavities in primary molars: a systematic review of the literature," *Eur Arch Paediatr Dent*, vol. 8, no. 1, pp. 5–13, 2007.

[56] K. Abass *et al.*, "Quantitative estimation of mercury intake by toxicokinetic modelling based on total mercury levels in humans," *Environ. Int.*, vol. 114, no. February, pp. 1–11, 2018.

[57] G. M. Richardson, *Assessment of Mercury Exposure and Risks from Dental Amalgam*. Medical Devices Bureau, Environmental Health Directorate, 1995.

[58] A. Fuks and A. Omegan, "Status of amalgams in pediatric dentistry: pros and cons," *Dep. Pediatr. Dent.*, 2005.

[59] B. SEIFERT, K. BECKER, D. HELM, C. KRAUSE, C. SCHULZ, and M. SEIWERT, "The German Environmental Survey 1990/1992 (GerES II): reference concentrations of selected environmental pollutants in blood, urine, hair, house dust, drinking water and indoor air," *J. Expo. Sci. Environ. Epidemiol.*, vol. 10, no. 6, pp. 552–565, 2000.

[60] A. Castaño *et al.*, "Mercury, lead and cadmium levels in the urine of 170 Spanish adults: A pilot human biomonitoring study," *Int. J. Hyg. Environ. Health*, vol. 215, no. 2, pp. 191–195, 2012.

[61] L. Pohl and M. Bergman, "The dentist's exposure to elemental mercury vapor during clinical work with amalgam," *Acta Odontol. Scand.*, vol. 53, no. 1, pp. 44–48, Jan. 1995.

[62] American Dental Association, "Best Management Practices for Amalgam waste ADA," no. October, 2007.

[63] R. L. Bowen, "Properties of a silica-reinforced polymer for dental restorations," *J. Am. Dent. Assoc.*, vol. 66, no. 1, pp. 57–64, 1963.

[64] M. W. Eta, "FUSED PORCELAIN-TO-METAL TEETH," *United States Pat. Off.*, vol. 4, 1962.

[65] R. Jordan and M. Suzuki, "Posterior composite restorations. Where and how they work best.," *J. Am Dent Assoc*, vol. 122, no. 11, pp. 30–37, 1991.

[66] M. Del Nero and J. de la Macorra, "Sealing and dentin bond strengths of adhesive systems," *Oper Dent*, vol. 24, no. 4, pp. 194–202, 1999.

[67] B. A. M. Venhoven, A. J. De Gee, A. Werner, and C. L. Davidson, “Influence of filler parameters on the mechanical coherence of dental restorative resin composites,” *Biomaterials*, vol. 17, no. 7, pp. 735–740, 1996.

[68] J. L. Ferracane and J. C. Mitchem, “Properties of posterior composites: Results of round robin testing for a specification,” *Dent. Mater.*, vol. 10, no. 2, pp. 92–99, 1994.

[69] J. L. Ferracane, “Resin composite—State of the art,” *Dent. Mater.*, vol. 27, no. 1, pp. 29–38, 2011.

[70] R. D. JACKSON and M. MORGAN, “THE NEW POSTERIOR RESINS AND: A SIMPLIFIED PLACEMENT TECHNIQUE,” *J. Am. Dent. Assoc.*, vol. 131, no. 3, pp. 375–383, 2000.

[71] I. L. Dogon, “Present and Future Value of Dental Composite Materials and Sealants,” *Int. J. Technol. Assess. Health Care*, vol. 6, no. 3, pp. 369–377, 1990.

[72] K.-H. Kim, J. L. Ong, and O. Okuno, “The effect of filler loading and morphology on the mechanical properties of contemporary composites,” *J. Prosthet. Dent.*, vol. 87, no. 6, pp. 642–649, 2002.

[73] B. Howard, N. D. Wilson, S. M. Newman, C. S. Pfeifer, and J. W. Stansbury, “Relationships between Conversion, Temperature and Optical Properties during Composite Photopolymerization,” *Acta Biomater.*, vol. 6, no. 6, pp. 2053–2059, Jun. 2010.

[74] R. Chavali, A. H. Nejat, and N. C. Lawson, “Machinability of CAD-CAM materials,” *J. Prosthet. Dent.*, vol. 118, no. 2, pp. 194–199, 2017.

[75] 3M, “Filtek Z250 Technical Profile,” 2018.

[76] 3M, “Filtek Z250 Technical Data sheet,” 2017.

[77] E. 2017. 3M Filtek Supreme Ultra Universal Restorative Technical Product Profile, 3M, “Filtek Technical Product Profile.”

[78] S. M. Chung, A. U. J. Yap, W. K. Koh, K. T. Tsai, and C. T. Lim, “Measurement of Poisson’s ratio of dental composite restorative materials,” *Biomaterials*, vol. 25, no. 13, pp. 2455–2460, 2004.

[79] H. Ultra, “Herculite Ultra Where legacy & advanced technology meet Herculite Ultra.”

[80] D. Abuelenain, Neel, and A. Dharrab, “Surface and Mechanical Properties of Different Dental Composites,” *Austin J Dent. Austin J Dent*, vol. 2, no. 2, pp. 1019–2, 2015.

[81] M. STEWART, “Tetric N-Ceram Bulk Fill Scientific Documentation,” 2014.

[82] H. Forss and E. Widström, “The post-amalgam era: A selection of materials and their longevity

in the primary and young permanent dentitions," *Int. J. Paediatr. Dent.*, vol. 13, no. 3, pp. 158–164, 2003.

[83] K. Sunnegårdh-Grönberg, J. W. V. van Dijken, U. Funegård, A. Lindberg, and M. Nilsson, "Selection of dental materials and longevity of replaced restorations in Public Dental Health clinics in northern Sweden," *J. Dent.*, vol. 37, no. 9, pp. 673–678, 2009.

[84] B. Van Meerbeek, G. Vanherle, M. Braem, and P. Lambrechts, "Trends in the selection of dental filling materials," *J. Dent.*, vol. 19, no. 4, pp. 207–213, 1991.

[85] E. Widström and H. Fross, "Selection of restorative materials in dental treatment of children and adults in public and private dental care in Finland.," *Swed Dent J*, vol. 18, no. 1–2, pp. 1–7, 1994.

[86] H. Forss and E. Widström, "From amalgam to composite: selection of restorative materials and restoration longevity in Finland.," *Acta Odontol. Scand.*, vol. 59, no. 2, pp. 57–62, 2001.

[87] V. Qvist, J. Qvist, and I. A. Mjör, "Placement and longevity of tooth-colored restorations in Denmark," *Acta Odontol. Scand.*, vol. 48, no. 5, pp. 305–311, 1990.

[88] I. A. Mjör, J. E. Dahl, and J. E. Moorhead, "Placement and replacement of restorations in primary teeth," *Acta Odontol. Scand.*, vol. 60, no. 1, pp. 25–28, Jan. 2002.

[89] S. Vidnes-Kopperud, A. B. Tveit, T. Gaarden, L. Sandvik, and I. Espelid, "Factors influencing dentists' choice of amalgam and tooth-colored restorative materials for Class II preparations in younger patients," *Acta Odontol. Scand.*, vol. 67, no. 2, pp. 74–79, Jan. 2009.

[90] I. Espelid, A. B. Tveit, I. Mejàre, H. Sundberg, and A.-L. Hallonsten, "Restorative treatment decisions on occlusal caries in Scandinavia," *Acta Odontol. Scand.*, vol. 59, no. 1, pp. 21–27, Jan. 2001.

[91] A. Baraba, I. Anić, S. Doméjean-Orliaguet, I. Espelid, A. B. Tveit, and I. Miletić, "Survey of Croatian Dentists' Restorative Treatment Decisions on Approximal Caries Lesions," *Croat. Med. J.*, vol. 51, no. 6, pp. 509–514, 2010.

[92] Y. Zhang, Z. Mai, A. Barani, M. Bush, and B. Lawn, "Fracture-resistant monolithic dental crowns," *Dent. Mater.*, vol. 32, no. 3, pp. 442–449, 2016.

[93] D. J. Anderson, "Measurement of Stress in Mastication. I," *J. Dent. Res.*, vol. 35, no. 5, 1956.

[94] A. H. Howell and F. Brudevold, "Vertical Forces Used During Chewing of Food," *J. Dent. Res.*, vol. 29, no. 2, 1950.

[95] E. Homaei, X. Z. Jin, E. H. N. Pow, J. P. Matinlinna, J. K. H. Tsoi, and K. Farhangdoost,

"Numerical fatigue analysis of premolars restored by CAD/CAM ceramic crowns," *Dent. Mater.*, pp. 1–9, 2018.

[96] C. N. Reid, J. Fisher, and P. H. Jacobsen, "Fatigue and wear of dental materials," *J. Dent.*, vol. 18, no. 4, pp. 209–215, 1990.

[97] R. G. Craig, M. K. El-Ebrashi, and F. A. Peyton, "Experimental stress analysis of dental restorations," *J. Prosthet. Dent.*, vol. 17, no. 3, pp. 292–302, 1967.

[98] R. G. Craig, M. K. El-ebrashi, and F. A. Peyton, "Experimental stress analysis of dental restorations Part II. Two dimensional photoelastic stress analysis of crowns," vol. 17, no. 3, pp. 292–302, 1967.

[99] H. Hameed, B. P. Babu, V. M. M. Sagir, K. J. Chiriyath, J. Mathias, and A. P. Shaji, "Microleakage in Resin Composite Restoration following Antimicrobial Pre-treatments with 2% Chlorhexidine and Clearfil Protect Bond.," *J. Int. oral Heal. JIOH*, vol. 7, no. 7, pp. 71–6, 2015.

[100] F. P. Rodrigues, N. Silikas, D. C. Watts, and R. Y. Ballester, "Finite element analysis of bonded model Class i 'restorations' after shrinkage," *Dent. Mater.*, vol. 28, no. 2, pp. 123–132, 2012.

[101] H. Ensa, D. M. O. Doherty, and P. H. Jacobsen, "The influence of the restoration-tooth interface in light cured composite restorations : a finite element analysis," vol. 22, 2001.

[102] B. Cummings, *Macroscopic bone structure*. Pearson Education, 2004.

[103] J. Y. Rho, L. Kuhn-Spearing, and P. Zioupos, "Mechanical properties and the hierarchical structure of bone," *Med. Eng. Phys.*, vol. 20, no. 2, pp. 92–102, 1998.

[104] R. L. Drake, A. Wayne Vogl, and A. W. M. Mitchell, *Gray's Anatomy for students*. Churchill Livingstone, 2009.

[105] J. Y. Rho, R. B. Ashman, and C. H. Turner, "Young's modulus of trabecular and cortical bone material: Ultrasonic and microtensile measurements," *J. Biomech.*, vol. 26, no. 2, pp. 111–119, 1993.

[106] R. B. Martin, "Determinants of the mechanical properties of bones," *J. Biomech.*, vol. 24, pp. 79–88, 1991.

[107] F. Martini, J. Nath, and E. Bartolomew, *Fundamentals of Anatomy & Physiology*, 4th ed. Martini, 1998.

[108] D. Carter and W. Hayes, "The compressive behavior of bone as a two-phase porous structure," *J. Bone Jt. Surg.*, vol. 59, 1977.

[109] L. Gibson, "The mechanical behaviour of cancellous bone," *J. Biomech*, vol. 18, no. 5, pp. 317–

328, 1985.

[110] D. . Enlow, *Principles of Bone Remodeling*. Charles C. Thomas, 1963.

[111] L. Lanyon, "Osteocytes, strain detection, bone modeling and remodeling.," *Calcif Tissue*, vol. 53, pp. 106–107, 1993.

[112] A. Nanci, *Ten Cate's Oral Histology*, 8th ed. Mosby, 2012.

[113] B. Moxham, B. Berkovitz, and G. Holland, *Oral Anatomy, Histology and Embryology*, 4th ed. Mosby, 2009.

[114] B. Moxham, B. Berkovitz, R. Linden, and A. Sloan, *Master Dentistry Volume 3 Oral Biology*, 1st ed. Churchill Livingstone, 2010.

[115] J. C. C. Hu, Y. Chun, T. Al Hazzazzi, and J. P. Simmer, "Enamel Formation and Amelogenesis Imperfecta," *Cells Tissues Organs*, vol. 186, no. 1, pp. 78–85, 2007.

[116] L. Zhang, Z. Wang, J. Chen, W. Zhou, and S. Zhang, "Probabilistic fatigue analysis of all-ceramic crowns based on the finite element method," *J. Biomech.*, vol. 43, no. 12, pp. 2321–2326, 2010.

[117] R. C. Scheid *et al.*, *Dental Anatomy*, 8th ed. 2014.

[118] S. L. Rothman, N. Chaftez, M. L. Rhodes, M. S. Schwarz, and M. S. Schwartz, "CT in the preoperative assessment of the mandible and maxilla for endosseous implant surgery. Work in progress.," *Radiology*, vol. 168, no. 1, pp. 171–175, 1988.

[119] J. J. Abrahams, J. K. Frisoli, and J. Dembner, "Anatomy of the jaw, dentition, and related regions," *Semin. Ultrasound, CT, MRI*, vol. 16, no. 6, pp. 453–467, 1995.

[120] M. Schwarz, S. L. Rothman, M. L. Rhodes, and N. Chaftez, "Computed tomography: Part I. Preoperative assessment of the mandible for endosseous implant surgery," *Int. J. Oral Maxillofac Implant.*, vol. 3, pp. 137–141, 1987.

[121] F. J. Vertucci, "Root canal morphology and its relationship to endodontic procedures," *Endod. Top.*, vol. 10, no. 1, pp. 3–29, 2005.

[122] M. Ash, *Dental Anatomy, Physiology and Occlusion*, 7th ed. Michigan: W.B. SAUNDERS COMPANY, 1993.

[123] G. Townsend, T. Hughes, M. Luciano, M. Bockmann, and A. Brook, "Genetic and environmental influences on human dental variation: A critical evaluation of studies involving twins," *Arch Oral Biol*, vol. 54, pp. 45–51, 2009.

[124] R. Pradeep, N. K. Ahuja, and G. Ankit, "Molar morphology: An evolutionary change or a

developmental variation in north indians," *J. Pierre Fauchard Acad. (India Sect.*, vol. 24, no. 3, pp. 113–115, 2010.

[125] A. Ugural and S. K. Fenster, *Advanced Strength and Applied Elasticity*, 4th ed. Prentice-Hall, 2003.

[126] K. Rajabi and S. Hosseini-Hashemi, "Application of the generalized Hooke's law for viscoelastic materials (GHVMs) in nonlocal free damped vibration analysis of viscoelastic orthotropic nanoplates," *Int. J. Mech. Sci.*, vol. 124–125, no. October 2016, pp. 158–165, 2017.

[127] K. Rajabi and S. Hosseini-Hashemi, "Application of the generalized Hooke's law for viscoelastic materials (GHVMs) in nanoscale mass sensing applications of viscoelastic nanoplates: A theoretical study," *Eur. J. Mech. A/Solids*, vol. 67, pp. 71–83, 2018.

[128] J. Belinha, *Meshless Methods in Biomechanics*. Springer, 2014.

[129] X. Hu, L. Mu, and X. Ye, "Weak Galerkin method for the Biot's consolidation model," *Comput. Math. with Appl.*, vol. 75, no. 6, pp. 2017–2030, 2018.

[130] T. Zhang and T. Lin, "A stable weak Galerkin finite element method for Stokes problem," *J. Comput. Appl. Math.*, vol. 333, pp. 235–246, 2018.

[131] J. Wang and X. Ye, "A Weak Galerkin Finite Element Method for the Stokes Equations," vol. 72204, pp. 1–17, 2013.

[132] J. Dolbow and T. Belytschko, "Numerical integration of the Galerkin weak form in meshfree methods," *Comput. Mech.*, vol. 23, no. 3, pp. 219–230, 1998.

[133] G. R. Liu and S. Quek, "The finite element method: a practical course," p. 433, 2003.

[134] J. Fish and T. Belytschko, *First Course in Finite Elements*. Wiley, 2006.

[135] W. F. Chen and H. Zhang, *Structural Plasticity*, 1st ed. Springer-Verlag New York, 1991.

[136] J. Belinha, "Meshless Methods : The Future of Computational Biomechanical Simulation," *J. Biom. Biostat.*, vol. 7, no. 4, 2016.

[137] Y. Li, G. R. Liu, and J. H. Yue, "A novel node-based smoothed radial point interpolation method for 2D and 3D solid mechanics problems q," vol. 196, pp. 157–172, 2018.

[138] N. -S Lee and K. -J Bathe, "Effects of element distortions on the performance of isoparametric elements," *Int. J. Numer. Methods Eng.*, vol. 36, no. 20, pp. 3553–3576, 1993.

[139] T. Belytschko, P. Krysl, and Y. Krongauz, "A THREE-DIMENSIONAL EXPLICIT ELEMENT-FREE GALERKIN METHOD," vol. 24, no. May 1996, pp. 1253–1270, 1997.

[140] *Mesh Free Methods, Moving beyond the Finite Element Method*. CRC Press. Boca Raton, 2002.

[141] B. V Farahani *et al.*, "A radial point interpolation meshless method extended with an elastic rate-independent continuum damage model for concrete materials rate-independent continuum damage model for concrete materials," vol. 6494, 2016.

[142] J. Belinha, L. M. J. S. Dinis, and R. M. Natal Jorge, "The meshless methods in the bone tissue remodelling analysis," *Procedia Eng.*, vol. 110, pp. 51–58, 2015.

[143] B. V Farahani, P. J. Tavares, P. M. G. P. Moreira, and J. Belinha, "Stress intensity factor calculation through thermoelastic stress analysis , finite element and RPIM meshless method," *Eng. Fract. Mech.*, vol. 183, pp. 66–78, 2017.

[144] J. G. Wang and G. R. Liu, "A point interpolation meshless method based on radial basis functions," vol. 1648, no. November 2001, pp. 1623–1648, 2002.

[145] Y. F. Z. Wing Kam Liu, Sukky Jun, "Reproducing kernel particle methods," *Int. J. Numer. Methods Fluids*, vol. 20, no. 8–9, pp. 1081–1106, 1995.

[146] S. N. Atluri and T. Zhu, "A new Meshless Local Petrov-Galerkin (MLPG) approach in computational mechanics," vol. 22, pp. 117–127, 1998.

[147] B. V. Farahani *et al.*, "The Axisymmetric Analysis of Circular Plates Using the Radial Point Interpolation Method," vol. 2287, pp. 336–353, 2015.

[148] R. Sibson, "A Brief Description of Natural Neighbor Interpolation," *John wiley Sons*, pp. 21–36, 1981.

[149] S. Beissel and T. Belytschko, "Nodal integration of the element-free Galerkin method," *Comput. Methods Appl. Mech. Eng.*, vol. 139, no. 1, pp. 49–74, 1996.

[150] J. S. Chen, S. Yoon, and C. T. Wu, "Non-linear version of stabilized conforming nodal integration for Galerkin mesh-free methods," *Int. J. Numer. Methods Eng.*, vol. 53, no. 12, pp. 2587–2615, 2002.

[151] S. Moreira, J. Belinha, L. M. J. S. Dinis, and R. M. N. Jorge, "Análise de vigas laminadas utilizando o natural neighbour radial point interpolation method," *Rev. Int. Metod. Numer. para Calc. y Disen. en Ing.*, vol. 30, no. 2, pp. 108–120, 2014.

[152] Carlos Felippa, *Introduction To Finite Element Methods (IFEM)*. 1998.

[153] G. R. Liu, G. Y. Zhang, Y. Y. Wang, Z. H. Zhong, G. Y. Li, and X. Han, "A nodal integration technique for meshfree radial point interpolation method (NI-RPIM)," *Int. J. Solids Struct.*, vol. 44, no. 11–12, pp. 3840–3860, 2007.

[154] Wing Kam Liu, Jame Shau-Jen Ong, and R. A. Uras, “Finite element stabilization matrices-a unification approach,” *Comput. Methods Appl. Mech. Eng.*, vol. 53, no. 1, pp. 13–46, 1985.

[155] T. Nagashima, “Node-By-Node Meshless Approach and Its Applications To Structural Analyses,” vol. 385, no. April 1997, pp. 2–3, 1999.

[156] W. K. Liu *et al.*, “Overview and applications of the reproducing Kernel Particle methods,” *Arch. Comput. Methods Eng.*, vol. 3, no. 1, pp. 3–80, 1996.

[157] B. V Farahani, J. Belinha, R. Amaral, P. J. Tavares, and P. M. P. G. Moreira, “Extending radial point interpolating meshless methods to the elasto-plastic analysis of aluminium alloys,” *Eng. Anal. Bound. Elem.*, vol. 000, no. August 2017, p. Available Online, 2018.

[158] L. M. J. S. Dinis, R. M. N. Jorge, and J. Belinha, “Analysis of 3D solids using the natural neighbour radial point interpolation method,” vol. 196, no. 2007, pp. 2009–2028, 2009.

[159] J. M. C. Azevedo, J. Belinha, L. M. J. S. Dinis, and R. M. N. Jorge, “Engineering Analysis with Boundary Elements Crack path prediction using the natural neighbour radial point interpolation method,” *Eng. Anal. Bound. Elem.*, vol. 59, pp. 144–158, 2015.

[160] J. G. Wang and G. R. Liu, “On the optimal shape parameters of radial basis functions used for 2-D meshless methods,” *Comput. Methods Appl. Mech. Eng.*, vol. 191, no. 23–24, pp. 2611–2630, 2002.

[161] J. Belinha, “FEMAS - Finite Element and Meshless Analysis Software.” [Online]. Available: https://jbelinha.webs.com/femas.

[162] J. P. Carey, M. Craig, R. B. Kerstein, and J. Radke, “Determining a relationship between applied occlusal load and articulating paper mark area.,” *Open Dent. J.*, vol. 1, pp. 1–7, 2007.

[163] G. Vasudeva and P. Bogra, “The effect of occlusal restoration and loading on the development of abfraction lesions : A finite element study Background : Aim and Objectives : Materials and Methods : Result : Conclusion :,” vol. 11, no. 3, pp. 117–120, 2008.